Phase-field modeling of freeing water droplets

Yichen Li

Dissertation submitted to the Faculty of the
Virginia Polytechnic Institute and State University
in partial fulfillment of the requirements for the degree of

Doctor of Philosophy
in
Mathematics

Pengtao Yue, Chair
Jeffrey Borggaard
Traian Iliescu
Honghu Liu

December 12, 2025
Blacksburg, Virginia

Keywords: phases-field method, Allen-Cahn equation, heat transfer, phase transition, finite element method

Phase-field modeling of freeing water droplets

Yichen Li

(ABSTRACT)

When a water droplet freezes on a cold plate, a pointy tip forms as the result of volume expansion. In this dissertation, we will introduce a quasi-compressible phase-field model that deals with this non-isothermal three-phase system involving water, ice, and air. The water-ice phase transition and the water-air fluid interface are handled by the Allen-Cahn and the Cahn-Hilliard equations, respectively. The governing equations, including the two phase-field equations, the Navier-Stokes equations, and the energy equation, are designed such that the non-negative entropy production is guaranteed. These equations are then solved by finite-element methods using the open-source deal.ii library. Our model reproduces the Gibbs-Thomson and Clausius-Clapeyron equations, which establish the dependence of the melting temperature on interface curvature and pressure, respectively. Furthermore, the built-in quasi-compressibility accurately accounts for the volume change due to the water-ice density contrast during the phase transition. With proper parameters, our simulation captures the pointy tip of the frozen droplet with good agreement with the experiment.

Phase-field modeling of freeing water droplets

Yichen Li

(GENERAL AUDIENCE ABSTRACT)

Have you ever noticed how a drop of water freezes into a shape with a pointy tip when it lands on a cold surface? It's a fascinating process that involves the transformation of water into ice, and it's more complex than it might seem at first glance. In our study, we explore this phenomenon using a special computer model that simulates the freezing process, including the interactions between water, ice, and air.

Our model uses advanced mathematical equations to understand how water turns into ice and how the tiny boundary between water and air behaves during freezing. These equations help us ensure that our simulation follows the laws of nature, specifically the principles of entropy, which in simple terms, measures the disorder or randomness of a system.

To solve these complex equations, we use a powerful computer program. Our simulations are not just theoretical exercises; they accurately predict the formation of the pointy tip on the frozen droplet, much like what we observe in real-life experiments. This success demonstrates the reliability of our model.

Furthermore, our study delves into the intricate details of how the shape of the frozen droplet is influenced by various factors, including the unique conditions at the point where water, ice, and air meet, and how changes in pressure and temperature affect the freezing process. Our research provides a deeper understanding of the freezing process, which is not only fascinating from a scientific perspective but also has potential applications in various fields, such as climate studies and the development of technologies based on the properties of ice and water.

Contents

List of Figures

List of Tables

Chapter 1

Introduction

1.1 Physical Background and Importance of the Problem

The solidification of a water droplet in the presence of air is a deceptively simple phenomenon. In reality, it is a highly coupled three-phase process involving water, ice, and air, and it plays an important role in both natural environments and engineering applications. In nature, icing influences phenomena such as frost formation, the stability of snowpacks, and the freezing of supercooled raindrops. In engineering, the same physics becomes critical in aircraft icing, wind turbine performance, refrigeration systems, and the design of anti-icing surfaces [56]. A recent comprehensive review by Akhtar et al. [2] further emphasized that droplet freezing spans a wide range of physical scales, from nucleation to macroscopic ice growth, and appears in applications as diverse as food processing, pharmaceutical preservation, thermal energy storage, and atmospheric icing. Despite its apparent simplicity, the freezing of a small droplet already contains many of the core challenges of multiphase solidification.

The water–ice–air system is governed by several intertwined physical mechanisms. One of

the most important is the *density change* associated with the water–ice transition. Because ice is less dense than liquid water, solidification leads to local volume expansion. When a water drop freezes on a cold plate, this expansion pushes the surrounding liquid–gas interface upward and gives rise to characteristic morphological features. Experiments have shown that this expansion is responsible for the formation of the sharp "spicule" or pointy tip that often appears at the end of freezing [20, 40, 49]. Classical studies of premelting and impurity effects also highlight the subtle thermodynamic behavior of ice near its phase boundary [14, 55]. These observations reinforce how sensitive the freezing process is to interfacial physics and thermodynamic driving forces.

Temperature dependence of the melting point also plays a central role in the freezing of a water droplet. The curvature of the interface and the local pressure influence the equilibrium temperature through the Gibbs–Thomson and Clausius–Clapeyron relations, and these effects become especially important near the top of the droplet where curvature can be large. As the freezing front advances, the pressure distribution adjusts in time, and the interface temperature follows these thermodynamic constraints. Classical studies have long shown that curvature can suppress or elevate the melting point, depending on the local geometry of the interface [9, 34]. These ideas have been used extensively to interpret the behavior of ice near its phase boundary, including the formation of premelted films and the sensitivity of ice surface properties to the ambient pressure and curvature [14, 55]. More recent work provides additional insight into how curvature, pressure, and temperature interact during solidification. For instance, high-resolution analyses of interface thermodynamics highlight how the Gibbs–Thomson effect couples with heat transport in materials that exhibit density change during freezing [52]. Reviews of water solidification modeling also emphasize that accurate predictions of interface temperature require a consistent treatment of curvature and pressure, especially in small droplets where geometric effects are amplified [2]. These findings reinforce the idea that droplet icing cannot be described by thermal diffusion alone. Instead, the process requires a thermodynamic framework in which interfacial curvature, pressure

variation, and latent heat release are linked directly to the evolution of the solidification front.

The interface dynamics themselves are complex. High-speed imaging has revealed that internal flow patterns, surface tension gradients, and even small air currents can alter the freezing rate and the shape of the growing ice front [32]. Recent experiments by Karlsson et al. [33] showed that internal recirculating flow persists well into the freezing process, influencing both the advance of the solidification front and the local temperature distribution. These studies suggest that fluid motion cannot be neglected, even when the droplet appears quasi-static from the outside.

Surface properties further complicate the picture. On many substrates, freezing initiates at the contact line, and the subsequent motion of the interface depends strongly on surface wettability. Systematic experiments show that hydrophilic and hydrophobic substrates produce markedly different ice morphologies and freezing times [20, 50]. Beyond intrinsic wettability, surface morphology also influences freezing behavior. For example, Hosseini et al. [28] demonstrated that micro-scale surface features modify the impacting–freezing dynamics of supercooled droplets, changing both nucleation behavior and the eventual ice shape. These findings highlight how interfacial mechanics and substrate characteristics feed directly into the freezing pathway.

When viewed together, these mechanisms reveal why modeling droplet icing is difficult. The water–ice–air system exhibits strong coupling between mass, momentum, and energy transport. The density jump creates velocity divergence during the phase transition. The curvature and pressure dependence of the melting temperature introduce nonlinear feedback between interface geometry and heat transfer. The motion of the free surface is tied to both local solidification rates and global volume conservation. Furthermore, the gas phase cannot be ignored: airflow alters convective heat transport and can change the freezing pathway [56]. Even at laboratory scales, capturing these effects consistently requires a modeling

framework that respects the thermodynamic structure of the system and handles multiple moving interfaces.

For these reasons, droplet icing serves as a challenging but revealing benchmark for studying non-isothermal multiphase solidification. A successful model must incorporate density change, interfacial thermodynamics, and the coupling between flow and phase transition. The present work is motivated by this need: to develop a thermodynamically consistent formulation for a three-phase water–ice–air system in which the dynamics of the interfaces, the non-isothermal environment, and the density variation are treated in a unified framework.

1.2 Existing Understanding of Droplet Freezing (Experimental and Theoretical)

The freezing of a water droplet has been examined for decades through a combination of analytical models and controlled laboratory experiments. Early analyses, such as the classical study of sessile drop solidification by Schultz et al. [43], treated the problem as a Stefan-type phase change process and revealed how the solidification front grows from the substrate toward the droplet apex. These early works established several characteristic features that later became central in icing research, including the formation of a concave freezing front and the sensitivity of the freezing time to heat transfer at the substrate.

A distinctive morphological signature of droplet icing is the sharp "tip" or "spicule" that appears at the end of the freezing process. Experiments by Marín et al. [40] and the analysis of Snoeijer and Brunet [49] demonstrated that this pointed structure results primarily from the density decrease of water upon freezing, which forces the remaining liquid upward as the volume expands. This mechanism is robust across a wide range of cooling conditions. Additional experiments, such as the study of drop freezing on solid surfaces by Chaudhary and Li [11], confirmed the same trend and showed that the upward displacement of the

liquid–air interface is closely tied to the evolving solidification front.

Surface properties also play a critical role. Fuller et al. [20] showed that substrate wettability can noticeably influence the front shape, interface speed, and total freezing time. Their results indicate that hydrophilic surfaces tend to anchor the freezing front at the base, whereas hydrophobic surfaces promote a different propagation pattern and may lead to modified ice morphologies. Similar conclusions were reported by Tavakoli et al. [50], who observed that droplets on hydrophilic surfaces tend to freeze from the bottom upward, while droplets on less-wettable substrates sometimes develop asymmetric fronts or delayed nucleation. Recent studies provide further support for this idea. For example, Kong et al. [37] examined impact-freezing of supercooled droplets and demonstrated that surface wettability changes the nucleation location and alters the freezing dynamics. A more detailed investigation by Shang et al. [44] showed that wettability affects both the internal flow and the shape of the advancing freezing front, especially during early impact stages on cold substrates.

High-speed imaging studies broadened our understanding of the internal dynamics. In particular, Jung et al. [32] documented the internal flow structures inside a supercooled droplet and showed that the water–air interface may deform before freezing fully sets in. Their experiments suggested that small disturbances, such as natural convection inside the drop or external air flow, can modify the solidification pattern. Direct flow measurements by Zeng et al. [64] further demonstrated that gravity influences the shape of the freezing front, the timing of nucleation, and the eventual formation of the tip. These observations highlight the role of the surrounding gas phase and explain why some icing morphologies cannot be reproduced if one neglects air–liquid interactions.

The relevance of airflow has motivated extensive studies in aerospace icing. As summarized by Yamazaki et al. [56], airflow can enhance convective cooling and shift the freezing front toward the upstream direction. Even mild air motion may change the local heat flux around the droplet and lead to asymmetric or accelerated icing. This connection between

environmental factors and icing morphology is important for interpreting experiments and for designing numerical models that aim to capture realistic freezing scenarios.

Altogether, the existing experimental and theoretical literature paints a coherent picture. The freezing front is strongly shaped by density change, curvature effects, and heat transfer; the contact line frequently serves as a nucleation site; and the final tip is a geometric consequence of water expanding as it becomes ice. At the same time, factors such as substrate wettability, surface morphology, gravity, and external airflow introduce additional complexity. Because these influences interact with the solid–liquid and liquid–gas interfaces simultaneously, the droplet icing problem is inherently multiscale and tightly coupled. These insights provide essential guidance for developing a physically consistent model that can capture the key dynamics observed in experiments.

1.3 Numerical Modeling Approaches for Droplet Freezing

The freezing of a water droplet involves the interaction of three phases, two curved and mobile interfaces, and a strongly non-isothermal environment. As a result, many numerical models have been proposed over the past decades, each focusing on different aspects of the problem. The main approaches can be grouped into three broad categories: sharp–interface or front–tracking methods, volume–fraction based methods such as VOF and Level–Set, and diffuse–interface methods based on the phase–field formulation. Each family of methods has contributed important physical insight, but each also comes with limitations that motivate the need for a more unified and thermodynamically consistent framework.

1.3.1 Sharp–Interface and Front–Tracking Approaches

Early numerical work treated the solid–liquid interface as a sharp moving boundary, often formulated through Stefan-type conditions. In these models, the freezing front is reconstructed explicitly, and the latent heat release is enforced through interfacial jump conditions. For instance, Tembely and Dolatabadi [51] developed a lubrication-based sharp–interface formulation to describe the solidification of a sessile droplet. Their model could predict the concave ice front, the freezing time, and the tip formation observed experimentally. Similarly, Zhang et al. [65] used a front-tracking approach to account for the liquid–solid volume change by injecting or removing mass, which allowed them to capture the upward motion of the droplet surface as freezing progressed.

Sharp–interface techniques provide a clear geometric description of the freezing front. However, they require explicit interface reconstruction and special numerical treatment at the contact line. Handling the triple junction is especially delicate when the interface becomes highly curved or when the substrate imposes a nontrivial contact angle. Extending these approaches to three-phase systems becomes cumbersome, since one must track both the liquid–air and solid–liquid interfaces at the same time.

1.3.2 Volume-of-Fluid and Level–Set Approaches

Methods based on volume fractions, such as the Volume-of-Fluid (VOF) and Level–Set methods, have been widely used to capture large deformations of the liquid–air interface. These formulations naturally handle topological changes such as breakup and coalescence. Shetabivash et al. [48] proposed a multiple Level–Set model for containerless freezing, in which one level–set field describes the liquid–gas boundary while another tracks the solid–liquid interface. Their model incorporates density change by modifying the continuity and energy equations and successfully reproduces the pointy tip associated with volume expansion.

More recent work extends these ideas by coupling Level–Set or VOF with additional transport models. For example, a lattice–Boltzmann–phase-field hybrid approach was introduced by Huang et al. [29] to simulate containerless freezing with improved resolution of the moving interface. Although the method targets levitated droplets, it highlights how multiphysics solvers can be combined to follow both curved boundaries and evolving thermal fields.

Despite their versatility, VOF and Level–Set methods face well-known challenges when accurate interfacial physics is required. Surface tension and curvature may be under-resolved without additional smoothing, and imposing consistent contact angles near the wall can be difficult. The physics at the triple junction requires special numerical treatment. These issues become more pronounced when phase change is involved, since thermodynamic relations must be enforced precisely at the solid–liquid boundary.

1.3.3 Phase–Field Approaches

Phase–Field methods describe interfaces as finite–thickness transition layers rather than sharp boundaries. The approach dates back to classical work on dynamic critical phenomena, in which an order parameter evolves according to thermodynamically motivated equations [27]. Later, Cahn and Hilliard introduced an energetic description for binary mixtures, and their ideas were formulated for fluid flows through the reviews of Anderson et al. [3] and the phase-field overview of Emmerich [18]. These studies established the basic framework used today: the interface is identified with rapid but smooth variations of an order parameter, and its motion follows a free–energy functional that incorporates interfacial energy, mixing energy, and capillary forces.

Early applications of diffuse–interface theory to hydrodynamics focused on incompressible two-phase flows. A key step was the work of Gurtin et al. [25], who provided a thermodynamically consistent formulation based on continuum mechanics. Soon after, Chella and Viñals [12] and Jacqmin [31] demonstrated that the phase-field methodology can be used

in direct numerical simulations of interfacial flows, including convection-driven mixing and Navier–Stokes two-phase systems. These contributions confirmed that the combination of the Cahn–Hilliard (CH) and Navier–Stokes equations can naturally capture interface deformation, breakup, and coalescence.

As applications grew, the main challenge became the treatment of fluids with different densities. The classical incompressible formulation enforces $\nabla \cdot \mathbf{v} = 0$, which is incompatible with a mixture whose density depends on an order parameter. The first consistent resolution of this difficulty was given by Lowengrub and Truskinovsky [39], who introduced the quasi–incompressible model. Their theory shows that mass conservation leads to a modified divergence condition

$$\nabla \cdot \mathbf{v} = -\frac{1}{\rho}\frac{D\rho}{Dt},$$

and that the CH equation determines the density variation. This model laid the foundation for later diffuse-interface descriptions of variable-density flows.

Several extensions built upon this idea. Boyer [8] proposed a formulation based on volume fractions and derived a consistent mixture stress. Ding et al. [15] developed a practical numerical model suitable for large density ratios. Shen and Yang [46] introduced a related system that remains incompressible but accounts for density contrast through modified stresses. A more rigorous treatment was given by Abels et al. [1], who derived an incompressible two-phase model that satisfies thermodynamic consistency and uses the volume-averaged velocity. Later studies, such as Guo et al. [24], further clarified the energy law and provided numerical schemes that preserve the dissipation structure. These works established the modern phase-field framework for two-phase systems with variable density, viscosity, and strong interfacial forces.

The development of phase-field methods for flows involving more than two phases followed naturally from the two-phase theory. Dong [16] and Dong [17] constructed N-phase formulations using general order parameters and showed how to maintain consistency among

multiple interfaces. Their models retain the essential free-energy structure and recover correct pairwise surface tensions. More recent studies include the moving-contact-line model of Yu and Yang [61], which incorporates variable densities and viscosities in situations where the interface meets solid boundaries.

Taken together, these contributions form a coherent progression. The diffuse-interface approach originates from free-energy principles, evolves through the modeling of binary fluids, and is extended to variable-density and multiphase systems with a consistent thermodynamic structure. Because the method avoids explicit interface tracking and allows topological changes to occur naturally, it has become a standard tool for complex interfacial flows. This framework motivates the model developed in this work, where phase-field variables describe the water–ice and water–air interfaces, and the governing equations follow directly from the free-energy functional and the thermodynamic relations introduced earlier.

1.4 Recent Advances in Three-Phase (Water–Ice–Air) Modeling

The freezing of water droplets involves the interaction of water, ice, and air. Although the solidification of droplets has been studied for many years, only recent work has tried to describe all three phases in a single framework. Early studies usually modeled each interface with a different numerical strategy. For example, diffuse-interface methods were used for the liquid–gas surface, while the ice front was represented by a sharp interface or a front-tracking method. This split description made it difficult to capture the coupling between the two interfaces, especially when density change during freezing moved the free surface upward or when the geometry changed quickly. In such settings, the motion of one interface affects the other, and a mixed treatment may introduce errors in curvature and mass conservation.

Other approaches used several interface-capturing fields. A typical example is the two-level-

set method developed for three-phase phase change, as in Shetabivash et al. [48]. One level-set function tracked the liquid–gas surface and another tracked the liquid–solid boundary. By modifying the continuity and energy equations, these methods included the density jump and applied suitable interface conditions at the three-phase point. They reproduced some features of the freezing process but still relied on curvature reconstruction and special procedures near the tri-junction. These requirements become more restrictive when convection is important or when the interfaces move rapidly.

Some studies applied phase-field modeling to freezing droplets but only for two phases. For instance, Hagiwara et al. [26] used a phase-field model for the ice growth while the surrounding air was treated through an immersed boundary method. Their simulations helped explain the oscillation and damping of the free surface during impact, and they captured the effect of ice-shell formation on the temperature field. However, the air phase was not part of the diffuse-interface formulation, so the model did not provide a unified description of the water–ice–air system.

Progress toward a more systematic three-phase formulation was made in the context of general multiphase flow modeling. The work of Kim and Lowengrub [36] introduced a thermodynamically consistent ternary Cahn–Hilliard system coupled with Navier–Stokes. Their free-energy functional and dissipation structure provided a clear framework for three-phase interactions, although the model was isothermal and did not include phase change. The study of Boyer et al. [7] extended the Cahn–Hilliard and Navier–Stokes equations to three-phase mixtures with different densities and viscosities. Their focus was on incompressible flows and did not address solidification, but their conditions on the free-energy potential remain important for avoiding spurious phases in ternary systems. These works form the basis for many later studies of three-phase interfaces.

More recent fluid models have also improved the consistency between capillary forces and the momentum equation. For example, Huang et al. [30] developed a balanced-force method for

two-phase flows that reduces spurious velocity and ensures a conservative formulation. Their ideas highlight the numerical difficulty of coupling surface tension and density variation, which becomes even more challenging in three-phase freezing where two moving interfaces interact with each other. The reviews by Chen [13] and Qin and Bhadeshia [41] also emphasized that a consistent free-energy structure is essential for any phase-field model, especially when several phases coexist.

Building on these foundations, Zhang et al. [66] proposed a diffuse-interface description for water–ice–air systems using two order parameters. A Cahn–Hilliard variable represented the water–air interface and an Allen–Cahn variable represented the phase change. Their model allowed the density to vary across the interfaces by relaxing the incompressibility constraint. This choice led to a non-zero velocity divergence and required additional assumptions in the pressure equation. The formulation reproduced several qualitative features of freezing, but it did not include a full energy law and some equations were hard to justify from a strict thermodynamic viewpoint.

A different direction was taken by Wang et al. [54], who developed an energy-stable three-phase formulation in an incompressible setting. Their system combined the Navier–Stokes, Cahn–Hilliard, and Allen–Cahn equations and used a convex-splitting strategy to guarantee unconditional stability of the discrete scheme. Their velocity field satisfies a zero-divergence condition, so density-driven motion is not captured. This model is not an extension of Zhang et al. [66] but provides a stable alternative for simulating ice formation under controlled conditions.

Overall, the development of three-phase water–ice–air modeling has moved from mixed-interface descriptions to diffuse-interface formulations that attempt to represent all phases in a unified way. Existing models differ in how they treat density variation, free-energy structure, and numerical stability. No current formulation resolves all difficulties. These limitations motivate the present work, which aims to construct a thermodynamically consis-

tent three-phase model that captures both the interfacial motion and the flow field during droplet freezing.

1.5 Thesis Outline

Although past studies have provided valuable insight into droplet icing, existing models still cannot fully resolve the coupled physics of a water–ice–air system. Many sharp–interface and front–tracking formulations struggle near the moving contact line, and volume–tracking approaches often have difficulty enforcing curvature, contact angle, and mass conservation in a consistent way. Recent phase–field models have made important progress, yet several essential features remain only partially treated: the thermodynamic link between curvature and melting temperature, the strong density contrast between water and ice, and the quasi-incompressible nature of the mixture during phase change. These limitations motivate the development of a more unified framework.

The model proposed in this study aims to address these gaps. The formulation is rooted in the fundamental principles of thermodynamics and derives all constitutive relations through non-negative entropy production. By combining the Allen–Cahn and Cahn–Hilliard equations with the quasi-incompressible Navier–Stokes system, the model captures both the water–ice phase transition and the deformable water–air interface within a single framework. The resulting system can represent density variation, curvature-induced melting-point shifts, and the non-isothermal coupling among the three phases.

The main contributions of this thesis are summarized as follows:

- A thermodynamically consistent phase-field formulation for a three-phase (water–ice–air) system that incorporates the Gibbs–Thomson and Clausius–Clapeyron relations directly into the free-energy structure.

- A quasi-incompressible mixture framework that accounts for density variation during solidification while maintaining mass conservation through the modified continuity equation derived in Appendix C of Yue [62].
- A coupled Cahn–Hilliard–Allen–Cahn model capable of representing two interfaces simultaneously, together with a single mixture velocity field governed by the Navier–Stokes equations.
- A numerical scheme that handles large density ratios and strong interfacial forces, enabling stable simulations of long-time icing processes and complex interface morphologies.
- A set of computational studies that validate the model against known physical behaviors, including volume expansion, upward motion of the free surface, and characteristic ice-front evolution.

The structure of the thesis is as follows. Chapter 2 introduces the thermodynamic framework and derives the free-energy functional, entropy production, and constitutive relations that form the foundation of the three-phase model. Chapter 3 presents the governing equations, including the quasi-incompressible mass balance, the momentum equations, and the coupled Allen–Cahn and Cahn–Hilliard formulations for the two order parameters describing the three-phase system.

Chapter 4 examines a simplified three-phase model designed to isolate the intrinsic phase-field dynamics. By removing convection, thermal effects, and density variation, this reduced system keeps the essential Cahn–Hilliard and Allen–Cahn structures while providing a cleaner setting for analyzing energy dissipation and for developing stable SAV/IEQ time-stepping schemes. The simplified model therefore serves as a venue for the exploration of efficient energy-stable numerical schemes.

Chapter 5 discusses the numerical discretization and outlines the solution algorithm for

the fully coupled system. Chapter 6 provides numerical experiments that demonstrate the model's ability to capture freezing dynamics in a water–ice–air system. Finally, Chapter 7 summarizes the main findings and outlines several directions for future work.

Notation

Table 1.1: Parameters and variables in the phase–field model.

Symbol	**Description**
ϕ	Allen–Cahn order parameter for the solid–liquid interface.
ψ	Cahn–Hilliard order parameter for the liquid–gas interface.
μ_ϕ	Chemical potential associated with ϕ.
μ_ψ	Chemical potential associated with ψ.
λ_ϕ	Gradient–energy coefficient for ϕ in the free–energy functional.
λ_ψ	Gradient–energy coefficient for ψ in the free–energy functional.
M_ϕ	Mobility in the Cahn–Hilliard equation.
M_ψ	Mobility in the Allen–Cahn equation.
$r(\phi)$	Interpolation function for phase–dependent thermodynamic properties.
$r(\psi)$	Interpolation function for solid–liquid transition properties.
$W(\phi)$	Double–well potential (bulk free–energy density) for ϕ.
$W(\psi)$	Double–well potential (bulk free–energy density) for ψ.
q	SAV/IEQ auxiliary variable introduced to ensure energy stability.

Table 1.2: Thermodynamic quantities.

Symbol	Description
e	Internal energy per unit mass.
h	Enthalpy per unit mass.
f	Helmholtz free–energy density per unit mass.
g	Gibbs free energy per unit mass.
$\mathcal{F}$	Total free energy of the system.
s	Entropy per unit mass.
T	Temperature field.
T_M	Melting temperature at a flat interface and the reference pressure p_0.
T_σ	Actual melting temperature at a curved interface (Gibbs–Thomson relation).
T_p	Actual melting temperature at the interface under a pressure deviation $p_a = p - p_0$ relative to the reference pressure p_0 (Clausius–Clapeyron relation).
L	Latent heat.
c	Specific heat capacity.
c_i	Concentration of species i.
p	Pressure.
p_0	Reference pressure.
σ	Surface tension.
$\hat{f}$	Local free-energy density (used in gradient forces).
$\frac{\partial \hat{f}}{\partial \nabla \phi}$	Variational derivative of energy w.r.t. $\nabla\phi$.
$\frac{\partial \hat{f}}{\partial \nabla \psi}$	Variational derivative of energy w.r.t. $\nabla\psi$.

Table 1.3: Mixture and fluid properties.

Symbol	Description
ρ	Mixture density depending on ϕ and ψ.
ρ_l	Liquid density.
ρ_s	Solid density.
$\mathbf{v}$	Velocity field.
η	Dynamic viscosity.
k	Thermal conductivity.

Table 1.4: Differential operators and tensor notation used throughout the thesis.

Symbol	Description
∂_i	Partial derivative with respect to the i-th spatial coordinate.
$\nabla \cdot \mathbf{v}$	Divergence of a vector field.
$\nabla \cdot \boldsymbol{\Sigma}$	Divergence of the stress tensor: $(\nabla \cdot \boldsymbol{\Sigma})_i = \partial_j \Sigma_{ji}$.
$(\mathbf{v}\cdot\nabla)\mathbf{v}$	Convective acceleration, $[(\mathbf{v}\cdot\nabla)\mathbf{v}]_i = v_j\, \partial_j v_i$.
$(\nabla\mathbf{v})^T$	Transpose of the velocity-gradient tensor.
$\mathbf{D}(\mathbf{v})$	Symmetric strain-rate tensor: $\mathbf{D} = \frac{1}{2}(\nabla\mathbf{v} + (\nabla\mathbf{v})^T)$.
$(\mathbf{A}\cdot\mathbf{a})_i$	Action of a second-order tensor $\mathbf{A}$ on vector $\mathbf{a}$: $(\mathbf{A}\cdot\mathbf{a})_i = \sum_j A_{ij}a_j$.
$\mathbf{A} : \mathbf{B}$	Double contraction of tensors: $\mathbf{A} : \mathbf{B} = \sum_{i,j} A_{ij}B_{ij}$.
$\mathbf{a} \otimes \mathbf{b}$	Dyadic product: $(\mathbf{a} \otimes \mathbf{b})_{ij} = a_i b_j$.
Δu	Laplacian of a scalar field: $\Delta u = \partial_i \partial_i u$.
$\Delta\mu_\phi$	Laplacian of the chemical potential in Cahn–Hilliard.
$\int_\Omega (\cdot)\, d\Omega$	Volume integral over the domain Ω.
$\int_{\partial\Omega} (\cdot)\, ds$	Boundary integral using the outward normal $\mathbf{n}$.
$\mathbf{n}$	Outward unit normal vector on $\partial\Omega$.
κ	Interface curvature (positive for solid drops, negative for liquid drops).

Table 1.5: Notation in numerical discretization and weak formulations.

Symbol	Description
$\tilde{\phi}$	Test function for ϕ.
$\tilde{\psi}$	Test function for ψ.
$\tilde{\mu}_\phi$	Test function for μ_ϕ.
$\tilde{\mu}_\psi$	Test function for μ_ψ.
$\tilde{\mathbf{v}}$	Test function for velocity.
$\tilde{p}$	Test function for pressure.
$\tilde{T}$	Test function for temperature.
θ	Weight parameter in the θ-scheme.
Δt	Time-step size.
$\phi^{*,\theta}$	θ-interpolated phase field.
$\delta\phi$	Newton increment for ϕ.
$\delta\psi$	Newton increment for ψ.
$\delta\mathbf{v}$	Newton increment for velocity.

Table 1.6: Geometric notation and domain-related symbols.

Symbol	**Description**
Ω	Computational domain.
$\partial\Omega$	Boundary of the computational domain.
$\mathbf{n}$	Outward unit normal vector on $\partial\Omega$.
R	Droplet radius.
R_0	Initial droplet radius.
κ	Interface curvature.
p_a	Pressure deviation $p - p_0$.

Chapter 2

Thermodynamics Relations

In the realm of classical thermodynamics, the equilibrium state of a system can be described by four fundamental thermodynamic potentials: internal energy e, enthalpy h, Helmholtz free energy f, and Gibbs free energy g [6, 10]. Each of these potentials serves a different role and has a specific set of natural variables. Internal energy represents the total microscopic energy of a system, including both kinetic and potential contributions. Enthalpy extends this concept by including the pressure–volume work, making it particularly useful for processes occurring at constant pressure. Helmholtz free energy measures the maximum useful work (including volume work) that can be extracted from a closed system at constant temperature. Gibbs free energy, on the other hand, reflects the maximum non-expansion work and is widely used to determine the direction of spontaneous processes and phase transitions under constant temperature and pressure.

The differential formulations of these potentials, often referred to as the fundamental thermodynamic equations, reveal the underlying relationships between temperature, entropy, pressure, volume, and chemical composition [21]. These relations not only establish the basis for classical thermodynamic analysis, but also enable indirect measurements of quantities that are otherwise difficult to access. For example, the Maxwell relations—derived

from second-order derivative symmetry—provide a connection between entropy and more directly measurable variables such as pressure or volume. Similarly, the Clapeyron equation relates the slope of the phase boundary in the P–T diagram to the latent heat and specific volume change during a phase transition, allowing us to estimate enthalpy changes based on observable gradients [42, 63].

In multicomponent systems, additional terms must be introduced to account for the mass or mole numbers of each species. The conjugate variables to composition in these cases are the *chemical potentials*, which quantify the energy cost of adding material to the system. These are related through the Gibbs–Duhem relation, which imposes thermodynamic constraints among temperature, pressure, and chemical potentials [10]. This relation plays an essential role when considering mixtures such as water–air systems in icing phenomena.

In the subsequent sections, we will delve into the mathematical structure of these thermodynamic identities and explore how they can be utilized in a phase-field framework. Special emphasis will be placed on the derivation of thermodynamically consistent constitutive relations using the entropy inequality, and on the identification of key driving forces such as chemical potentials. These analyses will establish a rigorous foundation for constructing our multiphase model and will ensure that the governing equations remain consistent with the second law of thermodynamics. Unless otherwise stated, all thermodynamic quantities will be formulated on a per unit mass basis throughout this chapter.

2.1 Internal energy $e(s, \rho, c_i)$

Internal energy per unit mass, denoted as $e(s, \rho, c_i)$, is fundamentally linked to its natural state variables: entropy per unit mass s, density ρ, and concentrations c_i of chemical species.

The differential form of internal energy can be as:

$$de = \left.\frac{\partial e}{\partial s}\right|_{\rho,c_i} d\rho + \left.\frac{\partial e}{\partial \rho}\right|_{s,c_i} ds + \sum_i \left.\frac{\partial e}{\partial c_i}\right|_{s,\rho} dc_i. \tag{2.1}$$

We define temperature, pressure, and chemical potentials as

$$T = \left.\frac{\partial e}{\partial s}\right|_{\rho,c_i}, \frac{p}{\rho^2} = \left.\frac{\partial e}{\partial \rho}\right|_{s,c_i}, \mu_i = \left.\frac{\partial e}{\partial c_i}\right|_{s,\rho}. \tag{2.2}$$

Then the differential can be rewritten as

$$de = Tds + \frac{p}{\rho^2} d\rho + \sum_i \left.\frac{\partial e}{\partial c_i}\right|_{s,\rho} dc_i. \tag{2.3}$$

2.2 Enthalpy $h(s, p, c_i)$

Enthalpy is the sum of the system's internal energy and the product of pressure and volume:

$$h = e + pv,$$

where $v = \frac{1}{\rho}$ is the specific volume of the system.

We have

$$\begin{aligned} dh =& de(s, \rho, c_i) + d\left(\frac{p}{\rho}\right) \\ =& Tds + \frac{p}{\rho^2} d\rho + \sum_i \left.\frac{\partial e}{\partial c_i}\right|_{s,\rho} dc_i + \frac{1}{\rho} dp - \frac{p}{\rho^2} d\rho \\ =& Tds + \sum_i \left.\frac{\partial e}{\partial c_i}\right|_{s,\rho} dc_i + \frac{1}{\rho} dp. \end{aligned} \tag{2.4}$$

Enthalpy can also be expressed as a function of its natural state variables: entropy, pressure,

and mass concentrations. Thus, the differential of h can also be expressed as

$$dh(s, p, c_i) = \left.\frac{\partial h}{\partial s}\right|_{p,c_i} ds + \left.\frac{\partial h}{\partial p}\right|_{s,c_i} dp + \sum_i \left.\frac{\partial h}{\partial c_i}\right|_{s,p} dc_i. \tag{2.5}$$

Comparing Eqs. (2.4) and (2.5), we have

$$T = \left.\frac{\partial h}{\partial s}\right|_{p,c_i}, \frac{1}{\rho} = \left.\frac{\partial h}{\partial p}\right|_{s,c_i}, \mu = \left.\frac{\partial e}{\partial c_i}\right|_{s,\rho} = \left.\frac{\partial h}{\partial c_i}\right|_{s,p}. \tag{2.6}$$

2.3 Helmholtz free energy $f(T, \rho, c_i)$

Helmholtz free energy f is a thermodynamic potential that measures the useful work obtainable from a closed thermodynamic system at a constant temperature (isothermal), f is connected to e through the following relation.

$$f(T, \rho, c_i) = e(s, \rho, c_i) - Ts, \tag{2.7}$$

by taking the differential of both sides, we obtain

$$\begin{aligned} df =& de(s, \rho, c_i) - d(Ts) \\ =& Tds + \frac{p}{\rho^2} d\rho + \sum_i \left.\frac{\partial e}{\partial c_i}\right|_{s,\rho} dc_i - Tds - sdT \\ =& - sdT + \frac{p}{\rho^2} d\rho + \sum_i \left.\frac{\partial e}{\partial c_i}\right|_{s,\rho} dc_i. \end{aligned} \tag{2.8}$$

f can also be expressed as a function of its natural variables, namely temperature T, density ρ, and the set of concentrations c_i. Its total differential is given by

$$df(T, \rho, c_i) = \left.\frac{\partial f}{\partial T}\right|_{\rho,c_i} dT + \left.\frac{\partial f}{\partial \rho}\right|_{T,c_i} d\rho + \sum_i \left.\frac{\partial f}{\partial c_i}\right|_{T,p} dc_i. \tag{2.9}$$

Comparing Eqs. (2.8) and (2.9) we get

$$-s = \left.\frac{\partial f}{\partial T}\right|_{\rho,c_i}, \frac{p}{\rho^2} = \left.\frac{\partial f}{\partial \rho}\right|_{T,c_i} = \left.\frac{\partial e}{\partial \rho}\right|_{s,c_i}, \left.\frac{\partial f}{\partial c_i}\right|_{T,\rho} = \left.\frac{\partial e}{\partial c_i}\right|_{s,\rho}. \tag{2.10}$$

2.4 Gibbs free energy $g(T, p, c_i)$

Gibbs free energy is a thermodynamic potential that may be used to determine the maximum amount of work that can be accomplished at constant temperature and pressure by a closed system. Gibbs free energy is defined as follows:

$$g = e + \frac{p}{\rho} - Ts = h - Ts. \tag{2.11}$$

By taking the differential of both sides, we obtain

$$\begin{aligned} dg =& de(s,p,c_i) + d\left(\frac{p}{\rho}\right) - d(Ts) \\ =& Tds + \frac{p}{\rho^2}d\rho + \sum_i \left.\frac{\partial e}{\partial c_i}\right|_{s,\rho} dc_i + \frac{1}{\rho}dp - \frac{p}{\rho^2}d\rho - Tds - sdT \\ =& -sdT + \frac{1}{\rho}dp + \sum_i \left.\frac{\partial e}{\partial c_i}\right|_{s,\rho} dc_i. \end{aligned} \tag{2.12}$$

Gibbs free energy can also be expressed as a function of its natural variables, which are temperature T, pressure p, and concentrations c_i. Based on this, the total differential of g can be written as

$$dg(T,p,c_i) = \left.\frac{\partial g}{\partial T}\right|_{p,c_i} dT + \left.\frac{\partial g}{\partial p}\right|_{T,c_i} dp + \sum_i \left.\frac{\partial g}{\partial c_i}\right|_{T,p} dc_i, \tag{2.13}$$

comparing Eqs. (2.12) and (2.13), we get

$$-s = \left.\frac{\partial g}{\partial T}\right|_{p,c_i} = \left.\frac{\partial f}{\partial T}\right|_{\rho,c_i}, \frac{1}{\rho} = \left.\frac{\partial g}{\partial p}\right|_{T,c_i} = \left.\frac{\partial h}{\partial p}\right|_{s,c_i}, \left.\frac{\partial g}{\partial c_i}\right|_{t,p} = \left.\frac{\partial e}{\partial c_i}\right|_{s,p}. \tag{2.14}$$

Equations (2.6), (2.10), and (2.14), can be reorganized into

(i) $T = \left.\frac{\partial e}{\partial s}\right|_{\rho,c_i} = \left.\frac{\partial h}{\partial s}\right|_{p,c_i}$,

(ii) $-s = \left.\frac{\partial g}{\partial T}\right|_{p,c_i} = \left.\frac{\partial f}{\partial T}\right|_{\rho,c_i}$,

(iii) $\frac{1}{\rho} = \left.\frac{\partial h}{\partial p}\right|_{s,c_i} = \left.\frac{\partial g}{\partial p}\right|_{T,c_i}$,

(iv) $\frac{p}{\rho^2} = \left.\frac{\partial f}{\partial \rho}\right|_{T,c_i} = \left.\frac{\partial e}{\partial \rho}\right|_{s,c_i}$,

(v) $\mu_i = \left.\frac{\partial e}{\partial c_i}\right|_{s,\rho} = \left.\frac{\partial f}{\partial c_i}\right|_{T,\rho} = \left.\frac{\partial h}{\partial c_i}\right|_{s,p} = \left.\frac{\partial g}{\partial c_i}\right|_{T,p}$.

The Gibbs–Helmholtz relation can be obtained by taking the derivative of g/T with respect to T:

$$\left.\frac{\partial\left(\frac{g}{T}\right)}{\partial T}\right|_{p,c_i} = \frac{\left.\frac{\partial g}{\partial T}\right|_{p,c_i} \cdot T - g}{T^2} = \frac{-sT - g}{T^2} = -\frac{h}{T^2}.$$

A similar expression can be derived for the free energy by following the same approach:

$$\left.\frac{\partial\left(\frac{f}{T}\right)}{\partial T}\right|_{\rho,c_i} = \frac{\left.\frac{\partial f}{\partial T}\right|_{\rho,c_i} \cdot T - f}{T^2} = \frac{-sT - f}{T^2} = -\frac{e}{T^2}.$$

This section has laid the groundwork for the thermodynamic analysis of equilibrium systems that are spatially homogeneous. Through the derivation of the differential forms of the four thermodynamic potential energies, we have identified how these energies interplay. The equations highlight the dependence of each thermodynamic potential on entropy, pressure, density, temperature, and mass concentration, providing a comprehensive framework for understanding the energetic and entropic variations during phase changes.

Chapter 3

Three-phase solidification model

In our thermodynamically consistent framework, we develop a three-phase model that accounts for variations in density, a key factor in the solidification of water. Through rigorous derivation, we ensure that the model is thermodynamically consistent, i.e., it guarantees non-negative entropy production.

3.1 Three-phase model with variable density

Following a thermodynamically consistent framework that assures the system's conservation laws, we briefly describe the derivations of our model equations in the following section.

We assume the three-phase system to be quasi-incompressible [39]. That is, each individual phase is incompressible with a constant density, but the whole mixture may change volume due to phase transition and inter-phase diffusion. More specifically, the mixture density is a function of mixture composition as characterized by the phase-field variables:

$$\frac{1}{\rho(\phi,\psi)} = \frac{m_l}{\rho_l} + \frac{m_s}{\rho_s} + \frac{m_g}{\rho_g}, \tag{3.1}$$

where $m_l = r(\phi)r(\psi)$, $m_s = r(\phi)(1 - r(\psi))$, and $m_g = 1 - r(\phi)$ are the mass fractions of liquid, solid, and gas, respectively. Here $r(\cdot)$ is a smooth interpolant satisfying $r(0) = 0$, $r(1) = 1$, and $r'(0) = r'(1) = 0$. This interpolant ensures $\frac{\partial \rho}{\partial \phi} = \frac{\partial \rho}{\partial \psi} = 0$ in the bulk phases. Equation (3.1) follows from the fact that the volume of the mixture is the sum of the volumes of its three components.

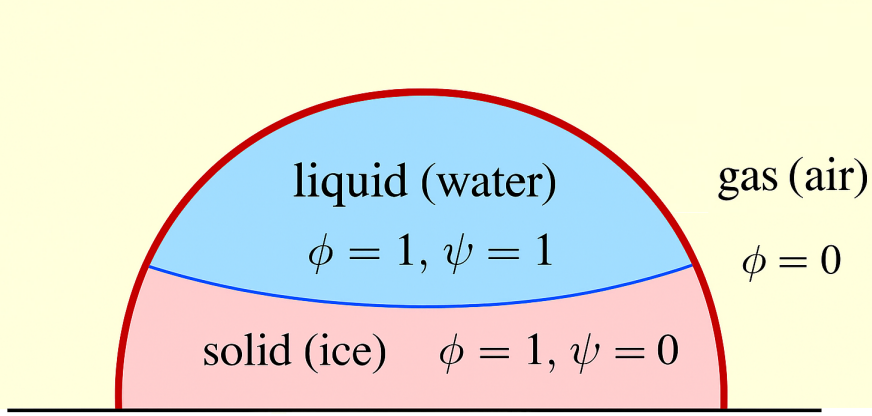

Figure 3.1: Schematic illustration of the phase distribution in the simplified three-phase model. The three phases—solid (ice), liquid (water), and gas (air)—are uniquely represented by two phase-field variables, ϕ and ψ. The regions are defined by the combinations: solid (ice), $\phi = 1$, $\psi = 0$; liquid (water), $\phi = 1$, $\psi = 1$; and gas (air), $\phi = 0$.

Figure 3.1 provides a visual representation of how the two order parameters, ϕ and ψ, distinguish the three phases in the present three-phase formulation. The variable ϕ serves as an indicator that separates the gas phase from the condensed phases: $\phi = 0$ corresponds to gas (air), while $\phi = 1$ designates the region occupied by either liquid water or solid ice. Within the condensed region, the variable ψ further differentiates the two states, taking the value $\psi = 0$ in the solid (ice) and $\psi = 1$ in the liquid (water). Each phase is therefore uniquely associated with a specific pair (ϕ, ψ), and the relationships shown in Figure 3.1 encode the structure that underlies the interpolations used in definition of density definition in (3.1) and the free energies to be discussed in the next subsection. This construction enables the model to track liquid–gas and solid–liquid interfaces simultaneously within a unified diffuse-interface framework.

3.1.1 Energies for a homogeneous system

Gibbs free energy, as defined in Eq. (2.11), is a thermodynamic potential that quantifies the maximum amount of useful work a closed system can accomplish when operating under constant temperature and pressure. In our model, Gibbs free energy is carefully constructed to capture the intricacies of phase transitions, particularly those involving water-ice and water-air interactions. This formulation allows us to incorporate both interface dynamics and bulk phase behavior by leveraging the Allen-Cahn and Cahn-Hilliard equations, ensuring consistency with the second law of thermodynamics. Furthermore, by taking into account the compositional dependence of density, the model handles the quasi-incompressible nature of the three-phase mixture in a physically consistent manner. Following the quasi-incompressible phase-field framework for a two-phase system by Anderson et al. [4], the homogeneous Gibbs free energy per unit mass is constructed as:

$$\begin{aligned} g(p,T,\phi,\psi) = &[h_0 + r(\phi)r(\psi)L - c(\phi,\psi)T_M]\left(1-\frac{T}{T_M}\right) \\ &- c(\phi,\psi)T\ln\frac{T}{T_M} + \frac{p-p_0}{\rho(\psi,\phi)}. \end{aligned} \tag{3.2}$$

Here, $c(\phi,\psi)$ denotes the specific heat of the mixture, T_M is the melting temperature at the reference pressure p_0, and L is the latent heat of fusion at T_M and p_0.

Based on the definition of Helmholtz free energy, we subtract the mechanical contribution from the Gibbs free energy to obtain

$$f(p,T,\phi,\psi) = g(p,T,\phi,\psi) - \frac{p}{\rho(\phi,\psi)}. \tag{3.3}$$

It should be noted that the Helmholtz free energy f here is expressed as a function of pressure p and temperature T, rather its natural state variables s and ρ, as done in the classical formulation. This choice is due to the fact that density ρ, as a function of the phase variables ϕ and ψ, is no longer an independent thermodynamic variable in our system. As

a result, certain differential thermodynamic relations derived in Chapter 2, which rely on (s, ρ) as independent variables, are not directly applicable to the current expression of f.

The internal energy e can be obtained as follows:

$$\begin{aligned} e(p, T, \phi, \psi) =& h - \frac{p}{\rho} \\ =& - T^2 \frac{\partial \left(g/T \right)}{\partial T} - \frac{p}{\rho} \\ =& e_0 + r(\phi) r(\psi) L + c(\phi, \psi)(T - T_M) - \frac{p_0}{\rho(\phi, \psi)} \end{aligned} \tag{3.4}$$

where we have used the Gibbs-Helmholtz relation (3.3). In this internal energy, we can identify the Latent heat term $r(\phi)r(\psi)L$ that is activated in the water phase and the term $c(\phi, \psi)(T - T_M)$ that is associated with heat capacity and temperature. It should be noted that

$$\left. \frac{\partial e}{\partial p} \right|_{T, \phi, \psi} = 0, \tag{3.5}$$

which is a consequence of the quasi-incompressibility. It is easy to see that the Helmholtz free energy (3.3) and entropy (3.6) are both independent of pressure p as well.

Entropy is a key indicator to ensure that the three-phase solidification phase field model involving water, ice, and air obeys the second law of thermodynamics. According to this law, an isolated system's total entropy can never drop over time and reaches its maximum at equilibrium. In order to ensure thermodynamic consistency, our model takes entropy into account and guarantees that all processes, such as the water-ice phase transition and the dynamics of the water-air interface, are oriented toward raising the total entropy. The entropy can be computed from e and f:

$$s(p, T, \phi, \psi) = \frac{e - f}{T} = \left[e_0 + r(\phi) r(\psi) L \right] \frac{1}{T_M} + c(\phi, \psi) \ln \frac{T}{T_M}. \tag{3.6}$$

3.1.2 Energies for a systems with diffuse interface

In classical sharp-interface models, material properties such as density, entropy, or composition change discontinuously across a mathematically idealized interface. As shown in Figure 3.2, this representation assumes that the interface has no thickness, which causes difficulties in numerical implementation and in providing a clear thermodynamic description of the motion of the interface, such as relating the interface velocity to the local variations in chemical potential, temperature, and curvature.

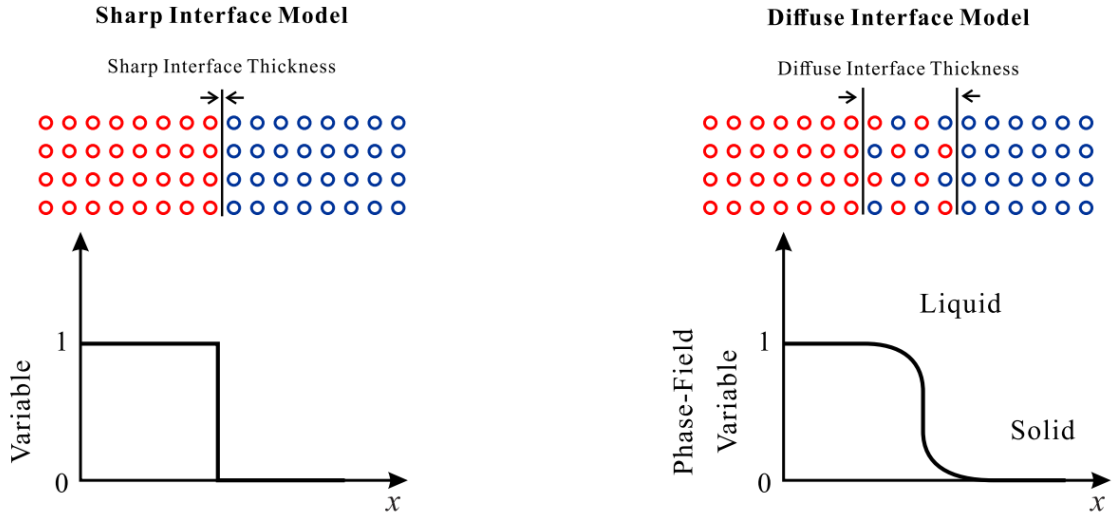

Figure 3.2: Properties are discontinuous at the sharp interface, but vary continuously across the diffuse interface.

In contrast, the diffuse interface approach provides a more natural and physically consistent framework by allowing these properties to vary smoothly across a finite interfacial region [3, 4]. This smooth transition is modeled through additional contributions to the free energy that include a double-well potential and gradient terms in ϕ and ψ, allowing the system to capture interfacial dynamics in an energetically consistent way.

Following Guo and Lin [23], we extend the Gibbs free energy to account for the diffuse interface:

$$\hat{g}(p, T, \phi, \psi, \nabla\phi, \nabla\psi) = g(p, T, \phi, \psi) + g^*(\phi, \psi, \nabla\phi, \nabla\psi), \tag{3.7}$$

where $\hat{g}$ is the total free energy for the non-homogeneous three-phase system, g is the classical part corresponding to a homogeneous system, and g^* is the non-classical contribution that arises from the non-homogeneity brought in by the diffuse interface.

Similarly, we extend the Helmholtz free energy, internal energy, and entropy as

$$\hat{f}(p,T,\phi,\psi,\nabla\phi,\nabla\psi) = f(p,T,\phi,\psi) + f^*(\phi,\psi,\nabla\phi,\nabla\psi), \tag{3.8}$$

$$\hat{e}(p,T,\phi,\psi,\nabla\phi,\nabla\psi) = e(p,T,\phi,\psi) + e^*(\phi,\psi,\nabla\phi,\nabla\psi), \tag{3.9}$$

$$\hat{s}(p,T,\phi,\psi,\nabla\phi,\nabla\psi) = s(p,T,\phi,\psi) + s^*(\phi,\psi,\nabla\phi,\nabla\psi). \tag{3.10}$$

The extended energies satisfy relations analogous to those of the classical energies,

$$\hat{f} = \hat{g} - \frac{p}{\rho}, \tag{3.11}$$

and

$$\hat{e} = \hat{f} - T\hat{s}. \tag{3.12}$$

It follows that

$$f^* = g^*, \qquad e^* = f^* - Ts^*.$$

It should be noted that the non-classical part f^* represents the excessive energy that contributes to surface tension. For simplicity, we assume that all non-classical terms are independent of T. This corresponds to a surface tension that is independent of T. This T-independence requires $s^* = 0$ (i.e., $\hat{s} = s$) and therefore $e^* = f^*$.

Different formulations exist in the literature. For instance, Guo and Lin [23] consider a temperature-dependent f^* by allowing $s^* \neq 0$, which leads to a surface tension that varies with temperature. This corresponds to a temperature-independent surface tension, allowing the model to capture thermocapillarity.

Following the standard form of mixing energy in phase-field models [3, 53] , we adopt

$$f^* = g^* = e^* = \lambda_\phi \left(W(\phi) + \tfrac{1}{2}|\nabla\phi|^2 \right) + r(\phi)\, \lambda_\psi \left(W(\psi) + \tfrac{1}{2}|\nabla\psi|^2 \right), \tag{3.13}$$

where $W(\phi) = \dfrac{\phi^2(1-\phi^2)}{\epsilon^2}$ is the double-well potential, and λ_ϕ, λ_ψ are the mixing energy coefficients associated with the ϕ and ψ interfaces, respectively. The function $r(\phi)$ ensures that ψ interface (i.e., the solid-liquid interface) only exists in the region with $\phi = 1$.

3.1.3 Conservation laws

The conservation laws play a pivotal role in phase-field modeling, encompassing mass, momentum, energy, and entropy within the system. In the context of three-phase solidification, we must derive the governing equations that comply with the fundamental conservation principles. These include the evolution equations for the gas interface (reprensented by ϕ), the solid-lquid interface (represented by ψ), the continuity equation, the momentum equation, and the energy and entropy equations.

Let $V(t)$ be an arbitrary material volume that moves with velocity $\mathbf{v}(\mathbf{x}, t)$. Then the mass, momentum, total energy, and entropy associated with this material volume are given by

$$\mathcal{M} = \int_{V(t)} \rho d\mathbf{x}, \tag{3.14}$$

$$\mathcal{P} = \int_{V(t)} \rho \mathbf{v} d\mathbf{x}, \tag{3.15}$$

$$\mathcal{E} = \int_{V(t)} \rho \left(\hat{e} + \frac{|\mathbf{v}|^2}{2} \right) d\mathbf{x}, \tag{3.16}$$

$$\mathcal{S} = \int_{V(t)} \rho \hat{s} d\mathbf{x}. \tag{3.17}$$

Here the total energy includes contributions from the internal energy $\rho\hat{e}$ and the kinetic energy $\frac{1}{2}\rho|\mathbf{v}|^2$.

Mass conservation requires

$$\frac{d}{dt}\mathcal{M} = 0. \tag{3.18}$$

The rate of change of momentum is determined by the external force on $V(t)$:

$$\frac{d}{dt}\mathcal{P} = \int_{\partial V(t)} \mathbf{n}\cdot\boldsymbol{\Sigma} d\mathbf{x}, \tag{3.19}$$

where $\mathbf{n}$ is the outward pointing normal, $\boldsymbol{\Sigma}$ is the Cauchy stress, and we have ignored the body force. The total energy is affected by external work and energy flux:

$$\frac{d}{dt}\mathcal{E} = \int_{\partial V(t)} \mathbf{n}\cdot(\boldsymbol{\Sigma}\cdot\mathbf{v} - \mathbf{q}_E - \mathbf{q}_E^{nc}) ds, \tag{3.20}$$

where $\mathbf{n}\cdot\boldsymbol{\Sigma}\cdot\mathbf{v}$ is the work done by the external force (which equals $\mathbf{n}\cdot\boldsymbol{\Sigma}$) on $\partial V(t)$, $\mathbf{q}_E$ is the classical heat flux, and $\mathbf{q}_E^{nc}$ is the non-classical heat flux associated with diffuse interface. Similarly we have the following equation for entropy:

$$\frac{d}{dt}\mathcal{S} = \int_{\partial V(t)} \mathbf{n}\cdot\Big(-\frac{\mathbf{q}_E}{T} - \mathbf{q}_s^{nc}\Big)\, ds + \int_{V(t)} \dot{S}_{\text{prod}}\, d\mathbf{x}, \tag{3.21}$$

where $\frac{\mathbf{q}_E}{T}$ is the entropy flux associated with the heat flux $\mathbf{q}_E$, $\mathbf{q}_s^{nc}$ is the non-classical entropy flux, and $\dot{S}_{prod}$ is the irreversible entropy production.

For a sufficiently smooth scalar, vector, or tensor field $f(\mathbf{x},t)$ advected by velocity $\mathbf{v}(\mathbf{x},t)$, the material derivative is given by $\frac{Df}{Dt} = \frac{\partial f}{\partial t} + \mathbf{v}\cdot\nabla f$. It is easy to see that the material derivative satisfies the product rule: $\frac{D(fg)}{Dt} = \frac{\partial (fg)}{\partial t} + \mathbf{v}\cdot\nabla(fg) = f\frac{\partial g}{\partial t} + \frac{\partial f}{\partial t}g + \mathbf{v}\cdot(f\nabla g + g\nabla f) = f\frac{Dg}{dt} + \frac{Df}{Dt}g$.

To put the conservation laws into differentia equations, we also need the following Reynolds transport theorem.

Theorem 3.1 (Reynolds transport theorem)**.** *Let $f(\mathbf{x},t)$ be smooth in the Eulerian frame,*

and let $V(t)$ be a control volume moving with a smooth velocity field $\mathbf{v}$*. Then*

$$\frac{d}{dt}\int_{V(t)} f\,d\mathbf{x} = \int_{V(t)}\left(\frac{\partial f}{\partial t} + \nabla\cdot(f\mathbf{v})\right)d\mathbf{x} = \int_{V(t)}\left(\frac{Df}{Dt} + f\,\nabla\cdot\mathbf{v}\right)d\mathbf{x}. \tag{3.22}$$

Applying Theorem 3.1 to Eq. (3.17) and considering that the control volume $V(t)$ is arbitrary, we get the following continuity equation for mass conservation in differential form:

$$\frac{D\rho}{Dt} + \rho\,\nabla\cdot\mathbf{v} = 0. \tag{3.23}$$

Combining (3.23) and (3.22), we also arrive at the following transport theorem for quantities per unit mass.

Theorem 3.2 (Reynolds transport theorem for quantities per unit mass)**.** *Let $f(\mathbf{x},t)$ be smooth in the Eulerian frame, let ρ be the density satisfying the continuity equation*(3.23)*, and let $V(t)$ be a control volume moving with a smooth velocity field* $\mathbf{v}$*. Then*

$$\frac{d}{dt}\int_{V(t)} \rho f\,d\mathbf{x} = \int_{V(t)}\left(\rho\frac{Df}{Dt} + \frac{D\rho}{Dt}f + \rho f\,\nabla\cdot\mathbf{v}\right)d\mathbf{x} = \int_{V(t)}\rho\frac{Df}{Dt}\,d\mathbf{x}. \tag{3.24}$$

With the help of Theorem 3.2, the integral-form conservations laws (3.19), (3.20), and (3.21) can be cast into differential equations:

$$\rho\frac{D\mathbf{v}}{Dt} = \nabla\cdot\boldsymbol{\Sigma}, \tag{3.25}$$

$$\rho\,\frac{D}{Dt}\left(\hat{e} + \frac{|\mathbf{v}|^2}{2}\right) = \nabla\cdot\left(\boldsymbol{\Sigma}\cdot\mathbf{v} - \mathbf{q}_E - \mathbf{q}_E^{nc}\right), \tag{3.26}$$

$$\rho\,\frac{D\hat{s}}{Dt} = \nabla\cdot\left(-\frac{\mathbf{q}_E}{T} - \mathbf{q}_s^{nc}\right) + \dot{S}_{\text{prod}}, \tag{3.27}$$

where we have used the divergence theorem to transform surface integrals into volume integrals of divergence.

By taking the dot product between the momentum equation (3.25) and $\mathbf{v}$, we get the fol-

lowing conservation law for kinetic energy

$$\rho \frac{D(\frac{1}{2}|\mathbf{v}|^2)}{Dt} = \nabla \cdot \Sigma \cdot \mathbf{v}, \tag{3.28}$$

where we have used the product rule $\frac{D|\mathbf{v}|^2}{Dt} = \frac{D(\mathbf{v}\cdot\mathbf{v})}{Dt} = 2\frac{D\mathbf{v}}{Dt} \cdot \mathbf{v}$. Combining this equation with the total energy equation (3.26), we arrive at the conservation law for internal energy:

$$\rho \frac{D\hat{e}}{Dt} = -\nabla \cdot (\mathbf{q}_E + \mathbf{q}_E^{nc}) + \nabla \mathbf{v} : \mathbf{\Sigma}, \tag{3.29}$$

where we have used the identify $\nabla \cdot (\mathbf{\Sigma} \cdot \mathbf{v}) = (\nabla \cdot \mathbf{\Sigma}) \cdot \mathbf{v} + \nabla \mathbf{v} : \mathbf{\Sigma}$.

We also need equations for ϕ and ψ to describe the evolution of mixture composition. The phase field ϕ represents the interface between gas and the condensed phases (liquid and solid). Since the total mass of air must be conserved, we assume ϕ evolves according the following conserved dynamics:

$$\rho \frac{D\phi}{Dt} = -\nabla \cdot \mathbf{j}_\phi, \tag{3.30}$$

where $\mathbf{j}_\phi$ is the diffusive flux of ϕ. This equation ensures that the total mass of air remains conserved in the computational domain. Integrating equation (3.30) over the computational domain Ω and applying the divergence theorem, the flux term transforms into a surface integral, which vanishes under appropriate boundary conditions (i.e., $\mathbf{n}\cdot\mathbf{j}_\phi$=0 on $\partial\Omega$), thereby conserving $\int_\Omega \rho\phi d\mathbf{x}$.

For the liquid-solid interface, denoted by ψ, we account for the phase transition that is not conserved. Thus, we include a source term:

$$\rho \frac{D\psi}{Dt} = j_\psi, \tag{3.31}$$

where j_ψ is a nonzero source that reflects the phase transformation process between liquid and solid.

Now we have gathered all the governing equations that our three-phase system has to satisfy: phase-field equations (3.30) and (3.31), continuity equation (3.23), momentum equation (3.25), energy equation (3.26) or (3.29), and entropy equation (3.27). It should be noted that the entropy equation (3.27) is redundant and we use it to determine entropy production $\dot{S}_{prod}$. The terms $\mathbf{\Sigma}$, $\mathbf{q}_E$, $\mathbf{q}_E^{nc}$, and $\mathbf{q}_s^{nc}$ are to be determined so that $\dot{S}_{prod} \geq 0$ is guaranteed.

3.1.4 Entropy generation

In this subsection we will derive entropy production $\dot{S}_{prod}$, which can be obtained by multiplying Eq. (3.27) by T and subtracting Eq. (3.29):

$$T\dot{S}_{prod} = \rho T\frac{D\hat{s}}{Dt} - \rho\frac{D\hat{e}}{dt} + \nabla\mathbf{v} : \mathbf{\Sigma} + \nabla\cdot(T\mathbf{q}_s^{nc} - \mathbf{q}_E^{nc}) - \nabla T\cdot(\frac{\mathbf{q}_E}{T} + \mathbf{q}_s^{nc}). \tag{3.32}$$

From Eq. (3.7), we have

$$\begin{aligned} d\hat{g} &= \frac{\partial g}{\partial p}\bigg|_{T,\phi,\psi} dp + \frac{\partial g}{\partial T}\bigg|_{p,\phi,\psi} dT + \frac{\partial\hat{g}}{\partial\phi}d\phi + \frac{\hat{g}}{\partial\psi}d\psi + \frac{\partial\hat{g}}{\partial\nabla\phi}\cdot d\nabla\phi + \frac{\partial\hat{g}}{\nabla\psi}\cdot d\nabla\psi \\ &= \frac{1}{\rho}dp - sdT + \frac{\partial\hat{g}}{\partial\phi}d\phi + \frac{\hat{g}}{\partial\psi}d\psi + \frac{\partial\hat{g}}{\partial\nabla\phi}\cdot d\nabla\phi + \frac{\partial\hat{g}}{\nabla\psi}\cdot d\nabla\psi, \end{aligned} \tag{3.33}$$

where we have used the relations in (2.14) with ϕ and ψ playing the roles of concentrations c_i. It follows that

$$\begin{aligned} d\hat{e} &= d(\hat{f} - T\hat{s}) = d(\hat{g} - \frac{p}{\rho} + T\hat{s}) = d\hat{g} - \frac{dp}{\rho} + \frac{p}{\rho^2}d\rho + Td\hat{s} + \hat{s}dT \\ &= Td\hat{s} + \frac{p}{\rho^2}d\rho + \frac{\partial\hat{g}}{\partial\phi}d\phi + \frac{\hat{g}}{\partial\psi}d\psi + \frac{\partial\hat{g}}{\partial\nabla\phi}\cdot d\nabla\phi + \frac{\partial\hat{g}}{\nabla\psi}\cdot d\nabla\psi, \end{aligned} \tag{3.34}$$

where we have used $\hat{s} = s$ stem from our assumption of T-independent non-classical energy.

From this differential form above, we obtain the following material derivative for internal

energy:

$$\begin{aligned}
\rho\frac{D\hat{e}}{Dt} &= \rho T\frac{D\hat{s}}{Dt} + \frac{p}{\rho}\frac{D\rho}{Dt} + \rho\left[\frac{\partial\hat{g}}{\partial\phi}\frac{D\phi}{Dt} + \frac{\hat{g}}{\partial\psi}\frac{D\psi}{Dt} + \frac{\partial\hat{g}}{\partial\nabla\phi}\cdot\frac{D\nabla\phi}{Dt} + \frac{\partial\hat{g}}{\partial\nabla\psi}\cdot\frac{D\nabla\psi}{Dt}\right] \\
&= \rho T\frac{D\hat{s}}{Dt} - p\nabla\cdot\mathbf{v} + \rho\frac{\partial\hat{g}}{\partial\phi}\frac{D\phi}{Dt} + \rho\frac{\partial\hat{g}}{\partial\psi}\frac{D\psi}{Dt} + \rho\frac{\partial\hat{g}}{\partial\nabla\phi}\cdot\nabla\frac{D\phi}{Dt} + \rho\frac{\partial\hat{g}}{\partial\nabla\psi}\cdot\nabla\frac{D\psi}{Dt} \\
&- \rho\frac{\partial\hat{g}}{\partial\nabla\phi}\cdot\nabla\mathbf{v}\cdot\nabla\phi - \rho\frac{\partial\hat{g}}{\partial\nabla\psi}\cdot\nabla\mathbf{v}\cdot\nabla\psi \\
&= \rho T\frac{D\hat{s}}{Dt} + \left[\frac{\partial\hat{g}}{\partial\phi} - \frac{1}{\rho}\nabla\cdot\left(\rho\frac{\partial\hat{g}}{\partial\nabla\phi}\right)\right]\rho\frac{D\phi}{Dt} + \left[\frac{\partial\hat{g}}{\partial\psi} - \frac{1}{\rho}\nabla\cdot\left(\rho\frac{\partial\hat{g}}{\partial\nabla\psi}\right)\right]\rho\frac{D\psi}{Dt} \\
&+ \nabla\cdot\left(\rho\frac{\partial\hat{g}}{\partial\nabla\phi}\frac{D\phi}{Dt} + \rho\frac{\partial\hat{g}}{\partial\nabla\psi}\frac{D\psi}{Dt}\right) - \left(\rho\frac{\partial\hat{g}}{\partial\nabla\phi}\otimes\nabla\phi + \rho\frac{\partial\hat{g}}{\partial\nabla\psi}\otimes\nabla\psi\right) : \nabla\mathbf{v} - p\nabla\cdot\mathbf{v}.
\end{aligned} \tag{3.35}$$

Here we have used the continuity equation $\frac{D\rho}{Dt} = -\rho\nabla\cdot\mathbf{v}$ in the first equality, the relation $\frac{D\nabla\phi}{Dt} = \frac{\partial\nabla\phi}{\partial t} + \mathbf{v}\cdot\nabla\nabla\phi = \nabla\frac{\partial\phi}{Dt} + \nabla(\mathbf{v}\cdot\nabla\phi) - \nabla\mathbf{v}\cdot\nabla\phi = \nabla\frac{D\phi}{Dt} - \nabla\mathbf{v}\cdot\nabla\phi$ in the second equality, and the product rule $\nabla\cdot\left(\rho\frac{\partial\hat{g}}{\partial\nabla\phi}\frac{D\phi}{Dt}\right) = \nabla\cdot\left(\rho\frac{\partial\hat{g}}{\partial\nabla\phi}\right)\frac{D\phi}{Dt} + \rho\frac{\partial\nabla\hat{g}}{\partial\phi}\cdot\nabla\frac{D\phi}{Dt}$ in the third equality. Similar relations are used for ψ. From this equation we can identify the chemical potentials

$$\mu_\phi = \frac{\partial\hat{g}}{\partial\phi} - \frac{1}{\rho}\nabla\cdot\left(\rho\frac{\partial\hat{g}}{\partial\nabla\phi}\right), \tag{3.36}$$

$$\mu_\psi = \frac{\partial\hat{g}}{\partial\psi} - \frac{1}{\rho}\nabla\cdot\left(\rho\frac{\partial\hat{g}}{\partial\nabla\psi}\right) \tag{3.37}$$

and the elastic stress due to the diffuse interface

$$\mathbf{T}_e = -\left(\rho\frac{\partial\hat{g}}{\partial\nabla\phi}\otimes\nabla\phi + \rho\frac{\partial\hat{g}}{\partial\nabla\psi}\otimes\nabla\psi\right). \tag{3.38}$$

Plugging Eq. (3.35) into Eq. (3.32), we obtain

$$\begin{aligned}
T\dot{S}_{prod} &= -\mu_\phi\rho\frac{D\phi}{Dt} - \mu_\psi\rho\frac{D\phi}{Dt} + (\boldsymbol{\Sigma} - \mathbf{T}_e) : \nabla\mathbf{v} + p\nabla\cdot\mathbf{v} \\
&- \nabla T\cdot\left(\frac{\mathbf{q}_E}{T} + \mathbf{q}_s^{nc}\right) - \nabla\cdot\left(\rho\frac{\partial\hat{g}}{\partial\nabla\phi}\frac{D\phi}{Dt} + \rho\frac{\partial\hat{g}}{\partial\nabla\psi}\frac{D\psi}{Dt} + \mathbf{q}_E^{nc} - T\mathbf{q}_s^{nc}\right).
\end{aligned} \tag{3.39}$$

Considering the phase-field equations (3.30) and (3.31), entropy production can be further written into

$$T\dot{S}_{prod} = \underbrace{-\nabla\mu_\phi \cdot \mathbf{j}_\phi}_{A} \underbrace{-\mu_\psi j_\psi}_{B} + \underbrace{(\boldsymbol{\Sigma} - \mathbf{T}_e) : \nabla\mathbf{v} + p\nabla\cdot\mathbf{v}}_{\Phi}$$
$$\underbrace{-\nabla\cdot\left(\rho\frac{\partial\hat{g}}{\partial\nabla\phi}\frac{D\phi}{Dt} + \rho\frac{\partial\hat{g}}{\partial\nabla\psi}\frac{D\psi}{Dt} + \mathbf{q}_E^{nc} - T\mathbf{q}_s^{nc} - \mu_\phi\mathbf{j}_\phi\right)}_{C} \underbrace{-\nabla T\cdot\left(\frac{\mathbf{q}_E}{T} + \mathbf{q}_s^{nc}\right)}_{D}. \quad (3.40)$$

Each term on the right-hand side of this equation is written as a product of a generalized force and generalized flux. A *sufficient* condition for $\dot{S}_{prod} \geq 0$ is that each term (i.e., A,B, C,D, and Ψ) is non-negative. In the following we will interrogate each term to obtain addmissible constitutive relations that yield non-negative entropy production.

Term A. This term is the dissipation caused from the Cahn-Hilliard equation. The simplest choice that guarantees $A \geq 0$ is the linear relationship between the generalized flux $\mathbf{j}_\phi$ and the generalized force $-\nabla\mu_\phi$:

$$\mathbf{j}_\phi = -M_\phi\nabla\mu_\phi, \quad (3.41)$$

where M_ϕ, a.k.a. the mobility parameter for ϕ, is a positive phenomenological parameter.

Term B. This is the disspation from the Allen-Cahn equation. Following the linear response assumption as in term A, $B \geq 0$ is guaranteed by

$$j_\psi \;=\; -M_\psi\,\mu_\psi, \quad (3.42)$$

where $M_\psi > 0$ is the mobility parameter for ψ.

Term Φ.. This is the viscous dissipation. The Cauchy stress $\boldsymbol{\Sigma}$ is composed of a isotropic pressure term, an elastic stress given by (3.38), and a viscous stress $\mathbf{T}_v$ to be determined:

$$\boldsymbol{\Sigma} = -p\mathbf{I} + \mathbf{T}_e + \mathbf{T}_v.$$

This leads to the familiar viscous dissipation:

$$\Phi = (-p\mathbf{I} + \mathbf{T}_v) : \nabla\mathbf{v} + p\nabla\cdot\mathbf{v} = \mathbf{T}_v : \nabla\mathbf{v},$$

where we have used the identity $\mathbf{I} : \nabla\mathbf{v} = \nabla\cdot\mathbf{v}$. The strain rate tensor $\nabla\mathbf{v}$ can be written as the sum of an isotropic part $\frac{1}{3}(\nabla\cdot\mathbf{v})\mathbf{I}$ and a deviatoric (traceless) part $\nabla\mathbf{v} - \frac{1}{3}(\nabla\cdot\mathbf{v})\mathbf{I}$. Thus the viscous dissipation can be further written as

$$\begin{aligned}\Phi &= \mathbf{T}_v : [\nabla\mathbf{v} - \frac{1}{3}(\nabla\cdot\mathbf{v})\mathbf{I}] + \frac{1}{3}\mathbf{T}_v : (\nabla\cdot\mathbf{v})\mathbf{I} \\ &= \frac{1}{2}\mathbf{T}_v : [\nabla\mathbf{v} + \nabla\mathbf{v}^T - \frac{2}{3}(\nabla\cdot\mathbf{v})\mathbf{I}] + \frac{1}{3}\mathbf{T}_v : (\nabla\cdot\mathbf{v})\mathbf{I},\end{aligned}$$

where we have used the fact that $\mathbf{T}_v$ is symmetric. Obviously, $\Phi \geq 0$ is guaranteed by the classical two-parameter viscous stress for isotropic Newtonian fluids:

$$\mathbf{T}_v = \eta[\nabla\mathbf{v} + \nabla\mathbf{v}^T - \frac{2}{3}(\nabla\cdot\mathbf{v})\mathbf{I}] + \kappa(\nabla\cdot\mathbf{v})\mathbf{I}, \tag{3.43}$$

where $\eta \geq 0$ is the shear viscosity and $\kappa \geq 0$ is the bulk viscosity. The total stress then reads

$$\boldsymbol{\Sigma} = -p\mathbf{I} + \eta[\nabla\mathbf{v} + \nabla\mathbf{v}^T - \frac{2}{3}(\nabla\cdot\mathbf{v})\mathbf{I}] + \kappa(\nabla\cdot\mathbf{v})\mathbf{I} - \left(\rho\frac{\partial\hat{g}}{\partial\nabla\phi}\otimes\nabla\phi + \rho\frac{\partial\hat{g}}{\partial\nabla\psi}\otimes\nabla\psi\right). \tag{3.44}$$

Term C. This is a divergence term related to flux. Since flux is reversible, this term should not contribute to the irreversible entropy production, i.e., we have $C = 0$. Since entropy has no non-classical part ($s^* = 0$), it makes sense to assume zero non-classical entropy flux:

$$\mathbf{q}_s^{nc} = 0. \tag{3.45}$$

Then $C = 0$ is satisfied by the following non-classical heat flux:

$$\mathbf{q}_E^{nc} = -\rho \frac{\partial \hat{g}}{\partial \nabla \phi} \frac{D\phi}{Dt} - \rho \frac{\partial \hat{g}}{\partial \nabla \psi} \frac{D\psi}{Dt} + \mu_\phi \mathbf{j}_\phi, \tag{3.46}$$

Term D. This is the dissipation from thermal diffusion. With $\mathbf{q}_s^{nc} = 0$, $D \geq 0$ is guaranteed by the Fourier's law for the classical heat flux:

$$\mathbf{q}_E = -k \nabla T. \tag{3.47}$$

The constitutive relations given by (3.41, 3.42, 3.44–3.47) guarantees nonegative entropy production:

$$T \dot{S}_{\text{prod}} = M_\phi |\nabla \mu_\phi|^2 + M_\psi \mu_\psi^2 + \frac{1}{2}\eta \left\| \nabla \mathbf{v} + \nabla \mathbf{v}^T - \frac{2}{3}(\nabla \cdot \mathbf{v})\mathbf{I} \right\|^2 + \kappa (\nabla \cdot \mathbf{v})^2 + \frac{k}{T} |\nabla T|^2 \geq 0. \tag{3.48}$$

It should be noted that, from the perspective of non-negative entropy production, the choice of these constitutive relations is not unique.

3.2 Governing equations

With the constitutive relations (3.41, 3.42, 3.44–3.47) from Sec. 3.1.4, the governing equations can be organized as follows.

The **Cahnh-Hilliard equation** can be obtained by plugging (3.41) into (3.30):

$$\rho \frac{D\phi}{Dt} = \nabla \cdot (M_\phi \nabla \mu_\phi). \tag{3.49}$$

Here the chemical potential μ_ϕ can be obtained by plugging the Gibbs energies defined in

(3.7,3.2,3.13) into Eq. (3.36):

$$\begin{aligned}\mu_\phi =& \frac{\partial \hat{g}}{\partial \phi} - \frac{1}{\rho}\nabla\cdot\left(\rho\frac{\partial \hat{g}}{\partial \nabla\phi}\right) = \frac{\partial (g+g^*)}{\partial \phi} - \frac{1}{\rho}\nabla\cdot\left(\rho\frac{\partial g^*}{\partial \nabla\phi}\right)\\ =& \left[r'(\phi)r(\psi)L - \frac{\partial c}{\partial \phi}T_M\right]\left(1-\frac{T}{T_M}\right) - \frac{\partial c}{\partial \phi}T\ln\frac{T}{T_M} - \frac{p-p_0}{\rho^2}\frac{\partial \rho}{\partial \phi}\\ &+ \lambda_\phi W'(\phi) - \frac{1}{\rho}\nabla\cdot(\rho\lambda_\phi\nabla\phi) + r'(\phi)\lambda_\psi(W(\psi)+\frac{1}{2}|\nabla\psi|^2).\end{aligned} \tag{3.50}$$

The **Allen-Cahn equation** can be obtained by plugging (3.42) into (3.31):

$$\rho\frac{D\psi}{Dt} = -M_\psi\mu_\psi, \tag{3.51}$$

where the chemical potential μ_ψ can be obtained similar to μ_ϕ expect for using (3.37) instead of (3.36):

$$\begin{aligned}\mu_\psi =& \left[r(\phi)r'(\psi)L - \frac{\partial c}{\partial \psi}T_M\right]\left(1-\frac{T}{T_M}\right) - \frac{\partial c}{\partial \psi}T\ln\frac{T}{T_M} - \frac{p-p_0}{\rho^2}\frac{\partial \rho}{\partial \psi}\\ &+ r(\phi)\lambda_\psi W'(\psi) - \frac{1}{\rho}\nabla\cdot(\rho r(\phi)\lambda_\psi\nabla\psi).\end{aligned} \tag{3.52}$$

With the energies given by (3.7,3.2,3.13), the elastic stress (3.38) can be updated to

$$\mathbf{T}_e = -\left(\rho\lambda_\phi\nabla\phi\otimes\nabla\phi + \rho r(\phi)\lambda_\psi\nabla\psi\otimes\nabla\psi\right). \tag{3.53}$$

Plugging (3.44) into (3.25), the **momentum equation** can be rewritten as:

$$\begin{aligned}\rho\frac{D\mathbf{v}}{Dt} =& -\nabla(p-p_0)\\ &+\nabla\cdot\left(\eta[\nabla\mathbf{v}+\nabla\mathbf{v}^T] + (\kappa-\frac{2}{3}\eta)(\nabla\cdot\mathbf{v})\mathbf{I} - \rho\lambda_\phi\nabla\phi\otimes\nabla\phi - \rho r(\phi)\lambda_\psi\nabla\psi\otimes\nabla\psi\right).\end{aligned} \tag{3.54}$$

Here we have replaced ∇p with $\nabla(p-p_0)$, where the reference pressure p_0 is a constant, since $p-p_0$ always appears as a whole entity in the Gibbs free energy (3.2) and the chemical

potentials (3.50,3.52).

The **continuity equation** (3.23) can be written as

$$-\nabla\cdot\mathbf{v}=\frac{1}{\rho}\left(\frac{\partial\rho}{\partial\phi}\frac{D\phi}{Dt}+\frac{\partial\rho}{\partial\psi}\frac{D\psi}{Dt}\right) \tag{3.55}$$

since ρ is a function of (ϕ,ψ).

For energy equation, instead of using the equation (3.29) for $\hat{e}(p,T,\phi,\psi,\nabla\phi,\nabla\psi)$, we will transform it into an equation for temperature T, which is a more popular choice of primitive unknown in practice. It can be shown that

$$\begin{aligned}
\rho\frac{D\hat{e}}{Dt}=&\rho\left[\frac{\partial\hat{e}}{\partial T}\frac{DT}{Dt}+\frac{\partial\hat{e}}{\partial\phi}\frac{D\phi}{Dt}+\frac{\partial\hat{e}}{\partial\phi}\frac{D\phi}{Dt}+\frac{\partial\hat{e}}{\partial\nabla\phi}\frac{D\nabla\phi}{Dt}+\frac{\partial\hat{e}}{\partial\nabla\psi}\frac{D\nabla\psi}{Dt}\right]\\
=&\rho\frac{\partial\hat{e}}{\partial T}\frac{DT}{Dt}+\rho\frac{\partial\hat{e}}{\partial\phi}\frac{D\phi}{Dt}+\rho\frac{\partial\hat{e}}{\partial\psi}\frac{D\psi}{Dt}+\rho\frac{\partial\hat{e}}{\partial\nabla\phi}\cdot\left(\nabla\frac{D\phi}{Dt}-\nabla\mathbf{v}\cdot\nabla\phi\right)\\
&+\rho\frac{\partial\hat{e}}{\partial\nabla\psi}\cdot\left(\nabla\frac{D\psi}{Dt}-\nabla\mathbf{v}\cdot\nabla\psi\right)\\
=&\rho\frac{\partial\hat{e}}{\partial T}\frac{DT}{Dt}+\left[\frac{\partial\hat{e}}{\partial\phi}-\frac{1}{\rho}\nabla\cdot\left(\rho\frac{\partial\hat{e}}{\partial\nabla\phi}\right)\right]\rho\frac{D\phi}{Dt}+\left[\frac{\partial\hat{e}}{\partial\psi}-\frac{1}{\rho}\nabla\cdot\left(\rho\frac{\partial\hat{e}}{\partial\nabla\psi}\right)\right]\rho\frac{D\psi}{Dt}\\
&+\nabla\cdot\left(\rho\frac{\partial\hat{e}}{\partial\nabla\phi}\frac{D\phi}{Dt}+\rho\frac{\partial\hat{e}}{\partial\nabla\psi}\frac{D\psi}{Dt}\right)-\left(\rho\frac{\partial\hat{e}}{\partial\nabla\phi}\otimes\nabla\phi+\rho\frac{\partial\hat{e}}{\partial\nabla\psi}\otimes\nabla\psi\right):\nabla\mathbf{v}\\
=&\rho\frac{\partial e}{\partial T}\frac{DT}{Dt}+\left[\frac{\partial(e-g)}{\partial\phi}+\mu_\phi\right]\rho\frac{D\phi}{Dt}+\left[\frac{\partial(e-g)}{\partial\psi}+\mu_\psi\right]\rho\frac{D\psi}{Dt}\\
&+\nabla\cdot\left(\rho\frac{\partial\hat{g}}{\partial\nabla\phi}\frac{D\phi}{Dt}+\rho\frac{\partial\hat{g}}{\partial\nabla\psi}\frac{D\psi}{Dt}\right)-\left(\rho\frac{\partial\hat{g}}{\partial\nabla\phi}\otimes\nabla\phi+\rho\frac{\partial\hat{g}}{\partial\nabla\psi}\otimes\nabla\psi\right):\nabla\mathbf{v}\\
=&\rho c(\phi,\psi)\frac{DT}{dt}-M_\phi|\nabla\mu_\phi|^2-M_\psi\mu_\psi^2+\nabla\cdot\left(\rho\frac{\partial\hat{g}}{\partial\nabla\phi}\frac{D\phi}{Dt}+\rho\frac{\partial\hat{g}}{\partial\nabla\psi}\frac{D\psi}{Dt}-\mu_\phi\mathbf{j}_\phi\right)\\
&-\left(\rho\frac{\partial\hat{g}}{\partial\nabla\phi}\otimes\nabla\phi+\rho\frac{\partial\hat{g}}{\partial\nabla\psi}\otimes\nabla\psi\right):\nabla\mathbf{v}+\rho L\left[r'(\phi)r(\psi)\frac{D\phi}{Dt}+r(\phi)r'(\psi)\frac{D\psi}{Dt}\right]\frac{T}{T_M}\\
&+\rho\left[\frac{\partial c}{\partial\phi}\frac{D\phi}{Dt}+\frac{\partial c}{\partial\psi}\frac{D\psi}{Dt}\right]T\ln\frac{T}{T_M}+\frac{p}{\rho}\left(\frac{\partial\rho}{\partial\phi}\frac{D\phi}{Dt}+\frac{\partial\rho}{\partial\psi}\frac{D\psi}{Dt}\right).
\end{aligned} \tag{3.56}$$

In the first equality, we have used $\frac{\partial\hat{e}}{\partial p}=\frac{\partial e}{\partial p}=0$ which is a direct result of (3.5). In the fourth equality, we have utilized relations such as $e^*=g^*$, $\frac{\partial\hat{e}}{\partial\nabla\phi}=\frac{\partial e^*}{\partial\nabla\phi}=\frac{\partial g^*}{\partial\nabla\phi}=\frac{\partial\hat{g}}{\partial\nabla\phi}$, and Eq. (3.36). In the last equality, we have plugged in the energies (3.2,3.4) and used the phase-field

equations (3.49, 3.51).

Plugging Eqs. (3.46, 3.47, 3.56) into the energy equation (3.29), and considering the continuity equation (3.55), we arrive at the following **energy equation**in the form of temperature T:

$$\begin{aligned}\rho c\frac{DT}{Dt} =&\nabla\cdot(k\nabla T)-\rho L\left[r'(\phi)r(\psi)\frac{D\phi}{Dt}+r(\phi)r'(\psi)\frac{D\psi}{Dt}\right]\frac{T}{T_M}-\rho(\frac{\partial c}{\partial\phi}\frac{D\phi}{Dt}+\frac{\partial c}{\partial\psi}\frac{D\psi}{Dt})T\ln\frac{T}{T_M}\\&+M_\phi|\nabla\mu_\phi|^2+M_\psi\mu_\psi^2+\eta\left(\nabla\mathbf{v}+\nabla\mathbf{v}^T-\frac{2}{3}\nabla\cdot\mathbf{v}\mathbf{I}\right):\nabla\mathbf{v}+\kappa(\nabla\cdot\mathbf{v})^2.\end{aligned}\tag{3.57}$$

Equations (3.49,3.51,3.54,3.55,3.57) form the governing equations for our simulation of three-phase solidification.

3.3 Theoretical solutions of phase transition in 1D

To better understand the solidification dynamics of our quasi-incompressible system, we consider two-phase (water-ice) systems in 1D. We ignor the existence of air and set $\phi = 1$ everywhere.

3.3.1 Planar interface at equilibrium

We begin with the Allen–Cahn equation (3.51), where the chemical potential μ_ψ is given in Eq. (3.52). Diffuse interface in static equilibrium can be achieved at the melting temperature T_M and the reference pressure p_0. These conditions can be summarized as

(i) $p = p_0$ at $x = \pm\infty$,

(ii) $T = T_M$, $\frac{\partial\phi}{\partial t} = 0$, and $\mathbf{v} = 0$ for $\mathbf{x} \in \mathcal{R}$.

The conditions above yields $\rho\frac{D\psi}{Dt} = M_\psi\mu_\psi = 0$, which can be further written as

$$\begin{aligned}\mu_\psi &= \lambda_\psi W'(\psi) - \frac{p-p_0}{\rho^2}\rho'(\psi) - \frac{1}{\rho}\nabla\cdot\left(\rho\lambda_\psi\nabla\psi\right)\\ &= \lambda_\psi W'(\psi) - \frac{p-p_0}{\rho^2}\rho'(\psi) - \frac{1}{\rho}\frac{\partial}{\partial x}\left(\rho\lambda_\psi\frac{\partial\psi}{\partial x}\right) = 0.\end{aligned} \tag{3.58}$$

A typical equilibrium solution of Eq. (3.58) is a smooth transition of ψ between two stable phases. The schematic profile is shown in Fig. 3.3, where ψ varies monotonically from 0 to 1 across the diffuse interface.

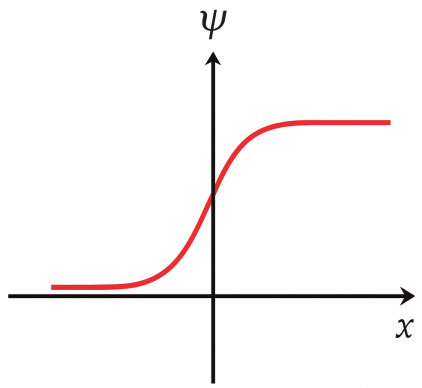

Figure 3.3: Schematic equilibrium profile of the order parameter ψ in one dimension. The interface is represented by a smooth transition from the solid to liquid phase.

Next, we turn to the momentum balance (3.54). Under the same static assumption $\mathbf{v} = 0$, the momentum equation simplifies to

$$\nabla(p-p_0) + \nabla\cdot(\rho r(\phi)\lambda_\psi\nabla\psi\otimes\nabla\psi) = \frac{\partial(p-p_0)}{\partial x} + \frac{\partial}{\partial x}\left(\rho\,\lambda_\psi\left(\frac{\partial\psi}{\partial x}\right)^2\right) = 0, \tag{3.59}$$

where we have used $r(\phi) = r(1) = 1$. Integrating (3.59) from $-\infty$ to x gives the local pressure profile

$$p(x) = p_0 - \rho\,\lambda_\psi\,(\partial_x\psi)^2, \tag{3.60}$$

where we have applied the boundary condition $p(-\infty) = p_0$. This equation shows that the

pressure is reduced within the diffuse interface by an amount proportional to the interfacial energy density $\lambda_\psi(\partial_x\psi)^2$. Typical ϕ and p profiles across the interface are illustrated in Fig. 3.4.

Plugging Eq. (3.60) into Eq. (3.58), we obtain

$$\frac{\partial^2\psi}{\partial x^2} = W'(\psi). \tag{3.61}$$

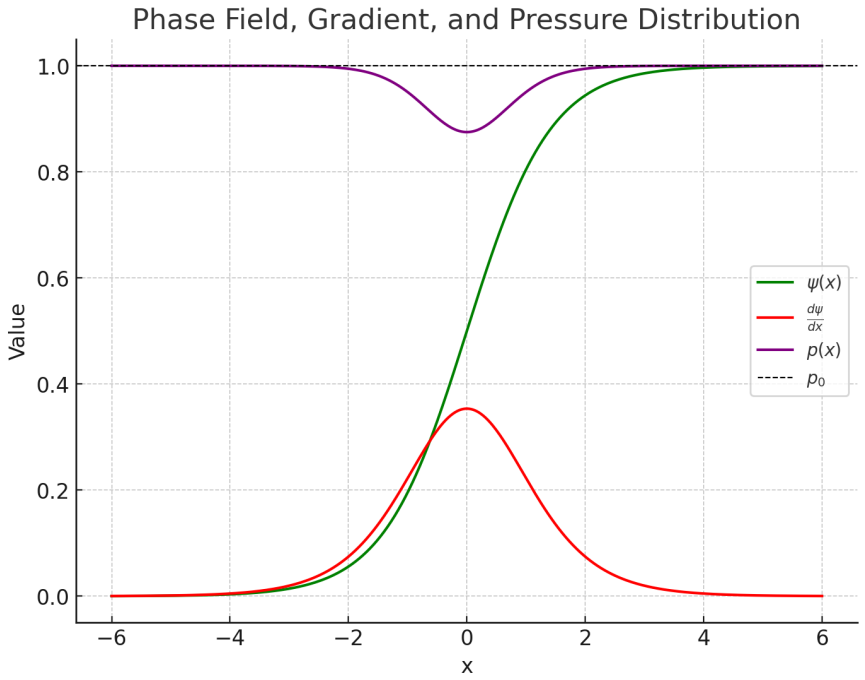

Figure 3.4: Equilibrium profiles of the order parameter $\psi(x)$, its gradient $\partial_x\psi$, and the pressure distribution $p(x)$ relative to p_0. The reduction of pressure inside the diffuse interface corresponds to the peak of the gradient.

Multiplying Eq. (3.61) by $\frac{\partial\psi}{\partial x}$ and integrating from $-\infty$ to x, with the boundary conditions $\psi(-\infty) = 0$, $\psi'(-\infty) = 0$, and $W(0) = 0$, we obtain

$$\frac{1}{2}\left(\frac{\partial\psi}{\partial x}\right)^2 = W(\psi). \tag{3.62}$$

This equation implies the equipartition between the gradient and homogeneous parts of the mixing energy f^* at equilibrium. For the chosen double-well potential $W(\psi) = \frac{\psi^2(1-\psi)^2}{\varepsilon^2}$, this

gives

$$\frac{\partial \psi}{\partial x} = \frac{\sqrt{2}}{\varepsilon}\,\psi(1-\psi). \tag{3.63}$$

Finally, integrating (3.63) once more and using the boundary conditions $\psi(-\infty) = 0$ and $\psi = \frac{1}{2}$ at $x = 0$ (s.t. the interface is centered at $x = 0$), we obtain the equilibrium profile

$$\psi(x) = \frac{1}{2}\left[1 + \tanh\left(\frac{x}{\sqrt{2}\,\varepsilon}\right)\right]. \tag{3.64}$$

Equation (3.64) shows that the phase field ψ varies smoothly across the interface, with the interface thickness proportional to ε.

Surface tension is can be obtained from the "excessive" Helmholtz free energy. At $T = T_M$ and $p = p_0$, the Helmholtz free energy (from Eqs. 3.2,3.3,3.8,3.13) reduces to

$$\hat{f} = \lambda_\psi\left[W(\psi) + \tfrac{1}{2}|\nabla\psi|^2\right] - \frac{p_0}{\rho}, \tag{3.65}$$

where $-\frac{p_0}{\rho}$ is the portion that exists everywhere and only the first term on the RHS is the excessive free energy associated with the diffuse interface. The surface tension σ can obtained by integrating the excessive free energy density across the interface:

$$\sigma = \int_{-\infty}^{\infty} \rho\,\lambda_\psi\left[W(\psi) + \tfrac{1}{2}\left(\frac{\partial\psi}{\partial x}\right)^2\right]dx = \int_{-\infty}^{\infty} \rho\,\lambda_\psi\left(\frac{\partial\psi}{\partial x}\right)^2 dx, \tag{3.66}$$

where we have used the Eq. (3.62) in the last equality. This shows that the interfacial tension is proportional to the gradient energy density accumulated across the diffuse interface.

If we define an average density

$$\bar{\rho} = \frac{\int_{-\infty}^{\infty} \rho(\psi)\left(\frac{\partial\psi}{\partial x}\right)^2 dx}{\int_{-\infty}^{\infty}\left(\frac{\partial\psi}{\partial x}\right)^2 dx}, \tag{3.67}$$

then Eq. (3.66) yields

$$\sigma = \bar{\rho}\lambda_\psi \int_{-\infty}^{\infty} \left(\frac{\partial \psi}{\partial x}\right)^2 dx = \frac{\sqrt{2}}{6}\frac{\bar{\rho}\lambda}{\epsilon}, \tag{3.68}$$

where we have plugged in the equilibrium ψ profile (3.64).

3.3.2 Phase transition dynamics in 1D

We now consider the isothermal phase transition of a planar, cylindrical, or spherical interface, as shown in Fig. 3.5. We assume the interface moves with uniform normal velocity V, such that the problem reduces to 1D due to symmetry. For convenience, we still use x to denote the radial coordinate. Similar to the planar interface, we have $\psi(0) = 0$, $\psi(\infty) = 1$, and $\psi'(0) = \psi'(\infty) = 0$. We further assume:

(i) Velocity induced by volume expansion is negligible and thus $\mathbf{v} = 0$ everywhere.

(ii) The whole system has constant temperature T, which can be different from T_M.

(iii) Density and pressure are different on the two sides of the interface: $(\rho, p) = (\rho_-, p_)$ at $x = 0$ and $(\rho_+, p+)$ at $x = \infty$.

(iv) Interface curvature radius is much greater than interfacial thickness ($R \gg \epsilon$) and thus the equilibrium ψ profile remains the same as the planar one given by (3.64). This equilibrium interface profile is maintained when the interface advances with speed V.

In 1D, we have the following relations from calculus:

$$\nabla \cdot (\rho \nabla \psi) = \frac{\partial}{\partial x}\left(\rho \frac{\partial \psi}{\partial x}\right) + \frac{d}{x}\rho\frac{\partial \psi}{\partial x}, \tag{3.69}$$

$$\nabla \cdot (\rho \nabla \psi \otimes \nabla \psi) = \left[\frac{\partial}{\partial x}\left(\rho \frac{\partial \psi}{\partial x}\frac{\partial \psi}{\partial x}\right) + \frac{d}{x}\rho\frac{\partial \psi}{\partial x}\frac{\partial \psi}{\partial x}\right]\mathbf{e}_x, \tag{3.70}$$

where $d = 0, 1, 2$ for planar, cylindrical, and spherical interfaces, respectively.

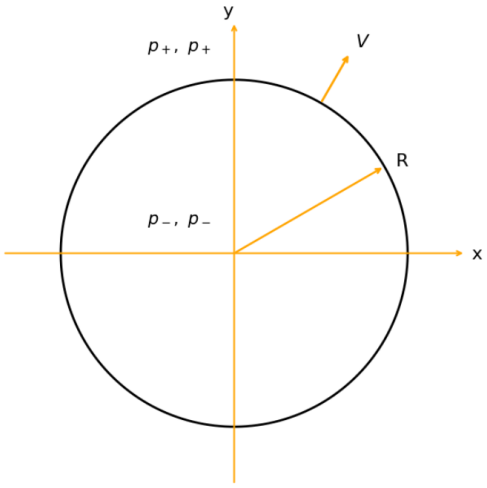

Figure 3.5: Schematic illustration of a radially symmetric interface. The interface of radius R moves outward with a constant speed V.

Assumption (iv) above leads to $\frac{\partial \psi}{\partial t} + V\frac{\partial \psi}{\partial x} = 0$. Further considering $\mathbf{v} = 0$, the Allen-Cahn equation (3.51) reduces to

$$\rho\, V\, \partial_x \psi = M_\psi \Big[r'(\psi) L \Big(1 - \tfrac{T}{T_M}\Big) - \tfrac{p - p_0}{\rho^2} \rho'(\psi) + \lambda_\psi W'(\psi) - \tfrac{1}{\rho} \nabla \cdot (\rho\, \lambda_\psi \nabla \psi) \Big]. \tag{3.71}$$

Plugging Eq. (3.69) into the equation above, we get the 1D Cahn-Hilliard equation

$$\underbrace{\rho\, V\, \partial_x \psi}_{A} = M_\psi \Big[\underbrace{r'(\psi) L \Big(1 - \tfrac{T}{T_M}\Big)}_{B} \underbrace{- \tfrac{p - p_0}{\rho^2} \rho'(\psi)}_{C} \underbrace{+ \lambda_\psi W'(\psi)}_{D} \underbrace{- \tfrac{1}{\rho}\, \partial_x (\rho\, \lambda_\psi\, \partial_x \psi)}_{E} \underbrace{- \frac{d}{x}\, \lambda_\psi\, \partial_x \psi}_{F} \Big]. \tag{3.72}$$

Under the assumption $\mathbf{v} = 0$, the momentum equation (3.54) reduces to

$$-\nabla p - \nabla \cdot (\rho\, \lambda_\psi\, \nabla \psi \otimes \nabla \psi) = 0, \tag{3.73}$$

which, with the consideration of Eq. (3.70), can be further written as

$$\frac{\partial p}{\partial x} + \frac{\partial}{\partial x} \left[\rho\, \lambda_\psi \left(\frac{\partial \psi}{\partial x} \right)^2 \right] + \frac{d}{x}\, \rho\, \lambda_\psi \left(\frac{\partial \psi}{\partial x} \right)^2 = 0. \tag{3.74}$$

Integrating Eq.(3.74) from 0 to x, and plugging in the boundary conditions $p = p_-$ and $\partial_x \psi = 0$ at $x = 0$, we obtain

$$p = p_- - \rho\,\lambda_\psi \left(\frac{\partial \psi}{\partial x}\right)^2 - \int_0^x \frac{d}{y}\,\rho(\psi(y))\,\lambda_\psi \left(\frac{\partial \psi}{\partial y}\right)^2 dy. \tag{3.75}$$

Noting $p = p_+$ and $\partial_x \psi = 0$ at $x \to \infty$, Eq. (3.75) reproduces the Young-Laplace equation for pressure jump across the interface:

$$p_- - p_+ = \int_0^\infty \frac{d}{y}\,\rho(\psi(y))\,\lambda_\psi \left(\frac{\partial \psi}{\partial y}\right)^2 dy \approx \frac{d}{R}\int_0^\infty \rho(\psi(y))\,\lambda_\psi \left(\frac{\partial \psi}{\partial y}\right)^2 dy = \frac{d}{R}\sigma, \tag{3.76}$$

where we have used Eq. (3.66) in the last equality. Since $\frac{\partial \psi}{\partial y}$ is nonzero only in the diffuse interface of width $O(\epsilon)$ and centered at radial coordinate R, it can be shown that the approximation above has an error of $O\left(\left(\frac{\epsilon}{R}\right)^2\right)$.

To proceed, we multiply the one-dimensional curved-interface Allen–Cahn equation (3.72) by $\partial_x \psi$ and integrate over the domain $x \in [0, \infty)$. This allows us to evaluate the contributions from each term in the equation systematically.

Term A of Eq. (3.51) gives

$$\int_0^\infty \rho\, V\,(\partial_x \psi)^2\, dx = \frac{V}{\lambda_\psi}\int_0^\infty \rho\,\lambda_\psi (\partial_x \psi)^2\, dx = \frac{V}{\lambda_\psi}\,\sigma. \tag{3.77}$$

Term B, the contribution from latent heat, gives

$$\int_0^\infty r'(\psi) L\left(1 - \frac{T}{T_M}\right)\partial_x \psi\, dx = \left(1 - \frac{T}{T_M}\right) L \int_0^1 r'(\psi)\, d\psi = \left(1 - \frac{T}{T_M}\right) L. \tag{3.78}$$

Term C, the coupling between pressure and density, can be written as

$$\begin{aligned}
&-\int_0^\infty \frac{p-p_0}{\rho^2}\rho'(\psi)\,\partial_x\psi\,dx \\
=&\int_0^\infty [(p_- - p_0)+(p-p_-)]\,\partial_x(\rho^{-1})\,dx = (p_- - p_0)\Big(\frac{1}{\rho_+}-\frac{1}{\rho_-}\Big)+\int_0^\infty (p-p_-)\,\partial_x(\rho^{-1})\,dx \\
=&(p_- - p_0)\left(\tfrac{1}{\rho_+}-\tfrac{1}{\rho_-}\right)+\int_0^\infty \tfrac{1}{\rho}\rho'(\psi)\lambda_\psi\left(\partial_x\psi\right)^3 dx + G,
\end{aligned} \tag{3.79}$$

where we have used Eq.(3.75) in the last equality and

$$G = -\int_0^\infty \left[\int_0^x \frac{d}{y}\rho(\psi(y))\lambda_\psi\left(\partial_y\psi\right)^2 dy\right]\partial_x(\rho(\psi(x))^{-1})dx. \tag{3.80}$$

By changing the integration order, G can be further written into

$$\begin{aligned}
G =& -\int_0^\infty \left[\int_y^\infty \partial_x(\rho(\psi(x))^{-1})dx\right]\frac{d}{y}\rho(\psi(y))\lambda_\psi\left(\psi'(y)\right)^2 dy \\
=&\int_0^\infty \left(\frac{1}{\rho(\psi(y))}-\frac{1}{\rho_+}\right)\frac{d}{y}\rho(\psi(y))\lambda_\psi\left(\psi'(y)\right)^2 dy \\
=&\int_0^\infty \frac{d}{y}\lambda_\psi\left(\psi'(y)\right)^2 dy - \frac{d}{\rho_+}\int_0^\infty \frac{\rho(\psi(y))}{y}\lambda_\psi\left(\psi'(y)\right)^2 dy \\
\approx&\int_0^\infty \frac{d}{y}\lambda_\psi\left(\psi'(y)\right)^2 dy - \frac{d\sigma}{R\rho_+},
\end{aligned} \tag{3.81}$$

where we have used the sharp-interface approximation similar to Eq. (3.76) in the last equality.

Term D vanishes since $W(0)=W(1)=0$:

$$\int_0^\infty \lambda_\psi W'(\psi)\partial_x\psi dx = \lambda_\psi\int_0^1 W'(\psi)d\psi = \lambda_\psi[W(1)-W(0)] = 0. \tag{3.82}$$

Term E leads to

$$\begin{aligned}
&-\int_0^\infty \frac{1}{\rho}\,\partial_x(\rho\,\lambda_\psi\,\partial_x\psi)\,\partial_x\psi\,dx \\
&=-\int_0^\infty \lambda_\psi\,\partial_{xx}\psi\,\partial_x\psi\,dx-\int_0^\infty \frac{1}{\rho}\rho'(\psi)\lambda_\psi\,(\partial_x\psi)^3\,dx \\
&=-\int_0^\infty \frac{1}{2}\lambda_\psi\partial_x[(\partial_x\psi)^2]dx-\int_0^\infty \frac{1}{\rho}\rho'(\psi)\lambda_\psi\,(\partial_x\psi)^3\,dx \\
&=-\int_0^\infty \frac{1}{\rho}\rho'(\psi)\lambda_\psi\,(\partial_x\psi)^3\,,
\end{aligned} \tag{3.83}$$

where we have used $\psi'(0)=\psi'(\infty)=0$ in the last equality. This term cancels out with the second term on the right hand side of Eq. (3.79).

Term F leads to

$$-\int_0^\infty \frac{d}{x}\,\lambda_\psi(\partial_x\psi)^2dx, \tag{3.84}$$

which cancels out with the first term on the right hand side of Eq. (3.81).

Combining all terms A-G above, we arrive at

$$\frac{V}{\lambda_\psi}\sigma=M_\psi\left[\left(1-\frac{T}{T_M}\right)L-\frac{d\sigma}{R\rho_+}+(p_--p_0)\left(\frac{1}{\rho_+}-\frac{1}{\rho_-}\right)\right], \tag{3.85}$$

which holds at the sharp interface limit $\frac{\epsilon}{R}\to 0$. With the help of Eq. (3.76), this equation can be further cast into the following form for the actual melting temperature T:

$$\frac{T}{T_M}-1=-\frac{V}{\frac{M_\psi\,\lambda_\psi\,L}{\sigma}}-\frac{d\,\sigma}{R\,L}\,\frac{1}{2}\left(\frac{1}{\rho_+}+\frac{1}{\rho_-}\right)+\frac{1}{L}\left(\frac{p_++p_-}{2}-p_0\right)\left(\frac{1}{\rho_+}-\frac{1}{\rho_-}\right). \tag{3.86}$$

The three terms on the right hand side account for three important effects on melting temperature: the kinetic effect associated with the moving speed of solidification front, the Gibbs-Thompson effect associated with the the surface tension and curvature, and the Clausius-Clapeyron effect associated with compressibility of the system. These three different effects will be elaborated more in later numerical experiments.

Chapter 4

Simplified 3-Phase Model

In the previous chapter, we developed a thermodynamically consistent three-phase solidification model that incorporates fluid flow, density variation, and heat transfer. To better understand the phase-field dynamics embedded in that full system, and to systematically design stable numerical schemes, we next consider a simplified three-phase model. This reduced model extracts the essential phase-evolution mechanism from the full formulation while intentionally suppressing several sources of complexity—namely the Navier–Stokes equations, the temperature equation, and the dependence of density on the phase variables. As a result, the model becomes isothermal and constant-density, enabling a cleaner analysis of the coupled Cahn–Hilliard and Allen–Cahn structures.

The simplified setting retains the two order parameters ϕ and ψ, which jointly distinguish the gas, liquid, and solid regions. Consistent with the full formulation, ϕ acts as a conserved variable governed by a Cahn–Hilliard-type equation, whereas ψ evolves according to an Allen–Cahn-type kinetics. By removing convection and thermal diffusion, the model focuses entirely on the intrinsic variational structure of the phase field system, which allows us to establish energy dissipation properties and to construct efficient SAV and IEQ time-stepping schemes. Although stripped of the hydrodynamic and thermodynamic couplings present in

the full model, the simplified system preserves the essential interfacial dynamics and serves as an effective platform for testing, analysis, and numerical verification.

4.1 Model

4.1.1 Total Free Energy

We begin by formulating the total free energy associated with the three-phase mixture. Let Ω be the spatial domain. In the present formulation, the total free energy functional $\mathcal{F}$ contains only the *non-classical part* from the diffuse interface. It is defined as:

$$\mathcal{F}[\phi, \psi] = \int_{\Omega} \tilde{f}(\phi, \psi; \nabla\phi, \nabla\psi)\, d\Omega \ , \tag{4.1}$$

where $\tilde{f}(\phi, \psi; \nabla\phi, \nabla\psi)$ is the free energy density composed of both gradient energy and bulk potential contributions:

$$\tilde{f}(\phi, \psi; \nabla\phi, \nabla\psi) = \lambda_\phi \left(W(\phi) + \frac{1}{2}|\nabla\phi|^2 \right) + r(\phi) \left[\lambda_\psi \left(W(\psi) + \frac{1}{2}|\nabla\psi|^2 \right) + r(\psi)\, L \left(1 - \frac{T}{T_m} \right) \right] . \tag{4.2}$$

Here, $W(\cdot)$ is a standard double-well potential function, whose minima correspond to the free energies of the pure phases. The gradient terms $\frac{1}{2}|\nabla\phi|^2$ and $\frac{1}{2}|\nabla\psi|^2$ penalize spatial variations, thereby contributing to interfacial energy. The constants λ_ϕ and λ_ψ scale with the interfacial energy.

The function $r(\phi)$ is a smoothly varying phase indicator (ranging between 0 and 1) that activates the second-phase free energy terms only when the material is in the solid or liquid state (i.e. when ϕ=1). Similarly, $r(\psi)$ is a phase indicator distinguishing the liquid from the solid phase. The term proportional to $L\big(1 - T/T_m\big)$ represents the bulk free-energy difference (a latent heat term) driving solidification; it is multiplied by $r(\phi)\, r(\psi)$ so that this

thermodynamic driving force is only active in the liquid phase indicated by $\phi = 1$ and $\psi = 1$. In summary, the first term in Eq. (4.2) represents the free energy contribution of the phase field ϕ (including its double-well potential and gradient energy), while the second group of terms (inside the brackets) represents the additional free energy described by ψ (including its own double-well potential and gradient term) plus the latent heat contribution when ψ changes from 0 (solid) to 1 (liquid).

To facilitate numerical implementation and reduce coupling complexity, we define a modified free energy density $f(\phi, \psi; \nabla\phi, \nabla\psi)$ by removing the phase indicator $r(\phi)$ in front of the $|\nabla\psi|^2$ term, while keeping all other components unchanged:

$$f(\phi, \psi; \nabla\phi, \nabla\psi) = \lambda_\phi \left(W(\phi) + \frac{1}{2}|\nabla\phi|^2 \right) + r(\phi) \left[\lambda_\psi W(\psi) + r(\psi)\, L \left(1 - \frac{T}{T_m} \right) \right] + \frac{1}{2}\lambda_\psi |\nabla\psi|^2 \,. \tag{4.3}$$

In this modified formulation, the gradient term $\frac{1}{2}\lambda_\psi|\nabla\psi|^2$ is treated independently of the indicator function $r(\phi)$, allowing its contribution to be present even when the system is not entirely in the condensed phase (i.e., even when $\phi \neq 1$). This simplification guarantees the linearity of the Laplacian term in the chemical potential.

4.1.2 Chemical Potentials

In this work, we use the modified free energy density $f(\phi, \psi; \nabla\phi, \nabla\psi)$ defined in Eq. (4.3), where the gradient energy term $\frac{1}{2}\lambda_\psi|\nabla\psi|^2$ is no longer multiplied by the phase indicator function $r(\phi)$. From the total free energy $\mathcal{F}$, the **chemical potentials** μ_ϕ and μ_ψ are defined as the variational (functional) derivatives of $\mathcal{F}$ with respect to the fields ϕ and ψ:

$$\mu_\phi = \frac{\delta\mathcal{F}}{\delta\phi} \,, \qquad \mu_\psi = \frac{\delta\mathcal{F}}{\delta\psi} \,. \tag{4.4}$$

Physically, these chemical potentials represent the driving forces for the evolution of the phase fields, ensuring that variations in ϕ and ψ lead to a decrease in the total free energy.

By carrying out the functional differentiation with respect to the modified free energy density f, the chemical potentials can be written in the general Euler–Lagrange form

$$\mu_\phi = \frac{\partial f}{\partial \phi} - \nabla \cdot \frac{\partial f}{\partial \nabla \phi}, \qquad \mu_\psi = \frac{\partial f}{\partial \psi} - \nabla \cdot \frac{\partial f}{\partial \nabla \psi}, \tag{4.5}$$

where the detailed derivation is provided in Appendix B.1. We obtain the full expanded forms of the chemical potentials:

$$\mu_\phi = -\lambda_\phi \Delta\phi \; + \; \lambda_\phi W'(\phi) \; + \; r'(\phi)\Big[\lambda_\psi\Big(W(\psi) + \tfrac{1}{2}|\nabla\psi|^2\Big) \; + \; r(\psi)\, L\Big(1 - \tfrac{T}{T_m}\Big)\Big] \;, \tag{4.6}$$

$$\mu_\psi = -\lambda_\psi \Delta\psi \; + \; r(\phi)\Big[\lambda_\psi W'(\psi) \; + \; r'(\psi)\, L\Big(1 - \tfrac{T}{T_m}\Big)\Big] \;, \tag{4.7}$$

where $W'(\cdot)$ and $r'(\cdot)$ denote the derivatives of W and r with respect to their arguments. These expressions explicitly show how gradients in the fields and the local free-energy landscape (through W') contribute to the chemical potentials, as well as how the coupling terms involving $r(\phi)$ and $r(\psi)$ incorporate the effect of the latent heat term in the solid phase.

4.1.3 Governing Equation

In this section, we derive the governing equations for the simplified three-phase model based on its variational structure and prove the associated energy dissipation law at the continuous PDE level. The simplified three-phase model is governed by the following coupled system of

phase-field equations:

$$\frac{\partial \phi}{\partial t} = M_\phi \, \Delta \mu_\phi, \tag{4.8}$$

$$\frac{\partial \psi}{\partial t} = - M_\psi \, \mu_\psi, \tag{4.9}$$

$$\mu_\phi = - \lambda_\phi \, \Delta \phi + \lambda_\phi \, W'(\phi) + r'(\phi) \Big[\lambda_\psi \Big(W(\psi) + \tfrac{1}{2} |\nabla \psi|^2 \Big) + r(\psi) \, L \Big(1 - \tfrac{T}{T_m} \Big) \Big], \tag{4.10}$$

$$\mu_\psi = - \lambda_\psi \, \Delta \psi + r(\phi) \Big[\lambda_\psi \, W'(\psi) + r'(\psi) \, L \Big(1 - \tfrac{T}{T_m} \Big) \Big]. \tag{4.11}$$

Here, ϕ and ψ denote the phase-field variables describing the phase configuration of the system. The quantities μ_ϕ and μ_ψ are the corresponding chemical potentials defined as the variational derivatives of the total free energy $\mathcal{F}$ with respect to ϕ and ψ. The parameters M_ϕ and M_ψ are positive mobilities that control the time scales of the phase-field evolution. The constants λ_ϕ and λ_ψ scale the interfacial energy contributions. The function $W(\cdot)$ is a double-well potential, and $r(\cdot)$ is a smooth phase indicator function. The parameter L denotes the latent heat coefficient, and T_m is the melting temperature.

4.1.4 Energy Dissipation Law

In this subsection, we derive the energy dissipation law at the PDE level for the simplified three-phase model. The governing system consists of the evolution equations (4.8)–(4.9) and the chemical potentials (4.10)–(4.11). We show that the total free energy is non-increasing in time.

We define the total free energy functional as in Eq. (4.1):

$$\mathcal{F}[\phi, \psi] = \int_\Omega f(\phi, \psi; \nabla \phi, \nabla \psi) \, d\Omega. \tag{4.12}$$

We take the time derivative of $\mathcal{F}$. Since the integrand depends on ϕ, ψ and their gradients,

we use the chain rule to obtain

$$\frac{d\mathcal{F}}{dt} = \int_\Omega \left(\frac{\partial f}{\partial \phi}\, \partial_t \phi + \frac{\partial f}{\partial \psi}\, \partial_t \psi + \frac{\partial f}{\partial \nabla \phi} \cdot \partial_t (\nabla \phi) + \frac{\partial f}{\partial \nabla \psi} \cdot \partial_t (\nabla \psi) \right) d\Omega. \tag{4.13}$$

Here, we used the fact that $f = f(\phi, \psi, \nabla\phi, \nabla\psi)$. Moreover, $\partial_t(\nabla\phi) = \nabla(\partial_t\phi)$ and $\partial_t(\nabla\psi) = \nabla(\partial_t\psi)$. We next rewrite the gradient contributions and apply integration by parts. For the ϕ term, we have

$$\int_\Omega \frac{\partial f}{\partial \nabla \phi} \cdot \nabla(\partial_t \phi)\, d\Omega = -\int_\Omega \nabla \cdot \left(\frac{\partial f}{\partial \nabla \phi} \right) \partial_t \phi\, d\Omega + \int_{\partial\Omega} \left(\frac{\partial f}{\partial \nabla \phi} \cdot \mathbf{n} \right) \partial_t \phi\, dS, \tag{4.14}$$

and similarly, for the ψ term,

$$\int_\Omega \frac{\partial f}{\partial \nabla \psi} \cdot \nabla(\partial_t \psi)\, d\Omega = -\int_\Omega \nabla \cdot \left(\frac{\partial f}{\partial \nabla \psi} \right) \partial_t \psi\, d\Omega + \int_{\partial\Omega} \left(\frac{\partial f}{\partial \nabla \psi} \cdot \mathbf{n} \right) \partial_t \psi\, dS. \tag{4.15}$$

Substituting (4.14)–(4.15) into (4.13), we obtain

$$\begin{aligned} \frac{d\mathcal{F}}{dt} = &\int_\Omega \left(\frac{\partial f}{\partial \phi} - \nabla \cdot \frac{\partial f}{\partial \nabla \phi} \right) \partial_t \phi\, d\Omega + \int_\Omega \left(\frac{\partial f}{\partial \psi} - \nabla \cdot \frac{\partial f}{\partial \nabla \psi} \right) \partial_t \psi\, d\Omega \\ &+ \int_{\partial\Omega} \left(\frac{\partial f}{\partial \nabla \phi} \cdot \mathbf{n} \right) \partial_t \phi\, dS + \int_{\partial\Omega} \left(\frac{\partial f}{\partial \nabla \psi} \cdot \mathbf{n} \right) \partial_t \psi\, dS. \end{aligned} \tag{4.16}$$

We now explain the boundary conditions used in the energy estimate. The boundary terms in (4.16) arise from integration by parts applied to the gradient contributions of the free energy. If these boundary terms do not vanish, then the time derivative $\frac{d\mathcal{F}}{dt}$ contains additional boundary contributions, and the energy dissipation property may no longer hold.

A standard and natural choice is to impose the following boundary conditions:

$$\mathbf{n} \cdot \frac{\partial f}{\partial \nabla \phi} = 0, \qquad \mathbf{n} \cdot \frac{\partial f}{\partial \nabla \psi} = 0 \quad \text{on } \partial\Omega, \tag{4.17}$$

under which all boundary integrals in (4.16) vanish. These conditions are referred to as

natural boundary conditions, since they arise directly from the variational structure of the free energy functional. The conditions (4.17) correspond to requiring that there is no flux of interfacial energy through the boundary.

Under (4.17), (4.16) reduces to

$$\frac{d\mathcal{F}}{dt} = \int_\Omega \left(\frac{\partial f}{\partial \phi} - \nabla \cdot \frac{\partial f}{\partial \nabla \phi} \right) \partial_t \phi \, d\Omega + \int_\Omega \left(\frac{\partial f}{\partial \psi} - \nabla \cdot \frac{\partial f}{\partial \nabla \psi} \right) \partial_t \psi \, d\Omega. \tag{4.18}$$

Using the definitions of the chemical potentials in Eqs. (B.1) and (B.2), we obtain

$$\frac{d\mathcal{F}}{dt} = (\mu_\phi, \partial_t \phi) + (\mu_\psi, \partial_t \psi), \tag{4.19}$$

where $(a, b) = \int_\Omega a \, b \, d\Omega$ denotes the L^2 inner product.

We now substitute the evolution equations (4.8) and (4.9). From (4.9), we have $\partial_t \psi = -M_\psi \mu_\psi$, and thus

$$(\mu_\psi, \partial_t \psi) = - M_\psi \, \|\mu_\psi\|^2_{L^2(\Omega)}.$$

From (4.8), we have $\partial_t \phi = M_\phi \Delta \mu_\phi$, and

$$(\mu_\phi, \partial_t \phi) = M_\phi \, (\mu_\phi, \Delta \mu_\phi) = - M_\phi \, \|\nabla \mu_\phi\|^2_{L^2(\Omega)},$$

where we used integration by parts and the boundary condition $\mathbf{n} \cdot \nabla \mu_\phi = 0$ on $\partial\Omega$.

Combining the above identities yields the energy dissipation law

$$\frac{d\mathcal{F}}{dt} = - M_\phi \, \|\nabla \mu_\phi\|^2_{L^2(\Omega)} - \, M_\psi \, \|\mu_\psi\|^2_{L^2(\Omega)} \, \leq \, 0. \tag{4.20}$$

Therefore, the total free energy $\mathcal{F}(t)$ is non-increasing in time.

4.1.5 Summary

In summary, the governing equations for the simplified three-phase model consist of the Cahn–Hilliard equation (4.8) for ϕ and the Allen–Cahn equation (4.9) for ψ. These equations ensure that the total free energy functional (4.1) decreases monotonically over time, as shown by the energy dissipation law (4.20).

4.2 Scalar Auxiliary Variable (SAV)

The Scalar Auxiliary Variable (SAV) approach, introduced by Shen et al. [47], is a systematic framework for constructing efficient and unconditionally energy-stable time discretization schemes for gradient flows with general nonlinear free energy potentials. Compared with earlier methods such as convex splitting [19] and stabilized semi-implicit schemes [45], the SAV approach has the key advantage of yielding linear schemes that preserve energy dissipation without restrictive timestep conditions.

The core idea of the SAV method is to introduce a scalar auxiliary variable representing the nonlinear part of the free energy, thereby reformulating the original system into an equivalent form in which the energy dissipation property can be enforced in a straightforward manner. Since its introduction, the SAV approach has been extended to a wide range of complex systems, including the Cahn–Hilliard and Allen–Cahn equations [47], hydrodynamic models of liquid crystals [67], multi-component phase-field models [60], phase-field models with nonlocal free energy terms [47], and the phase-field crystal model [38].

In this section, we derive the SAV formulation for the simplified three-phase model, following the general procedure outlined in [47]. The SAV method enables us to construct an unconditionally energy-stable numerical scheme with linear systems and high computational efficiency, making it suitable for simulating the nonlinear thermodynamic coupling in our model.

4.2.1 Nonlinear Energy Decomposition

We decompose the total free energy functional (4.1) into gradient-dependent terms and a nonlinear part:

$$\mathcal{F}[\phi,\psi] = \int_\Omega \left[\frac{\lambda_\phi}{2}|\nabla\phi|^2 + \frac{\lambda_\psi}{2}|\nabla\psi|^2\right] d\Omega + E_1(\phi,\psi), \tag{4.21}$$

where

$$E_1(\phi,\psi) = \int_\Omega \left[\lambda_\phi W(\phi) + r(\phi)\left(\lambda_\psi W(\psi) + r(\psi)L\left(1-\frac{T}{T_m}\right)\right)\right] d\Omega. \tag{4.22}$$

Here, $E_1(\phi,\psi)$ represents the nonlinear bulk energy contributions.

4.2.2 Introducing the Scalar Auxiliary Variable

Define the scalar auxiliary variable $q(t)$ by:

$$q(t) = \sqrt{E_1(\phi(t),\psi(t)) + C_0}, \tag{4.23}$$

where C_0 is a positive constant chosen to ensure $E_1 + C_0 \geq 0$ for all admissible (ϕ,ψ).

Differentiating (4.23) with respect to time yields:

$$\frac{dq}{dt} = \frac{1}{2\sqrt{E_1 + C_0}}\frac{dE_1}{dt}. \tag{4.24}$$

Using the chain rule for $E_1(\phi,\psi)$, which depends on both ϕ and ψ, we obtain

$$\frac{dE_1}{dt} = \int_\Omega \left(\frac{\partial E_1}{\partial\phi}\frac{\partial\phi}{\partial t} + \frac{\partial E_1}{\partial\psi}\frac{\partial\psi}{\partial t}\right) d\Omega. \tag{4.25}$$

Define

$$U_\phi = \frac{\partial E_1}{\partial \phi} = \lambda_\phi W'(\phi) + r'(\phi)\left[\lambda_\psi W(\psi) + r(\psi)L\left(1 - \frac{T}{T_m}\right)\right], \tag{4.26}$$

$$U_\psi = \frac{\partial E_1}{\partial \psi} = r(\phi)\left[\lambda_\psi W'(\psi) + r'(\psi)L\left(1 - \frac{T}{T_m}\right)\right], \tag{4.27}$$

where $W'(\cdot)$ and $r'(\cdot)$ denote derivatives with respect to their arguments.

Substituting (4.25) into (4.24) gives the evolution equation for q:

$$\frac{dq}{dt} = \frac{1}{2\sqrt{E_1 + C_0}} \int_\Omega \left(U_\phi \frac{\partial \phi}{\partial t} + U_\psi \frac{\partial \psi}{\partial t}\right) d\Omega. \tag{4.28}$$

4.2.3 Reformulated Chemical Potentials

In the phase-field model, the chemical potentials μ_ϕ and μ_ψ are derived from the total free energy functional $E(\phi, \psi)$, which consists of both gradient-dependent terms and nonlinear energy contributions. Reformulating these chemical potentials within the Scalar Auxiliary Variable (SAV) framework enhances numerical stability and enables a more efficient computational treatment of the phase evolution equations. Under the SAV framework, the chemical potentials are reformulated as:

$$\mu_\phi = -\lambda_\phi \Delta \phi + \frac{q}{\sqrt{E_1 + C_0}} U_\phi, \tag{4.29}$$

$$\mu_\psi = -\lambda_\psi \Delta \psi + \frac{q}{\sqrt{E_1 + C_0}} U_\psi. \tag{4.30}$$

Here, the factor $\frac{q}{\sqrt{E_1+C_0}}$ ensures that the nonlinear energy contributions are reformulated in a linearizable form while preserving energy dissipation.

4.2.4 Phase Field Evolution Equations under SAV

We now present the phase-field evolution equations under the SAV reformulation. Under this framework, the governing system consists of the evolution equations for the phase variables ϕ and ψ, together with the evolution equation for the scalar auxiliary variable q.

Substituting the reformulated chemical potentials (4.29)–(4.30) into the original governing equations (4.8) and (4.9), we obtain

$$\frac{\partial \phi}{\partial t} = M_\phi \Delta \mu_\phi = M_\phi \Delta \left(-\lambda_\phi \Delta \phi + \frac{q}{\sqrt{E_1 + C_0}} U_\phi \right), \tag{4.31}$$

$$\frac{\partial \psi}{\partial t} = -M_\psi \mu_\psi = -M_\psi \left(-\lambda_\psi \Delta \psi + \frac{q}{\sqrt{E_1 + C_0}} U_\psi \right). \tag{4.32}$$

In addition, the scalar auxiliary variable $q(t)$ evolves according to (4.28), namely,

$$\frac{dq}{dt} = \frac{1}{2\sqrt{E_1 + C_0}} \int_\Omega \left(U_\phi \frac{\partial \phi}{\partial t} + U_\psi \frac{\partial \psi}{\partial t} \right) d\Omega. \tag{4.33}$$

Equations (4.31), (4.32), and (4.33) form a closed SAV system for the variables (ϕ, ψ, q).

4.2.5 Discrete Energy Dissipation Law under SAV

We now derive a discrete energy dissipation law for the SAV formulation of the simplified three-phase model. Time is discretized using a first-order semi-implicit scheme with time step Δt and discrete time levels $t^n = n\Delta t$. Let ϕ^n, ψ^n denote the numerical solutions at time t^n, and q^n the corresponding scalar auxiliary variable.

We discretize the SAV-based phase-field evolution equations (4.31) and (4.32) as

$$\frac{\phi^{n+1}-\phi^{n}}{\Delta t} = M_\phi \, \Delta \mu_\phi^{n+1}, \tag{4.34}$$

$$\frac{\psi^{n+1}-\psi^{n}}{\Delta t} = - M_\psi \, \mu_\psi^{n+1}, \tag{4.35}$$

where the chemical potentials at the new time level are given by

$$\mu_\phi^{n+1} = - \lambda_\phi \, \Delta \phi^{n+1} + \frac{q^{n+1}}{\sqrt{E_1^n + C_0}} \, U_\phi^n, \tag{4.36}$$

$$\mu_\psi^{n+1} = - \lambda_\psi \, \Delta \psi^{n+1} + \frac{q^{n+1}}{\sqrt{E_1^n + C_0}} \, U_\psi^n. \tag{4.37}$$

Here U_ϕ^n and U_ψ^n are evaluated explicitly at time t^n.

The scalar auxiliary variable is updated according to the discrete form of (4.28):

$$\frac{q^{n+1}-q^{n}}{\Delta t} = \frac{1}{2\sqrt{E_1^n + C_0}} \int_\Omega \left(U_\phi^n \, \frac{\phi^{n+1}-\phi^{n}}{\Delta t} + U_\psi^n \, \frac{\psi^{n+1}-\psi^{n}}{\Delta t} \right) d\Omega. \tag{4.38}$$

We next take the L^2 inner product of (4.34) with μ_ϕ^{n+1} and (4.35) with μ_ψ^{n+1}. Here the inner product is defined as $(a,b) = \int_\Omega a\, b \, d\Omega$. This yields

$$\left(\mu_\phi^{n+1}, \frac{\phi^{n+1}-\phi^{n}}{\Delta t} \right) = M_\phi \, (\nabla \mu_\phi^{n+1}, \nabla \mu_\phi^{n+1}), \tag{4.39}$$

$$\left(\mu_\psi^{n+1}, \frac{\psi^{n+1}-\psi^{n}}{\Delta t} \right) = - M_\psi \, \|\mu_\psi^{n+1}\|^2_{L^2(\Omega)}, \tag{4.40}$$

where homogeneous Neumann boundary conditions are used to eliminate boundary terms.

Multiplying both equations by Δt and summing gives

$$(\mu_\phi^{n+1}, \phi^{n+1}-\phi^{n}) + (\mu_\psi^{n+1}, \psi^{n+1}-\psi^{n}) = \Delta t \, M_\phi \|\nabla \mu_\phi^{n+1}\|^2_{L^2} - \Delta t \, M_\psi \|\mu_\psi^{n+1}\|^2_{L^2}. \tag{4.41}$$

We now consider the discrete energy

$$\mathcal{F}^n = \int_\Omega \left(\frac{\lambda_\phi}{2} |\nabla \phi^n|^2 + \frac{\lambda_\psi}{2} |\nabla \psi^n|^2 \right) d\Omega + (q^n)^2 - C_0. \tag{4.42}$$

Using the definitions of μ_ϕ^{n+1}, μ_ψ^{n+1}, together with the discrete auxiliary equation (4.38), one obtains

$$(\mu_\phi^{n+1}, \phi^{n+1} - \phi^n) + (\mu_\psi^{n+1}, \psi^{n+1} - \psi^n) = \mathcal{F}^{n+1} - \mathcal{F}^n.$$

Substituting this identity into (4.41) yields the discrete energy dissipation law

$$\mathcal{F}^{n+1} - \mathcal{F}^n = -\Delta t\, M_\phi \|\nabla \mu_\phi^{n+1}\|_{L^2}^2 - \Delta t\, M_\psi \|\mu_\psi^{n+1}\|_{L^2}^2 \leq 0. \tag{4.43}$$

This demonstrates that the SAV scheme is unconditionally energy stable. The discrete free energy $\mathcal{F}^n$ is non-increasing in time, which ensures thermodynamic consistency at the fully discrete level.

4.2.6 Summary

The Scalar Auxiliary Variable (SAV) method reformulates the nonlinear free energy contributions using a scalar variable q defined in (4.23), yielding the evolution equations (4.31)–(4.32) and the auxiliary equation (4.28). This reformulation ensures an energy dissipation law at both the continuous and discrete levels, providing unconditional energy stability and linear time discretization.

However, despite its unconditional stability and simplicity, the SAV formulation introduces a scalar auxiliary variable that is coupled to all unknowns in the system, resulting in a dense row in the discretized linear system. Such a global coupling increases the computational cost and complexity for large-scale simulations. Therefore, in this work, we employ the Invariant Energy Quadratization (IEQ) method presented in the next section, which reformulates the

nonlinearities in a way that avoids introducing dense rows while retaining unconditional stability and linearity, leading to more efficient numerical implementations.

4.3 Invariant Energy Quadratization (IEQ)

The Invariant Energy Quadratization (IEQ) method is a widely used approach for constructing efficient, linear, and unconditionally energy stable schemes for gradient flow models. The IEQ approach was first introduced by Yang et al. [57], motivated by the Lagrange multiplier method proposed by Guillen-Gonzalez and Tierra [22]. It has been successfully applied to various phase-field models, including the Allen–Cahn and Cahn–Hilliard equations [57, 67].

The main advantage of the IEQ method lies in its ability to reformulate the nonlinear free energy density into a quadratic form with the introduction of auxiliary variables. This reformulation leads to linear numerical schemes that are unconditionally energy stable, even for complex nonlinearities. Compared to the convex splitting method [19] and stabilized schemes [45], the IEQ method avoids solving nonlinear systems while preserving energy stability without timestep restrictions.

Since its introduction, the IEQ approach has been widely used for solving gradient flows in phase-field models for multi-component fluids [35], hydrodynamic Q-tensor models of liquid crystals [67], binary fluid-surfactant systems [58], and molecular beam epitaxy models [59].

In this section, we derive the IEQ formulation for the simplified three-phase model introduced in Chapter 4, following the general strategy outlined in [47]. The IEQ method enables efficient time marching schemes with linear systems while guaranteeing energy dissipation at the discrete level, making it a robust choice for our coupled thermodynamic model.

4.3.1 Nonlinear Energy Reformulation

The free energy density f is given by (Eq. (4.2)):

$$f(\phi,\psi;\nabla\phi,\nabla\psi)=\lambda_\phi W(\phi)+\frac{\lambda_\phi}{2}|\nabla\phi|^2+r(\phi)\lambda_\psi W(\psi)+\frac{\lambda_\psi}{2}|\nabla\psi|^2+r(\phi)r(\psi)L\left(1-\frac{T}{T_m}\right). \tag{4.44}$$

Define the nonlinear part of f as:

$$F(\phi,\psi)=\lambda_\phi W(\phi)+r(\phi)\lambda_\psi W(\psi)+r(\phi)r(\psi)L\left(1-\frac{T}{T_m}\right). \tag{4.45}$$

Here, $F(\phi,\psi)$ collects all terms not involving gradients, while the gradient energy terms remain linear. The definitions of $W(\cdot)$, $r(\cdot)$, λ_ϕ, λ_ψ, L, T, and T_m follow Eq. (4.2).

To facilitate linearization, we introduce an auxiliary variable $q(\mathbf{x},t)$ satisfying

$$q=\sqrt{F(\phi,\psi)+C_0}, \tag{4.46}$$

where C_0 is a positive constant ensuring $F(\phi,\psi)+C_0\geq 0$ for all admissible (ϕ,ψ). Then,

$$F(\phi,\psi)=q^2-C_0. \tag{4.47}$$

This reformulation rewrites the nonlinear energy contribution in quadratic form, which is critical for constructing linear energy-stable schemes.

4.3.2 Chemical Potentials under IEQ

Under the IEQ framework, the nonlinear free energy density $F(\phi,\psi)$ is reformulated through the auxiliary variable $q=\sqrt{F(\phi,\psi)+C_0}$. Using this reformulation, the chemical potentials

associated with the phase variables ϕ and ψ can be rewritten in an equivalent form.

Recall that the total free energy functional is given by Eq. (4.1), where the gradient energy terms are quadratic and the nonlinear bulk energy contribution is represented by $F(\phi, \psi)$. Taking variational derivatives with respect to ϕ and ψ, and using the IEQ reformulation, the chemical potentials are written as

$$\mu_\phi = -\lambda_\phi \Delta\phi + \frac{q}{\sqrt{F + C_0}} \frac{\partial F}{\partial \phi}, \tag{4.48}$$

$$\mu_\psi = -\lambda_\psi \Delta\psi + \frac{q}{\sqrt{F + C_0}} \frac{\partial F}{\partial \psi}. \tag{4.49}$$

Here, the partial derivatives of the nonlinear energy $F(\phi, \psi)$ are given explicitly by

$$\frac{\partial F}{\partial \phi} = \lambda_\phi W'(\phi) + r'(\phi)\lambda_\psi W(\psi) + r'(\phi) r(\psi) L \left(1 - \frac{T}{T_m}\right), \tag{4.50}$$

$$\frac{\partial F}{\partial \psi} = r(\phi) \left[\lambda_\psi W'(\psi) + r'(\psi) L \left(1 - \frac{T}{T_m}\right)\right]. \tag{4.51}$$

At the continuous level, since $q = \sqrt{F + C_0}$ by definition, the factor $\frac{q}{\sqrt{F+C_0}}$ is identically equal to one. Therefore, the reformulated expressions (4.48)–(4.49) are mathematically equivalent to the original variational derivatives of the free energy. The introduction of this factor does not alter the continuous model. Its purpose is to facilitate the construction of linear and energy-stable schemes at the discrete level.

We note that the appearance of $\partial F/\partial \phi$ and $\partial F/\partial \psi$ follows directly from the chain rule. Indeed, taking the time derivative of $F(\phi, \psi)$ yields

$$\frac{dF}{dt} = \frac{\partial F}{\partial \phi} \frac{\partial \phi}{\partial t} + \frac{\partial F}{\partial \psi} \frac{\partial \psi}{\partial t},$$

which plays a central role in the derivation of the discrete energy dissipation law for the IEQ scheme.

4.3.3 Governing Equations under IEQ

We now present the reformulated governing equations for the simplified three-phase model under the IEQ framework. In addition to the phase variables ϕ and ψ, an auxiliary variable q is introduced to handle the nonlinear bulk free energy. As a result, the IEQ formulation leads to a coupled system consisting of the evolution equations for ϕ, ψ, and q.

Recall that the auxiliary variable is defined by Eq. (4.46), taking the time derivative and applying the chain rule yields the evolution equation for q:

$$\frac{\partial q}{\partial t} = \frac{1}{2\sqrt{F + C_0}} \left(\frac{\partial F}{\partial \phi} \frac{\partial \phi}{\partial t} + \frac{\partial F}{\partial \psi} \frac{\partial \psi}{\partial t} \right). \tag{4.52}$$

This equation couples the auxiliary variable q to the time evolution of the phase fields and ensures consistency between the reformulated energy and the original nonlinear free energy.

Using the IEQ reformulated chemical potentials (4.48) and (4.49), the phase-field evolution equations can be written as

$$\frac{\partial \phi}{\partial t} = M_\phi \Delta \mu_\phi = M_\phi \Delta \left(-\lambda_\phi \Delta \phi + \frac{q}{\sqrt{F + C_0}} \frac{\partial F}{\partial \phi} \right), \tag{4.53}$$

$$\frac{\partial \psi}{\partial t} = -M_\psi \mu_\psi = -M_\psi \left(-\lambda_\psi \Delta \psi + \frac{q}{\sqrt{F + C_0}} \frac{\partial F}{\partial \psi} \right). \tag{4.54}$$

Equations (4.53)–(4.54) together with (4.52) form a closed IEQ reformulated system at the continuous level. In the following section, we discretize this system in time and derive the corresponding discrete energy dissipation law.

4.3.4 Numerical Scheme

We now present a Crank–Nicolson type time discretization for the IEQ system. For simplicity, we assume a uniform time step size Δt and denote $t^n = n\Delta t$. Let ϕ^n, ψ^n, and q^n be

numerical approximations of ϕ, ψ, and q at time t^n, respectively.

The semi-discrete IEQ system is discretized in time as follows:

$$\frac{\phi^{n+1}-\phi^n}{\Delta t} = M_\phi \Delta \mu_\phi^{n+1/2}, \tag{4.55}$$

$$\mu_\phi^{n+1/2} = -\lambda_\phi \Delta \left(\frac{\phi^{n+1}+\phi^n}{2}\right) + \frac{q^{n+1/2}}{\sqrt{\overline{F}^{n+1/2}+C}} \frac{\partial \overline{F}^{n+1/2}}{\partial \phi}, \tag{4.56}$$

$$\frac{\psi^{n+1}-\psi^n}{\Delta t} = -M_\psi \mu_\psi^{n+1/2}, \tag{4.57}$$

$$\mu_\psi^{n+1/2} = -\lambda_\psi \Delta \left(\frac{\psi^{n+1}+\psi^n}{2}\right) + \frac{q^{n+1/2}}{\sqrt{\overline{F}^{n+1/2}+C}} \frac{\partial \overline{F}^{n+1/2}}{\partial \psi}, \tag{4.58}$$

$$\frac{q^{n+1}-q^n}{\Delta t} = \frac{1}{2\sqrt{\overline{F}^{n+1/2}+C}} \left(\frac{\partial \overline{F}^{n+1/2}}{\partial \phi} \frac{\phi^{n+1}-\phi^n}{\Delta t} + \frac{\partial \overline{F}^{n+1/2}}{\partial \psi} \frac{\psi^{n+1}-\psi^n}{\Delta t} \right). \tag{4.59}$$

Here, $\overline{F}^{n+1/2}$ denotes a second-order extrapolation of $F^{n+1/2}$ based on previous time levels. Under the assumption of a constant time step size Δt, the extrapolation is given by

$$\overline{F}^{n+1/2} = \frac{3}{2}F^n - \frac{1}{2}F^{n-1}, \tag{4.60}$$

which only involves known quantities from earlier time steps. This extrapolation provides second-order accuracy in time without introducing additional computational cost. A detailed derivation of this formula is given in Appendix B.2.

In the above scheme, all nonlinear terms associated with the free energy are treated explicitly through extrapolation, while all linear terms are treated implicitly. As a result, the scheme leads to a sequence of linear systems at each time step and is computationally efficient. Moreover, as shown in the following subsection, the resulting numerical scheme satisfies a discrete energy dissipation law.

4.3.5 Discrete Energy Dissipation and Unconditional Stability under IEQ

We derive the discrete energy dissipation law for the IEQ formulation of the simplified three-phase model. This result further implies unconditional energy stability of the proposed Crank–Nicolson IEQ scheme.

We define the discrete modified energy functional at time step n as

$$\mathcal{E}^n = \int_\Omega \left(\frac{\lambda_\phi}{2} |\nabla \phi^n|^2 + \frac{\lambda_\psi}{2} |\nabla \psi^n|^2 + (q^n)^2 - C_0 \right) d\Omega, \tag{4.61}$$

where $q^n = \sqrt{F(\phi^n, \psi^n) + C_0}$ is the auxiliary variable introduced in the IEQ reformulation.

The fully discrete IEQ system is given by the Crank–Nicolson scheme (4.55)–(4.59). Following the standard energy analysis for IEQ-type schemes, we test the discrete evolution equations with the corresponding chemical potentials and sum the resulting identities. The detailed algebraic steps are provided in Appendix B.3 and are omitted here for brevity.

As a result, we obtain the following discrete energy dissipation law:

$$\begin{aligned} &\frac{1}{\Delta t} \int_\Omega \left[(q^{n+1})^2 - (q^n)^2 \right] d\Omega + \frac{\lambda_\phi}{2\Delta t} \int_\Omega \left(|\nabla \phi^{n+1}|^2 - |\nabla \phi^n|^2 \right) d\Omega \\ &\quad + \frac{\lambda_\psi}{2\Delta t} \int_\Omega \left(|\nabla \psi^{n+1}|^2 - |\nabla \psi^n|^2 \right) d\Omega \\ &= - \int_\Omega |\nabla \mu_\phi^{n+1/2}|^2 \, d\Omega - \int_\Omega (\mu_\psi^{n+1/2})^2 \, d\Omega \ \leq \ 0, \end{aligned} \tag{4.62}$$

where $\mu_\phi^{n+1/2}$ and $\mu_\psi^{n+1/2}$ are defined in Eqs. (4.55)–(4.57).

Equation (4.62) immediately implies

$$\mathcal{E}^{n+1} \leq \mathcal{E}^n \quad \text{for any } \Delta t > 0. \tag{4.63}$$

Therefore, the proposed IEQ-based Crank–Nicolson scheme is *unconditionally energy stable*. The discrete free energy decays monotonically in time without any restriction on the time step size, which guarantees thermodynamic consistency at the fully discrete level.

Table 4.1 summarizes the key notation used throughout the variational formulation of the simplified three-phase model. This includes the definitions of phase-field variables, chemical potentials, model parameters, and mathematical symbols appearing in the governing equations, weak formulations, and numerical schemes. The table serves as a concise reference to facilitate the understanding of the model derivation, implementation, and subsequent analysis.

Table 4.1: Notation for the variational formulation of the three-phase model.

Symbol	Description
$\phi(\mathbf{x}, t)$	Conserved phase-field variable (e.g. composition or phase-fraction field); obeys Cahn–Hilliard-type dynamics.
$\psi(\mathbf{x}, t)$	Non-conserved phase-field variable (e.g. order parameter for phase state); obeys Allen–Cahn-type dynamics.
$\mu_\phi(\mathbf{x}, t)$	Chemical potential associated with ϕ (variational derivative $\delta\mathcal{F}/\delta\phi$).
$\mu_\psi(\mathbf{x}, t)$	Chemical potential associated with ψ (variational derivative $\delta\mathcal{F}/\delta\psi$).
$M_\phi,\ M_\psi$	Mobility coefficients for ϕ and ψ (positive constants governing the time scale of evolution).
$\lambda_\phi,\ \lambda_\psi$	Gradient energy (interface energy) coefficients for ϕ and ψ, respectively.
$W(u)$	Double-well potential function (bulk free energy density with two minima, typically representing two phases).
$r(u)$	Interpolation function (smooth function used to interpolate material properties or energy contributions between phases).
L	Latent heat (energy density associated with phase change, appears in free energy).
$T,\ T_m$	T is the temperature (field or parameter); T_m is a reference temperature (e.g. melting temperature).
C_0	A positive constant added to E_1 to ensure $E_1 + C_0 > 0$ (used in the SAV formulation for stability).
$F(\phi, \psi)$	Local free energy density (bulk part of the Helmholtz free energy, excluding gradient terms).
$E_1(\phi, \psi)$	Non-gradient (bulk) free energy functional, $E_1 = \int_\Omega F(\phi, \psi)\, d\Omega$.
$\mathcal{F}[\phi, \psi]$	Total free energy functional of the system (includes bulk energy E_1 and gradient energy terms).
$q(t)$	Scalar auxiliary variable (SAV) defined via $q^2 = E_1(\phi, \psi) + C_0$, introduced to linearize the scheme and preserve energy stability.
(a, b)	Notation for the L^2 inner product on Ω: $(a, b) = \int_\Omega a(\mathbf{x})\, b(\mathbf{x})\, d\Omega$.
$(\nabla a, \nabla b)$	Notation for the H^1 inner product of gradients: $(\nabla a, \nabla b) = \int_\Omega \nabla a \cdot \nabla b\, d\Omega$.
Ω	Spatial domain of the problem (with volume element $d\Omega$).
$\partial\Omega$	Boundary of the domain Ω (with outward unit normal vector $\mathbf{n}$ and surface element dS).

4.4 Numerical Result

4.4.1 Planar Interface Solidification

In this subsection, we consider a planar solid–liquid interface solidification problem to verify both the accuracy of the Allen–Cahn formulation and the energy stability of the proposed numerical scheme. This test corresponds to a one–dimensional sharp–interface limit, for which an explicit analytical expression of the front velocity is available, and therefore provides a quantitative benchmark for validation.

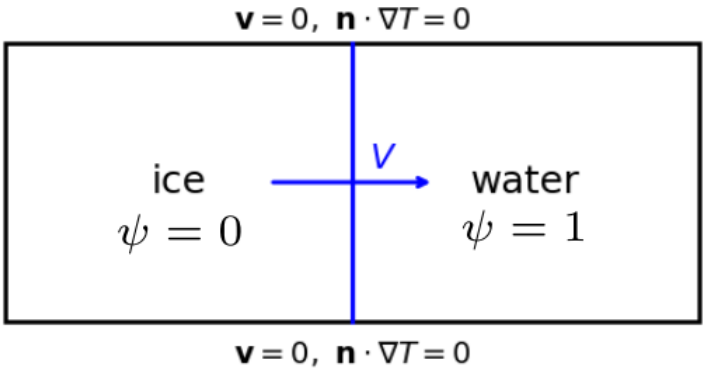

Figure 4.1: Schematic of the planar interface solidification test. The order parameter ψ distinguishes the solid phase ($\psi = 0$) from the liquid phase ($\psi = 1$). The interface propagates in the x–direction with constant velocity V under prescribed undercooling. The velocity field is set to zero and homogeneous Neumann boundary conditions are imposed for the temperature.

The computational setup corresponds to a one–dimensional planar interface embedded in a two–dimensional domain. The velocity field is identically zero, and the interface remains flat throughout the simulation, leading to steady–state interface propagation.

The following parameters are used in this test:

- mobility parameter: $M_\psi = 10, 20, 50, 100$;
- interfacial thickness: $\varepsilon = 0.2$;

- latent heat: $L = 1$;
- normalized temperature: $T/T_m = 0.9$;
- homogeneous Neumann boundary conditions for all variables.

Under these conditions, the interface propagates at a constant velocity after a short initial transient, which allows direct comparison with the sharp–interface theory.

Theoretical front velocity

The theoretical front velocity is obtained from the sharp–interface relation in Eq. (3.86). For a planar interface with equal densities in the two phases and uniform pressure, this relation reduces to

$$\frac{T}{T_m} - 1 = -\frac{V\sigma}{M_\psi \lambda_\psi L}, \tag{4.64}$$

which yields

$$V = \frac{M_\psi \lambda_\psi L}{\sigma}\left(1 - \frac{T}{T_m}\right). \tag{4.65}$$

The surface tension σ associated with the Allen–Cahn order parameter ψ is given by Eq. (3.68),

$$\sigma = \bar{\rho}\lambda_\psi \int_{-\infty}^{\infty} \left(\frac{\partial \psi}{\partial x}\right)^2 dx = \frac{\sqrt{2}}{6}\frac{\bar{\rho}\lambda_\psi}{\varepsilon}. \tag{4.66}$$

Substituting this expression and adopting the nondimensional setting $\bar{\rho} = 1$ leads to

$$V = \frac{3\sqrt{2} M_\psi L \varepsilon}{T_m}(T_m - T), \tag{4.67}$$

For the numerical experiments reported below, we fix $L = 1$, $\varepsilon = 0.2$, and $T/T_m = 0.9$. Since $T_m - T = 0.1$, the theoretical front velocity becomes

$$V = 0.042426\, M_\psi. \tag{4.68}$$

Numerical measurement of front velocity

In the numerical simulations, the interface position is identified by the level set $\psi = 0.5$. After the transient stage, the interface position varies linearly in time. The front velocity is computed by performing a linear least–squares fit of the interface position over the steady–state interval. For each value of M_ψ, two representative simulations are performed and the reported velocity is obtained by averaging the fitted values.

Table 4.2 summarizes the comparison between the theoretical prediction and the numerically measured front velocities.

Table 4.2: Comparison of theoretical and simulated front velocities for different mobility values M_ψ.

M_ψ	10	20	50	100
Theoretical V	0.042426	0.084853	0.212132	0.424264
Simulated V	0.042414	0.084822	0.212119	0.424228
Relative Error (%)	0.028	0.037	0.006	0.008

The agreement is further illustrated in Fig. 4.2, where the numerically measured front velocities are plotted against the mobility parameter.

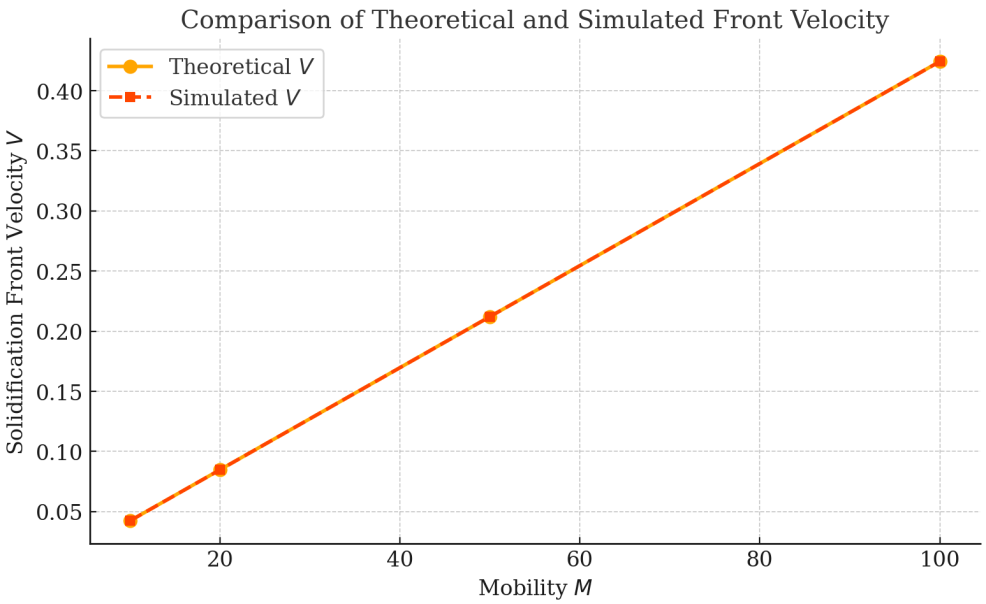

Figure 4.2: Comparison of theoretical and simulated solidification front velocity as a function of the mobility parameter M_ψ. The numerical results exhibit a linear dependence on M_ψ and agree closely with the sharp–interface prediction.

Energy decay verification

In addition to front–speed accuracy, we verify the energy stability of the numerical scheme for the planar interface case. The total free energy $\mathcal{F}(t)$ is computed at each time step using the discrete free energy functional defined in Eq. (4.1). According to the theoretical energy dissipation law (4.20), the free energy should decrease monotonically in time under homogeneous Neumann boundary conditions.

For this test, we consider the Allen–Cahn equation with mobility parameter $M_\psi = 100$. The system is initialized with a flat interface, and due to symmetry, the interface propagates at a constant speed. As shown in Fig. 4.3, the computed free energy decreases linearly over the interval $t \in [0, 0.74]$, which is in perfect agreement with the theoretical prediction for steady planar interface motion.

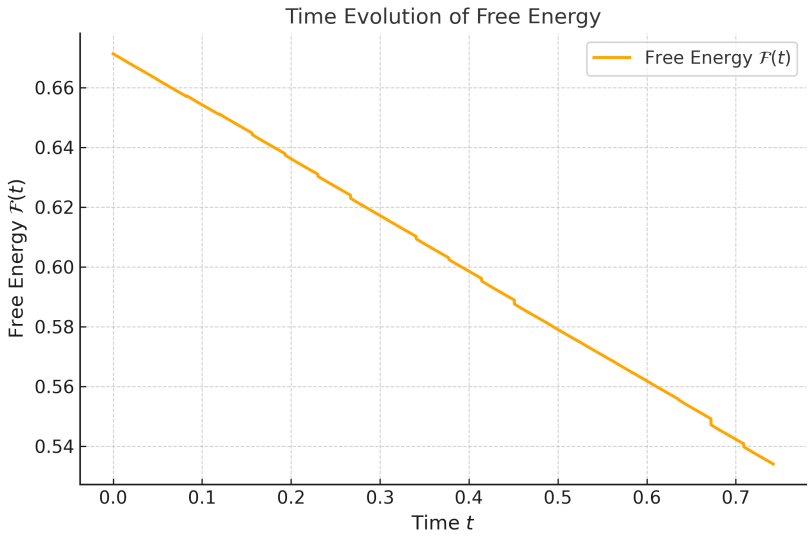

Figure 4.3: Time evolution of free energy for the Allen–Cahn equation with a planar advancing interface ($M_\psi = 100$). The free energy decreases linearly, consistent with the analytical prediction.

The planar interface solidification test demonstrates that the proposed numerical scheme accurately reproduces the analytical front–speed law in the sharp–interface limit and satisfies the discrete energy dissipation property. The linear decay of free energy and the excellent agreement between theoretical and numerical front velocities confirm both the accuracy and the thermodynamic consistency of the Allen–Cahn formulation.

4.4.2 Three-phase Freezing

In this subsection, we investigate the energy dissipation behavior of the proposed numerical scheme for a fully coupled three-phase solidification process involving solid, liquid, and gas phases. Unlike the planar interface test considered previously, this example features curved interfaces and nontrivial phase interactions.

Simulation setup and parameters

The computational domain is $\Omega = [0,1] \times [0,1]$, discretized by a uniform mesh consisting of 128×128 quadrilateral finite elements. Time integration is performed using a Crank–Nicolson scheme with a fixed time step size $\Delta t = 1.0 \times 10^{-4}$, and the simulation is advanced up to the final time $t = 1.0$, corresponding to 10^4 time steps.

The physical and numerical parameters used in this test are listed as follows:

- **Interface thickness parameters:** $\lambda_\phi = 1.0$, $\lambda_\psi = 1.0$.
- **Thermodynamic parameters:** latent heat $L = 1.0$ and $T_m = 1.0$.
- **Initial conditions:** the phase-field variables ϕ and ψ are initialized by small random perturbations around their equilibrium values in order to trigger interface formation and phase separation. Specifically,

$$\phi_0(x, y) = 0.5 + 0.01\,\mathrm{rand}(x, y),$$

  where $\mathrm{rand}(x, y)$ denotes uniformly distributed random numbers in $[-1, 1]$, and ψ is initialized in the same manner.
- **Boundary conditions:** homogeneous Neumann boundary conditions are imposed for all variables on $\partial\Omega$.

All nonlinear free energy terms are treated using the Invariant Energy Quadratization (IEQ) formulation described in Section 4.3. Compared with the Scalar Auxiliary Variable (SAV) approach [47], the IEQ method avoids global coupling through a scalar variable and leads to linear systems with sparse structure, which can be efficiently solved using standard iterative solvers.

The simulations are implemented within the `deal.II` finite element framework [5], and the

resulting linear systems are solved using a conjugate gradient method with SSOR preconditioner.

Three-phase solidification configuration

Figure 4.4 shows a schematic illustration of the three-phase solidification test. The condensed region is described by the order parameter ϕ, which separates the gas phase from the liquid–solid mixture, while the order parameter ψ distinguishes the solid and liquid phases inside the condensed region. Initially, a liquid region is surrounded by gas, with a solid nucleus present inside the liquid. As the system evolves, the solid grows at the expense of the liquid phase, and the liquid–gas interface simultaneously retreats.

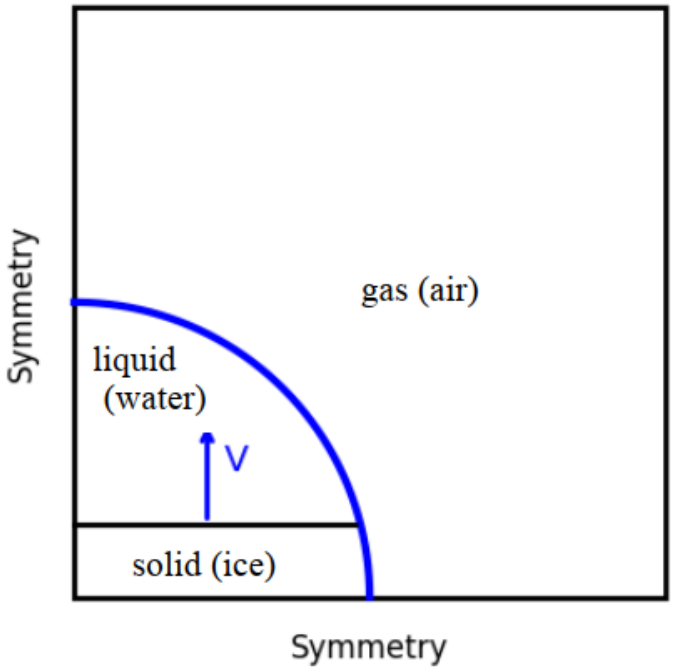

Figure 4.4: Schematic illustration of the three-phase solidification test. The order parameter ϕ separates the gas phase from the condensed phases, while ψ distinguishes solid and liquid. Curved solid–liquid and liquid–gas interfaces evolve simultaneously during the freezing process.

4.4.2.1 Energy Decay Verification

We verify the energy decay property of the proposed IEQ-based numerical scheme. The total discrete free energy is computed at each time step using the IEQ-modified energy functional defined in Eq. (4.61). The numerical scheme satisfies

$$\mathcal{E}^{n+1} \leq \mathcal{E}^{n}$$

under homogeneous Neumann boundary conditions.

We examine the energy decay behavior for a fully coupled three-phase solidification process involving solid, liquid, and gas phases. In this test, the mobilities are set to $M_\phi = 10^{-4}$ and $M_\psi = 100$, corresponding to slow gas–liquid relaxation and fast solid–liquid phase transformation.

Figure 4.5 shows the time evolution of the discrete free energy for this three-phase system. The free energy decreases strictly monotonically throughout the simulation, demonstrating that the numerical scheme preserves the discrete energy dissipation property in a complex, nonlinear setting.

Unlike the planar interface case, the energy decay is no longer linear. This nonlinear decay arises from several coupled effects: the curvature of the evolving interfaces varies in time, the liquid region progressively shrinks during freezing, and the release of latent heat is inherently nonuniform. These features lead to a time-dependent energy dissipation rate, which is accurately captured by the numerical scheme.

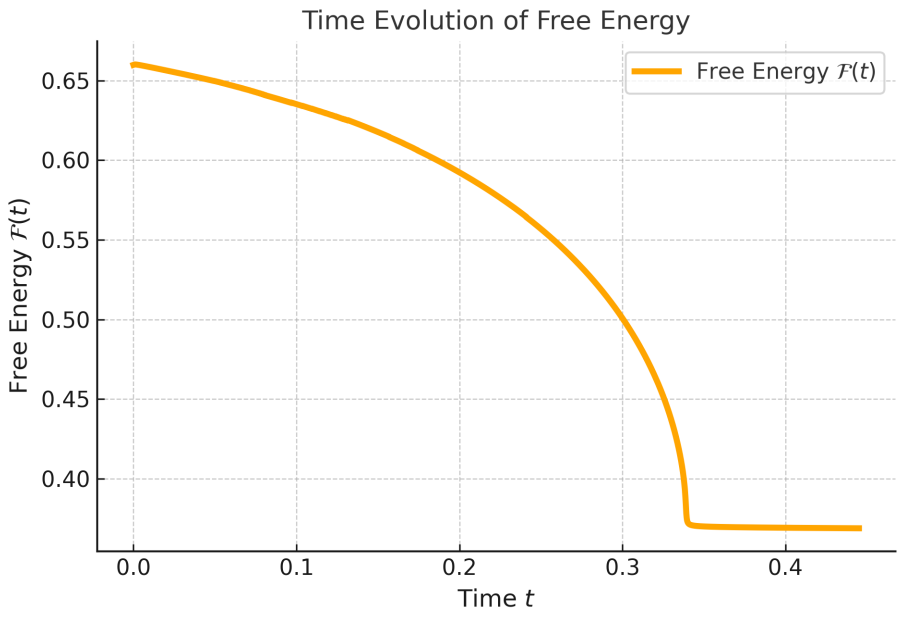

Figure 4.5: Time evolution of the discrete free energy for the three-phase freezing process with $M_\phi = 10^{-4}$ and $M_\psi = 100$. The free energy decays monotonically in time, confirming the discrete energy dissipation property of the IEQ-based numerical scheme.

Together, these two numerical experiments demonstrate that the proposed IEQ-based Crank–Nicolson scheme satisfies the discrete energy dissipation law for both simple planar interface motion and complex three-phase solidification dynamics. This confirms the thermodynamic consistency and robustness of the numerical method.

Interface evolution

To further illustrate the three–phase dynamics, Fig. 4.6 shows the contour plots of ϕ and ψ at an intermediate stage of the simulation. The contours demonstrate how the two order parameters jointly describe all three phases, with ψ capturing the solid–liquid interface and ϕ representing the liquid–gas interface.

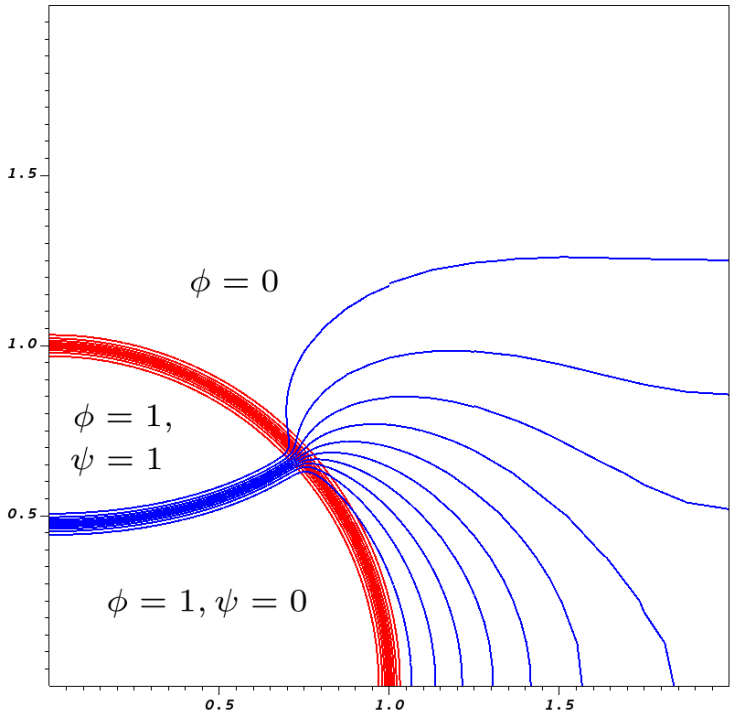

Figure 4.6: Contour plots of the phase–field variables ϕ and ψ at time $t = 0.21986$ during the three–phase freezing process. For both variables, contour levels are drawn uniformly from 0.1 to 0.9 using $N = 9$ equally spaced contours. The ψ contours (blue) represent the solid–liquid interface, while the ϕ contours (red) represent the liquid–gas interface. This visualization illustrates how the two phase–field variables jointly describe the solid, liquid, and gas phases.

For better visualization of the interface motion, Fig. 4.7 shows snapshots of the evolving interfaces at selected times. The blue curve denotes the solid–liquid interface ψ, while the red curve marks the liquid–gas interface ϕ. As solidification proceeds, the liquid region gradually shrinks and eventually disappears. The curvature–driven interface motion explains the nonlinear decay of the free energy observed in Fig. 4.5.

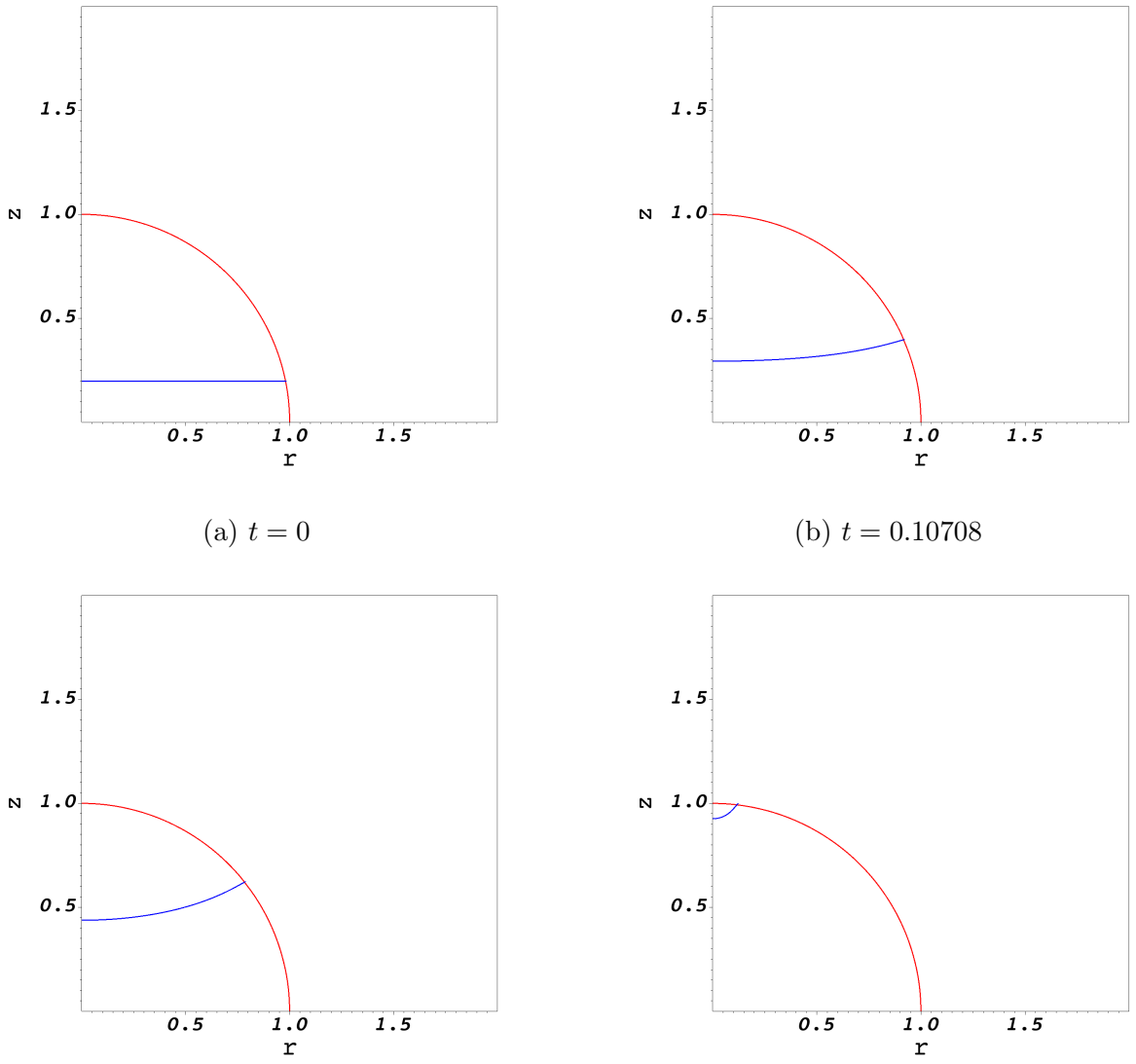

(a) $t = 0$

(b) $t = 0.10708$

(c) $t = 0.19708$

(d) $t = 0.33708$

Figure 4.7: Snapshots of interface evolution during the three–phase freezing process. The blue curve shows the solid–liquid interface ψ, and the red curve marks the liquid–gas interface ϕ. The disappearance of the liquid phase and the curved interface motion are consistent with the nonlinear energy decay.

The three–phase freezing simulation demonstrates that the proposed numerical scheme preserves the discrete energy dissipation property for complex interfacial dynamics. Unlike the planar interface case, the free energy decay is nonlinear due to curvature effects and latent heat release. Nevertheless, the free energy remains strictly decreasing in time, confirming

the thermodynamic consistency and robustness of the method for fully coupled three–phase solidification problems.

Chapter 5

Numerical discretization

5.1 Weak form of governing equation

The governing equations of our three-phase, non-isothermal solidification model consist of the Cahn–Hilliard equation for the phase-field variable ϕ, the Allen–Cahn equation for the phase-field variable ψ, the quasi-incompressible momentum equation for the velocity field $\mathbf{v}$, the associated mass continuity equation for the pressure p, and the internal energy equation for the temperature T. The governing equation have been derived and presented in Chapter 3.2.

To derive the weak formulation, each governing equation is multiplied by a suitable test function and integrated over the computational domain Ω. We denote by

$$(\cdot,\cdot)_\Omega = \int_\Omega (\cdot)(\cdot)\,\mathrm{d}\Omega$$

the $L^2(\Omega)$ inner product, and by

$$(\cdot,\cdot)_{\partial\Omega} = \int_{\partial\Omega} (\cdot)(\cdot)\,\mathrm{d}S$$

the corresponding boundary inner product.

We seek the solution fields

$$\mathbf{v} \in [H^1(\Omega)]^d, \qquad p \in L^2(\Omega), \qquad \phi,\ \psi,\ T \in H^1(\Omega),$$

where $\mathbf{v} = \mathbf{0}$ on $\partial\Omega$ enforces the no-slip boundary condition. The associated test functions

$$\tilde{\mathbf{v}},\ \tilde{p},\ \tilde{\phi},\ \tilde{\psi},\ \tilde{T}$$

are taken from the same function spaces and satisfy homogeneous boundary conditions consistent with the trial functions.

Applying integration by parts to the diffusion and stress terms and assuming homogeneous Neumann boundary conditions for ϕ, ψ, and T, together with no-slip Dirichlet boundary conditions for $\mathbf{v}$, all boundary integrals vanish naturally. The resulting weak formulation of the coupled system reads as follows.

The weak form of the momentum equation is given by

$$\begin{aligned}\big(\rho(\phi,\psi)\, D_t\mathbf{v},\ \tilde{\mathbf{v}}\big)_\Omega = \Big(&- (p - p_0)\mathbf{I} + \eta\big[\nabla\mathbf{v} + (\nabla\mathbf{v})^T - \tfrac{2}{3}(\nabla\cdot\mathbf{v})\mathbf{I}\big],\ \nabla\tilde{\mathbf{v}}\Big)_\Omega \\ &+ \Big(\rho\,\frac{\partial\hat{f}}{\partial(\nabla\phi)} \otimes \nabla\phi + \rho\,\frac{\partial\hat{f}}{\partial(\nabla\psi)} \otimes \nabla\psi,\ \nabla\tilde{\mathbf{v}}\Big)_\Omega. \end{aligned} \tag{5.1}$$

The weak form of the mass continuity equation reads

$$\big(\nabla\cdot\mathbf{v},\ \tilde{p}\big)_\Omega = -\Big(\frac{1}{\rho}\Big[\frac{\partial\rho}{\partial\phi}D_t\phi + \frac{\partial\rho}{\partial\psi}D_t\psi\Big],\ \tilde{p}\Big)_\Omega. \tag{5.2}$$

The weak form of the Cahn–Hilliard equation for ϕ is

$$\big(\rho(\phi,\psi)\, D_t\phi,\ \tilde{\phi}\big)_\Omega = -\big(M_\phi\nabla\mu_\phi,\ \nabla\tilde{\phi}\big)_\Omega. \tag{5.3}$$

The corresponding weak form defining the chemical potential μ_ϕ is

$$\begin{aligned}(\mu_\phi,\ \tilde{\mu}_\phi)_\Omega = &\Big(\big[r(\psi)r'(\phi)L - \frac{\partial c}{\partial \phi}T_M\big]\Big(1-\frac{T}{T_M}\Big),\ \tilde{\mu}_\phi\Big)_\Omega - \Big(\frac{\partial c}{\partial \phi}T\ln\frac{T}{T_M},\ \tilde{\mu}_\phi\Big)_\Omega \\ &+ \big(\lambda_\phi \omega'(\phi),\ \tilde{\mu}_\phi\big)_\Omega + \Big(r'(\phi)\lambda_\psi\Big[\omega(\psi)+\tfrac{1}{2}|\nabla\psi|^2\Big],\ \tilde{\mu}_\phi\Big)_\Omega \\ &- \Big(\frac{p-p_0}{\rho^2}\frac{\partial \rho}{\partial \phi},\ \tilde{\mu}_\phi\Big)_\Omega - \Big(\frac{1}{\rho}\nabla\cdot(\rho\lambda_\phi\nabla\phi),\ \tilde{\mu}_\phi\Big)_\Omega. \end{aligned} \tag{5.4}$$

The weak form of the Allen–Cahn equation for ψ is

$$\big(\rho\, D_t\psi,\ \tilde{\psi}\big)_\Omega = -\big(M_\psi \mu_\psi,\ \tilde{\psi}\big)_\Omega. \tag{5.5}$$

The weak form defining the chemical potential μ_ψ is

$$\begin{aligned}(\mu_\psi,\ \tilde{\mu}_\psi)_\Omega = &\Big(\big[r'(\psi)r(\phi)L - \frac{\partial c}{\partial \psi}T_M\big]\Big(1-\frac{T}{T_M}\Big),\ \tilde{\mu}_\psi\Big)_\Omega - \Big(\frac{\partial c}{\partial \psi}T\ln\frac{T}{T_M},\ \tilde{\mu}_\psi\Big)_\Omega \\ &+ \big(r(\phi)\lambda_\psi \omega'(\psi),\ \tilde{\mu}_\psi\big)_\Omega - \Big(\frac{p-p_0}{\rho^2}\frac{\partial \rho}{\partial \psi},\ \tilde{\mu}_\psi\Big)_\Omega - \Big(\frac{1}{\rho}\nabla\cdot(\rho r(\phi)\lambda_\psi\nabla\psi),\ \tilde{\mu}_\psi\Big)_\Omega. \end{aligned} \tag{5.6}$$

Finally, the weak form of the internal energy equation is

$$\begin{aligned}\big(\rho c\, D_t T,\ \tilde{T}\big)_\Omega = &\big(M_\phi|\nabla\mu_\phi|^2 + M_\psi|\mu_\psi|^2,\ \tilde{T}\big)_\Omega + \Big(\eta\big[\nabla\mathbf{v} + (\nabla\mathbf{v})^T - \tfrac{2}{3}(\nabla\cdot\mathbf{v})\mathbf{I}\big] : \nabla\mathbf{v},\ \tilde{T}\Big)_\Omega \\ &+ \big(k\nabla T,\ \nabla\tilde{T}\big)_\Omega - \Big(\rho L\big[r(\psi)r'(\phi)D_t\phi + r'(\psi)r(\phi)D_t\psi\big]\frac{T}{T_M},\ \tilde{T}\Big)_\Omega \\ &- \Big(\rho\big[\tfrac{\partial c}{\partial \phi}D_t\phi + \tfrac{\partial c}{\partial \psi}D_t\psi\big]T\ln\frac{T}{T_M},\ \tilde{T}\Big)_\Omega. \end{aligned} \tag{5.7}$$

In the above equations, $D_t(\cdot)$ denotes the material time derivative following the velocity field $\mathbf{v}$. The chemical potentials μ_ϕ and μ_ψ are defined variationally from the free-energy functional introduced in Chapter 2. The weak formulation (5.1)–(5.7) serves as the foundation for the numerical discretization described in the following sections.

5.2 Temporal Discretization

We discretize the coupled weak system (5.1)–(5.7) in time using a semi-implicit θ-scheme. Let $0 = t^0 < t^1 < \cdots < t^N$ with uniform time step size $\Delta t = t^{n+1} - t^n$. For a generic (possibly vector-valued) quantity $X(t)$, we introduce the standard convex combination at the intermediate time level $t^{n+\theta}$,

$$X^{n+\theta} := \theta X^{n+1} + (1-\theta)X^n, \qquad 0 \le \theta \le 1, \tag{5.8}$$

and approximate the material derivative by the first-order difference

$$D_t X^{n+\theta} \;\approx\; \frac{X^{n+1} - X^n}{\Delta t} + \mathbf{v}^{n+\theta} \cdot \nabla X^{n+\theta}. \tag{5.9}$$

With this convention, $\theta = 0$ recovers a fully explicit update, $\theta = \frac{1}{2}$ gives the Crank–Nicolson-type update, and $\theta = 1$ corresponds to the backward Euler. In our simulations we adopt $\theta = \frac{1}{2}$, which yields second-order accuracy for linear terms and provides a robust balance between stability and accuracy for the present nonlinear, strongly coupled system.

To make the θ-scheme treatment explicit, we illustrate the discretization on representative terms. For instance, the transient term in the Cahn–Hilliard equation (5.3),

$$\big(\rho(\phi,\psi)\, D_t\phi, \tilde{\phi}\big)_\Omega,$$

is evaluated at $t^{n+\theta}$ as

$$\Big(\rho^{n+\theta}(\phi,\psi)\, \frac{\phi^{n+1} - \phi^n}{\Delta t},\, \tilde{\phi}\Big)_\Omega, \tag{5.10}$$

while the convective contribution is treated consistently by

$$\big(\mathbf{v}\cdot\nabla\phi,\, \tilde{\phi}\big)_\Omega^{n+\theta} = \big(\mathbf{v}^{n+\theta}\cdot\nabla\phi^{n+\theta},\, \tilde{\phi}\big)_\Omega, \qquad \phi^{n+\theta} = \theta\phi^{n+1} + (1-\theta)\phi^n. \tag{5.11}$$

The same convention is applied to all advection terms appearing in (5.1)–(5.7).

Because the coefficients $\rho(\phi,\psi)$, $c(\phi,\psi)$, $\eta(\phi,\psi)$ and the chemical potentials μ_ϕ, μ_ψ are nonlinear functions of the unknown fields, the θ-scheme is implemented in a semi-implicit manner through Newton linearization within each time step. Denoting the current Newton iterate at time level t^{n+1} by $(\mathbf{v}^*, p^*, \phi^*, \psi^*, T^*)$, we write the update as

$$\mathbf{v}^{n+1} = \mathbf{v}^* + \delta\mathbf{v}, \quad p^{n+1} = p^* + \delta p, \quad \phi^{n+1} = \phi^* + \delta\phi, \quad \psi^{n+1} = \psi^* + \delta\psi, \quad T^{n+1} = T^* + \delta T,$$

and define the intermediate θ-states in the form

$$X^{*,\theta} := \theta X^* + (1-\theta)X^n, \qquad X^\theta := \theta X^{n+1} + (1-\theta)X^n = X^{*,\theta} + \theta\,\delta X, \tag{5.12}$$

for $X \in \{\mathbf{v}, p, \phi, \psi, T\}$. Equation (5.12) is precisely the practical realization of the θ-scheme, namely

$$\phi^\theta = \theta\phi^{n+1} + (1-\theta)\phi^n = \phi^{*,\theta} + \theta\,\delta\phi, \qquad \phi^{n+1} \approx \phi^* + \delta\phi.$$

Under this representation, every nonlinear contribution evaluated at $t^{n+\theta}$ can be consistently expanded to first order in the Newton increments $(\delta\mathbf{v}, \delta p, \delta\phi, \delta\psi, \delta T)$, leading to a linearized system for the increments at each Newton step.

In particular, the semi-discrete in time forms of the chemical potential relations (5.4) and (5.6) require careful θ-level linearization of the nonlinear couplings among (ϕ, ψ, T, p) and gradient terms. For completeness, we provide the detailed θ-scheme expansions and the corresponding Newton right-hand side/matrix contributions in Appendix A; see Section A.1 for μ_ϕ (starting from (5.4)) and Section A.2 for μ_ψ (starting from (5.6)). The same θ-scheme linearization strategy is also documented in Appendix A for the momentum equation (Section A.3), the continuity relation (Section A.4), and the internal energy equation (Section A.5). In the main text, we therefore only state the θ-scheme principle (5.8)–(5.12) and use it systematically when assembling the fully discrete system.

In summary, at each time step $t^n \mapsto t^{n+1}$ we evaluate all weak-form terms (5.1)–(5.7) at the intermediate level $t^{n+\theta}$, approximate material derivatives by (5.9), and linearize the resulting nonlinear residual using (5.12). This produces, at each time step, a sequence of linearized problems for the Newton increments, which are solved until convergence to obtain $(\mathbf{v}^{n+1}, p^{n+1}, \phi^{n+1}, \psi^{n+1}, T^{n+1})$.

5.3 Spatial Discretization

For the spatial discretization of the coupled weak system (5.1)–(5.7), we employ a conforming finite element method on a quadrilateral mesh of the computational domain $\Omega \subset \mathbb{R}^d$. The mesh is generated by standard `deal.II` routines and is refined either uniformly or adaptively near the diffuse interfaces, depending on the simulation setup.

Let $\mathcal{T}_h$ be a quadrilateral partition of Ω, and let $\mathbb{Q}_k(K)$ denote the tensor-product polynomials of degree $\leq k$ in each coordinate on an element $K \in \mathcal{T}_h$. In the implementation, all unknowns are discretized by continuous Lagrange elements (`FE_Q` in `deal.II`). Specifically, we choose a Taylor–Hood-type pair for the velocity–pressure variables and the same polynomial degree for the remaining scalar fields:

$$\mathbf{V}_h := \big\{ \mathbf{w}_h \in [H^1(\Omega)]^d \ : \ \mathbf{w}_h|_K \in [\mathbb{Q}_k(K)]^d \ \ \forall K \in \mathcal{T}_h \big\},$$

$$Q_h := \big\{ q_h \in L^2(\Omega) \ : \ q_h|_K \in \mathbb{Q}_{k-1}(K) \ \ \forall K \in \mathcal{T}_h \big\},$$

$$S_h := \big\{ s_h \in H^1(\Omega) \ : \ s_h|_K \in \mathbb{Q}_k(K) \ \ \forall K \in \mathcal{T}_h \big\}.$$

Here $k =$ `velocity_degree` is the polynomial degree used in the code. With this choice, $(\mathbf{V}_h, Q_h)$ corresponds to the classical Q_k/Q_{k-1} Taylor–Hood family, which satisfies the LBB (inf–sup) stability condition for incompressible flow when $k \geq 2$. In the simulations reported in this work, we set $k = 2$, i.e., the velocity is discretized by bi-quadratic ($Q2$) elements

and the pressure by bi-linear ($Q1$) elements. In contrast to the common $Q1$ choice, the scalar fields are discretized using the same degree k as the velocity in our implementation (as reflected by `FE_Q(velocity_degree)` for each scalar component).

Accordingly, we approximate

$$\mathbf{v}_h \in \mathbf{V}_h, \quad p_h \in Q_h, \quad T_h \in S_h, \quad \phi_h \in S_h, \quad \mu_{\phi,h} \in S_h, \quad \psi_h \in S_h, \quad \mu_{\psi,h} \in S_h,$$

and we choose test functions from the same spaces. The fully coupled discrete trial (and test) space is therefore

$$\mathcal{X}_h := \mathbf{V}_h \times Q_h \times S_h \times S_h \times S_h \times S_h \times S_h,$$

corresponding to the unknown vector $(\mathbf{v}_h, p_h, T_h, \phi_h, \mu_{\phi,h}, \psi_h, \mu_{\psi,h})$ assembled in the `FESystem` with component multiplicities

$$(d,\ 1,\ 1,\ 1,\ 1,\ 1,\ 1).$$

Let $(\hat{\mathbf{v}}_h, \hat{p}_h, \hat{T}_h, \hat{\phi}_h, \hat{\mu}_{\phi,h}, \hat{\psi}_h, \hat{\mu}_{\psi,h}) \in \mathcal{X}_h$ be admissible test functions. The semi-discrete (space-discrete) formulation is: find $(\mathbf{v}_h(t), p_h(t), T_h(t), \phi_h(t), \mu_{\phi,h}(t), \psi_h(t), \mu_{\psi,h}(t)) \in \mathcal{X}_h$ such that the weak equations (5.1)–(5.7) hold for all test functions in $\mathcal{X}_h$, with all integrals evaluated elementwise on $\mathcal{T}_h$ using numerical quadrature. Hanging-node constraints for adaptive refinement and essential boundary conditions are imposed through affine constraint operators, and the resulting algebraic system is assembled and solved within the `deal.II` framework.

5.4 Newton's method

After applying the temporal discretization described in Section 5.2 and the spatial discretization in Section 5.3, the coupled weak system (5.1)–(5.7) leads, at each time step $t^n \mapsto t^{n+1}$,

to a nonlinear algebraic system for the discrete unknowns

$$(\mathbf{v}^{n+1},\, p^{n+1},\, \phi^{n+1},\, \psi^{n+1},\, T^{n+1}) \in \mathbf{V}_h \times Q_h \times \Phi_h \times \Psi_h \times \Theta_h.$$

The nonlinearity arises from the advection terms, the variable material properties $\rho(\phi,\psi)$, $c(\phi,\psi)$, $\eta(\phi,\psi)$, and the nonlinear free-energy contributions in the phase-field equations.

To solve this nonlinear system, we employ a monolithic Newton iteration at each time step. Let

$$(\mathbf{v}^{*},\, p^{*},\, \phi^{*},\, \psi^{*},\, T^{*})$$

denote the current Newton iterate for the solution at time t^{n+1}, with the initial guess taken as the converged solution at the previous time level,

$$(\mathbf{v}^{*},\, p^{*},\, \phi^{*},\, \psi^{*},\, T^{*}) = (\mathbf{v}^{n},\, p^{n},\, \phi^{n},\, \psi^{n},\, T^{n}).$$

We seek an updated solution in the increment form

$$\mathbf{v}^{n+1} = \mathbf{v}^{*}+\delta\mathbf{v}, \qquad p^{n+1} = p^{*}+\delta p, \qquad \phi^{n+1} = \phi^{*}+\delta\phi, \qquad \psi^{n+1} = \psi^{*}+\delta\psi, \qquad T^{n+1} = T^{*}+\delta T. \tag{5.13}$$

Consistent with the θ-scheme introduced in (5.8)–(5.12), all quantities evaluated at the intermediate time level $t^{n+\theta}$ are expressed as

$$X^{\theta} = \theta X^{n+1} + (1-\theta)X^{n} = X^{*,\theta} + \theta\,\delta X, \qquad X \in \{\mathbf{v}, p, \phi, \psi, T\},$$

where $X^{*,\theta} = \theta X^{*} + (1-\theta)X^{n}$ is known at the current Newton step. Under this representation, every nonlinear term in (5.1)–(5.7) evaluated at $t^{n+\theta}$ can be expanded to first order with respect to the increments $(\delta\mathbf{v},\, \delta p,\, \delta\phi,\, \delta\psi,\, \delta T)$.

Substituting the increment form (5.13) into the fully discrete weak formulation and retaining

only linear terms in the increments yields a linear variational problem for $(\delta\mathbf{v},\ \delta p,\ \delta\phi,\ \delta\psi,\ \delta T)$. This linearized system couples all variables and includes the cross-derivative contributions arising from the dependence of ρ, η, and the chemical potentials μ_ϕ, μ_ψ on (ϕ, ψ, T). The detailed θ-scheme linearizations for each equation are provided in Appendix A.

At each Newton iteration, the resulting linear system is assembled and solved for the increments. The solution is then updated according to (5.13), and the process is repeated until convergence. In practice, convergence is declared when the norm of the Newton increment becomes sufficiently small, or equivalently when the residual of the discrete system is reduced below a prescribed tolerance. Due to the use of the solution at the previous time step as the initial guess and the semi-implicit treatment of the θ-scheme, only a small number of Newton iterations is required at each time step.

This fully coupled Newton linearization ensures that the strong interactions among fluid flow, phase evolution, and heat transfer are consistently resolved at the nonlinear level. Combined with the energy-consistent weak formulation and the semi-implicit time discretization, the Newton method provides a robust and efficient solver for the three-phase solidification model.

Chapter 6

Numerical results and discussions

We start this chapter by recalling the sharp–interface relation obtained in Sec. 3.3, where the moving curved interface problem was reduced to a one–dimensional problem. The key result from that section is Eq. (3.86), which relates the interfacial melting temperature to three contributions: a kinetic term, a curvature (Gibbs–Thomson) term, and a pressure (Clausius–Clapeyron) term.

In this chapter we focus on the equilibrium (static) setting relevant to freezing of water droplets, and we therefore set the interface velocity to zero, $V = 0$. With this assumption, the kinetic contribution in Eq. (3.86) drops out, and the sharp–interface relation reduces to

$$\frac{T}{T_M} - 1 = -\frac{d\,\sigma}{R\,L}\,\frac{1}{2}\left(\frac{1}{\rho_+} + \frac{1}{\rho_-}\right) + \frac{1}{L}\left(\frac{p_+ + p_-}{2} - p_0\right)\left(\frac{1}{\rho_+} - \frac{1}{\rho_-}\right), \tag{6.1}$$

where T denotes the interfacial temperature, T_M is the bulk melting temperature, σ is the interfacial surface tension, L is the latent heat, and p_0 is the reference pressure. The quantities $(\rho_\pm, p_\pm)$ represent the densities and pressures on the two sides of the interface, and the geometric parameter $d = 0, 1, 2$ together with the radius R distinguishes planar, cylindrical, and spherical settings, respectively, as discussed in Sec. 3.3.

Equation (6.1) serves as the common starting point for the validation problems in this chapter. In Sec. 6.1 (Gibbs–Thomson effect), we isolate the curvature contribution by considering cases in which the pressure term is inactive (e.g. $p_+ = p_- = p_0$), and we compare the predicted curvature–dependent shift of the melting temperature with numerical simulations. In Sec. 6.2 (Clausius–Clapeyron relation), we instead isolate the pressure contribution by considering a planar interface ($d = 0$) and varying the imposed pressure difference to quantify the resulting melting–temperature shift. For each test case, the identification of the "+" and "−" sides with the corresponding phases (solid/liquid/air) will be stated explicitly within that section, since it depends on the particular physical configuration being simulated.

6.1 Gibbs-Thomson effect

We begin by validating the Gibbs–Thomson effect, which describes how interfacial curvature and surface tension modify the melting temperature at a solid–liquid interface. Rather than postulating an explicit interfacial condition, this effect is expected to emerge naturally from the thermodynamically consistent phase-field formulation developed in the previous chapters.

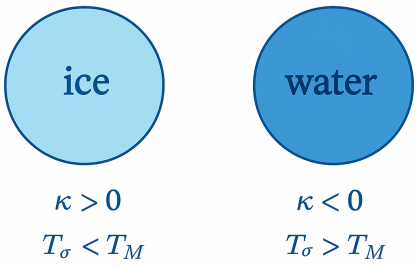

Figure 6.1: Schematic illustration of the Gibbs–Thomson effect. A curved solid–liquid interface modifies the local melting temperature T_σ relative to the planar melting temperature T_M. Positive curvature ($\kappa > 0$), corresponding to a solid particle, leads to $T_\sigma < T_M$, while negative curvature ($\kappa < 0$), corresponding to a liquid droplet, results in $T_\sigma > T_M$.

The theoretical reference for this validation is the sharp–interface equilibrium relation (6.1), obtained in Sec. 3.3. In the present test case, we consider a static equilibrium configuration ($V = 0$) and impose a uniform reference pressure $p = p_0$. Under these assumptions, the pressure contribution in (6.1) vanishes, and the remaining balance predicts a linear dependence of the melting temperature on the interfacial curvature and surface tension, corresponding to the classical Gibbs–Thomson relation.

We consider a two–dimensional square domain containing an initially circular interface of radius $R_0 = 0.5$, centered at the origin. The liquid phase occupies the region outside the circle, while the solid phase lies inside. Due to symmetry, only the first quadrant of the domain is computed. The computational configuration and mesh are illustrated in Fig. 6.2.

The phase-field variable ψ is initialized as

$$\psi = \frac{1}{2}\left[1 + \tanh\left(\frac{r - R_0}{\sqrt{2}\,\epsilon}\right)\right], \qquad r = \sqrt{x^2 + y^2}, \tag{6.2}$$

which represents a diffuse circular interface of thickness $\mathcal{O}(\epsilon)$. All other physical parameters are fixed as listed in Table 6.1, while the surface tension σ is varied.

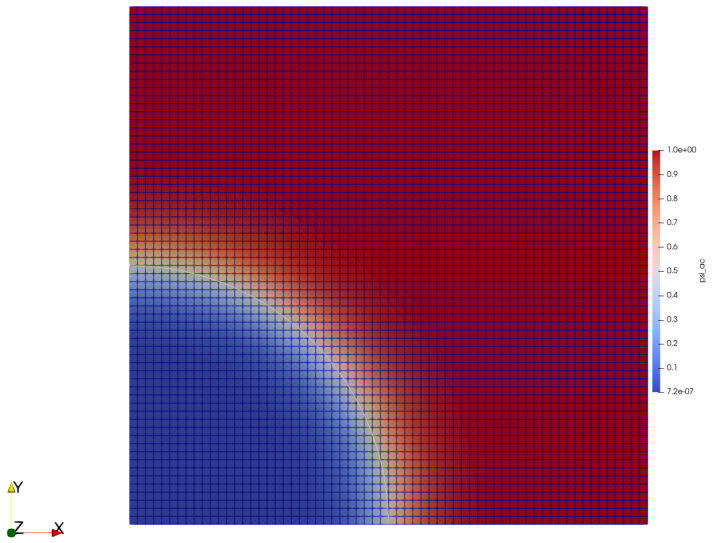

Figure 6.2: Initial circular interface and computational mesh for the Gibbs–Thomson validation test.

Parameter	Symbol	Value
Surface tension	σ	0.1,0.2,0.3,0.4
Melting temperature	T_M	1
Latent heat	L	1
Curvature	κ	2
Initial drop radius	R	0.5

Table 6.1: Parameters used for the test case.

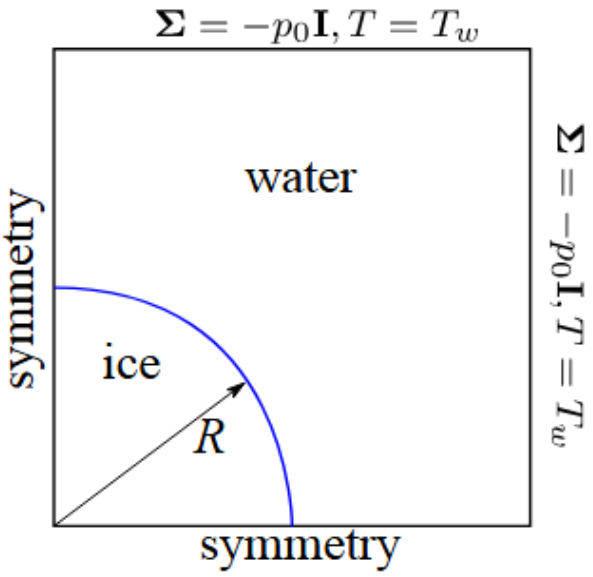

Figure 6.3: Schematic of the Gibbs–Thomson validation setup. A circular ice region is surrounded by water in a square domain. Symmetry boundary conditions are imposed along the left and bottom boundaries. The outer boundary is subject to a prescribed temperature $T = T_w$ and isotropic stress $\boldsymbol{\Sigma} = -p_0\mathbf{I}$. The interface has radius R, giving curvature $\kappa = 1/R$.

The schematic configuration used in this test is shown in Fig. 6.3. An initially circular ice region of radius $R_0 = 0.5$ is embedded in water and centered at the origin of a unit square domain. Due to symmetry, only the first quadrant is simulated. The interface curvature is therefore constant and given by $\kappa = 1/R_0$. A uniform temperature T_w is imposed on

the outer boundary, while symmetry conditions are applied on the remaining boundaries. This configuration allows us to study a static equilibrium of the curved solid–liquid interface under prescribed curvature and surface tension.

Starting from the sharp–interface equilibrium relation (6.1), we consider the case of constant pressure $p = p_0$. Under this assumption, the pressure contribution vanishes and the equilibrium condition reduces to the classical Gibbs–Thomson relation,

$$L\left(1 - \frac{T_\sigma}{T_M}\right) + \frac{\sigma\kappa}{\rho} = 0, \tag{6.3}$$

where T_σ denotes the equilibrium melting temperature of a curved interface, T_M is the melting temperature of a planar interface, σ is the surface tension, and ρ is the averaged density defined in Sec. 3.3. For a fixed curvature κ, this relation predicts a linear dependence of T_σ on σ.

For a fixed value of σ, a sequence of simulations is performed by varying the imposed initial temperature with increment $\Delta T = 0.01$. For each run, the evolution of the interface is monitored:

- if the interface shrinks monotonically, the temperature is above the equilibrium melting temperature T_σ;
- if the interface expands, the temperature is below T_σ;
- if the interface neither shrinks nor expands over time, the system is at an unstable equilibrium corresponding to $T = T_\sigma$.

This procedure yields a lower and an upper bound for T_σ, from which the numerical melting temperature is identified.

The predicted equilibrium melting temperatures obtained from the Gibbs–Thomson relation are listed in Table 6.2, while the numerical results are summarized in Table 6.3.

Surface tension σ	Predicted T_σ
0.1	0.8
0.2	0.6
0.3	0.4
0.4	0.2

Table 6.2: Theoretical melting temperatures predicted by the Gibbs–Thomson relation.

Surface tension σ	Lower bound	Numerical T_σ	Upper bound
0.1	0.79	0.80	0.81
0.2	0.59	0.60	0.61
0.3	0.39	0.40	0.41
0.4	0.19	0.20	0.21

Table 6.3: Numerically identified melting temperatures for different surface tensions.

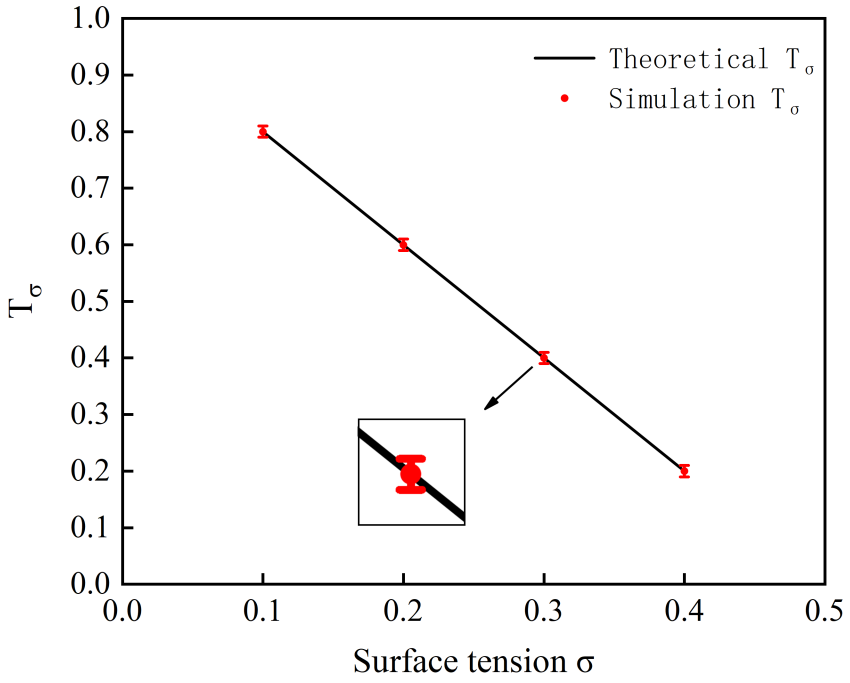

Figure 6.4: Comparison between theoretical and numerical melting temperatures as a function of surface tension.

The numerical results show excellent agreement with the theoretical prediction across all tested values of surface tension. Both the linear trend and the quantitative values of T_σ are accurately captured. This confirms that the Gibbs–Thomson effect is automatically recovered by the phase-field model through its thermodynamically consistent formulation, without imposing any explicit interfacial condition.

6.2 Clausius-Clapeyron relation

To further validate our phase-field model, we consider the Clausius–Clapeyron relation by isolating the pressure effect in the sharp–interface condition (6.1). Specifically, we set the curvature $\kappa = 0$, corresponding to a planar solid–liquid interface, so that surface tension effects are absent and only pressure-induced shifts of the melting temperature remain. Under

this assumption, equation (6.1) reduces to

$$L\left(1-\frac{T_p}{T_M}\right)+p_a\left(\frac{1}{\rho_l}-\frac{1}{\rho_s}\right)=0, \tag{6.4}$$

where T_p denotes the equilibrium melting temperature under pressure p, T_M is the melting temperature at the reference pressure p_0, and $p_a = p - p_0$ is the imposed pressure deviation.

In this validation test, we take $\rho_l = 1$ and $\rho_s = 0.9$, consistent with the density contrast used throughout this chapter. The density difference term therefore evaluates to

$$\frac{1}{\rho_l}-\frac{1}{\rho_s}=1-\frac{1}{0.9}=-0.1111.$$

With this choice, the theoretical melting temperature under pressure p_a follows directly as

$$\frac{T_p}{T_M}=1+\frac{p_a}{L}\left(\frac{1}{\rho_l}-\frac{1}{\rho_s}\right)=1-0.1111\,\frac{p_a}{L}.$$

Here the latent heat is set to $L = 1$ in the numerical simulations, which serves as a normalization choice and does not affect the validity of the Clausius–Clapeyron relation.

The computational setup used to validate this relation is illustrated in Fig. 6.5. The domain consists of ice on the left and water on the right, separated by an initially sharp, planar interface. Symmetry conditions are imposed on the top and bottom boundaries, while zero velocity is enforced on all boundaries. A constant pressure offset is applied in the water region, while the ice region is taken as the reference state.

Temperatures $T_a < T_M$ and $T_b > T_M$ are imposed on the left and right boundaries, respectively, creating an approximately linear temperature profile across the domain. For a given pressure deviation p_a, the system evolves until a steady state is reached. At equilibrium, the solid–liquid interface remains stationary, and the interface temperature is identified numerically as the temperature value at which the phase-field order parameter remains steady in

time. This numerically determined interface temperature is then compared directly with the theoretical prediction T_p.

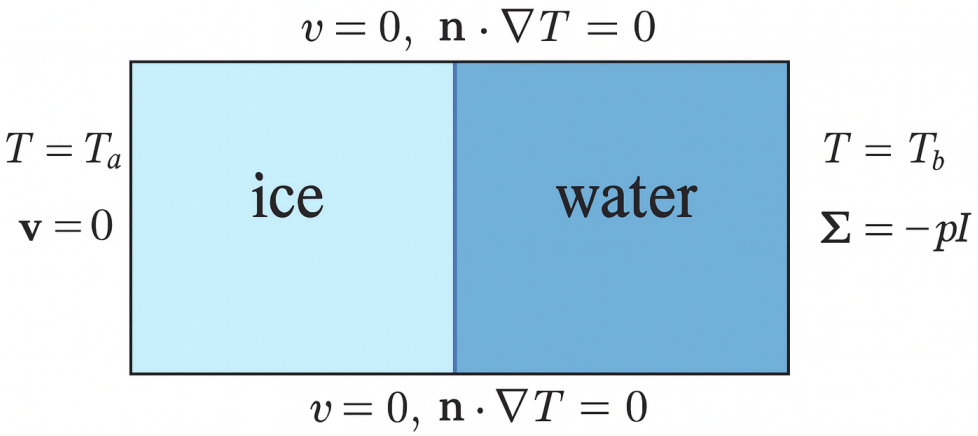

Figure 6.5: Computational setup for validating the Clausius–Clapeyron relation. Ice occupies the left region and water occupies the right region, separated by an initially planar interface. Boundary temperatures $T_a < T_M$ and $T_b > T_M$ are imposed to generate a linear temperature profile, while a pressure deviation p_a is applied in the water region.

We perform simulations for several values of the pressure deviation p_a and extract the corresponding equilibrium interface temperatures. The numerical results are summarized in Table 6.4, together with the theoretical predictions obtained from the Clausius–Clapeyron relation.

p_a	Theoretical T_p	Simulation T_p	Error (%)
-1	1.1111	1.1059	0.47
-0.5	1.0556	1.0529	0.25
-0.3	1.0333	1.0321	0.12
-0.1	1.0111	1.0109	0.02
0.1	0.9889	0.9891	0.03
0.3	0.9667	0.9680	0.13
0.5	0.9444	0.9470	0.27
1	0.8889	0.8940	0.57

Table 6.4: Comparison between theoretical and simulated melting temperatures under different pressure deviations.

Figure 6.6 presents a direct comparison between the theoretical melting temperatures predicted by the Clausius–Clapeyron relation and the numerically obtained equilibrium interface temperatures. The excellent agreement across the entire range of pressure deviations confirms that the proposed phase-field model accurately captures the pressure dependence of the melting temperature.

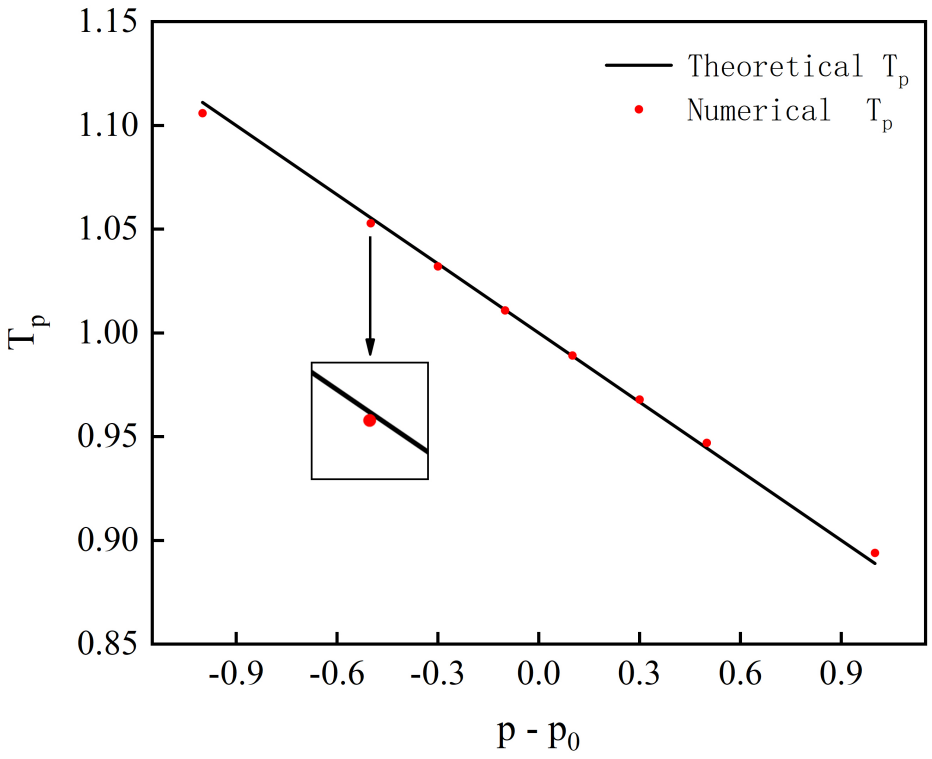

Figure 6.6: Comparison between theoretical predictions and numerical results for the melting temperature under varying pressure deviations p_a.

6.3 Volume expansion

In this section, we validate the ability of the proposed phase-field model to capture volume expansion during the phase transition from water to ice. To this end, we consider a one-dimensional three-phase Stefan problem, where ice, water, and air coexist and the solid–liquid interface advances due to freezing. The primary goal of this test is to verify whether the numerical solution satisfies the mass conservation constraint associated with density mismatch between the solid and liquid phases.

We consider a one-dimensional domain initially composed of three consecutive regions: ice on the left, water in the middle, and air on the right. As freezing proceeds, the water region

shrinks while the ice region grows, and the air region adjusts accordingly. A schematic illustration of this three-phase Stefan problem is shown in Fig. 6.7, where l_i and l_w denote the lengths of the ice and water regions, respectively.

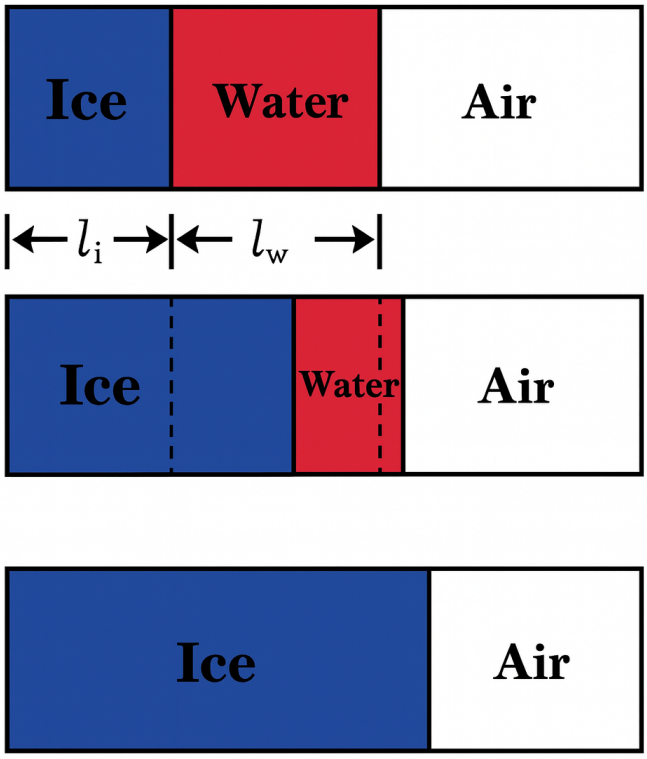

Figure 6.7: Schematic of the one-dimensional three-phase Stefan problem. The ice region grows at the expense of the water region during freezing, while the air phase occupies the remaining part of the domain.

Due to the density difference between ice and water, freezing is accompanied by volume expansion. Assuming mass conservation across the solid–liquid interface, the changes in the lengths of the ice and water regions must satisfy

$$\rho_s \Delta l_i + \rho_l \Delta l_w = 0, \tag{6.5}$$

where ρ_s and ρ_l are the densities of the solid and liquid phases, respectively, and Δl_i and Δl_w denote the increments of the ice and water regions. Equation (6.5) provides a quantitative

criterion for assessing whether the numerical solution correctly captures volume expansion.

Figure 6.8 shows the time evolution of the ice and water interfaces, as extracted from the phase-field variable. The corresponding numerical values of l_i, l_w, and the ratio $\Delta l_w/\Delta l_i$ are summarized in Table 6.5.

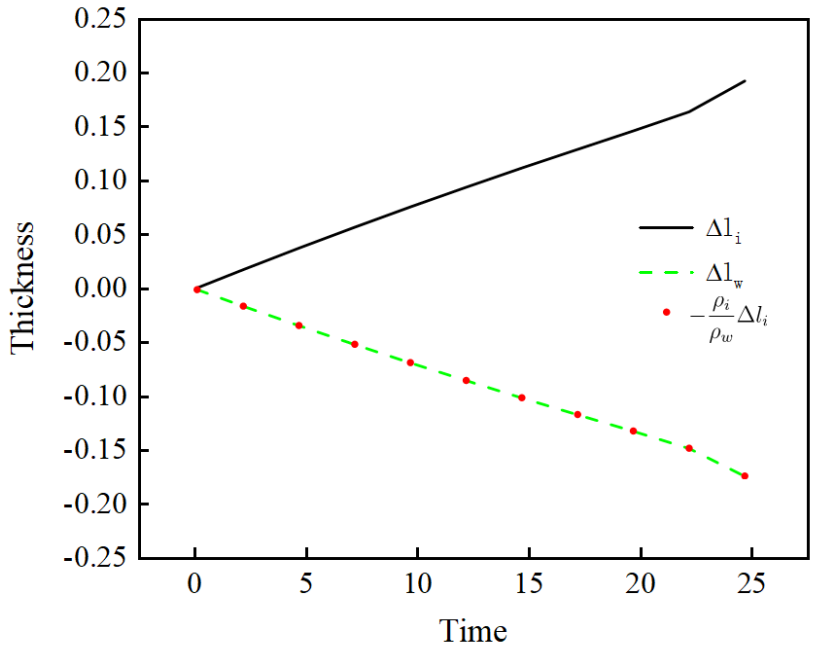

Figure 6.8: Evolution of the ice and water interface positions as functions of time. The advance of the ice region is accompanied by the retreat of the water region, reflecting volume expansion during freezing.

Time	l_i	l_w	$\frac{\Delta l_w}{\Delta l_i}$	Error %
0.0971	0.2508	0.2492	-0.9380	4.05
2.1687	0.2678	0.2339	-0.9068	0.75
4.6687	0.2877	0.2159	-0.9048	0.53
7.1687	0.3071	0.1983	-0.9040	0.44
9.6687	0.3259	0.1814	-0.9032	0.35
12.1687	0.3443	0.1649	-0.9025	0.28
14.6687	0.3620	0.1489	-0.9022	0.25
17.1687	0.3794	0.1333	-0.9020	0.23
19.6687	0.3964	0.1180	-0.9018	0.20
22.1687	0.4142	0.1020	-0.9016	0.18
24.6687	0.4427	0.0762	-0.9020	0.22

Table 6.5: Evolution of the ice and water regions and verification of mass conservation.

As shown in Table 6.5, the ratio $\Delta l_w/\Delta l_i$ remains close to the theoretical value $-\rho_s/\rho_l$ throughout the simulation. The relative error decreases over time and remains below one percent after the initial transient. These results demonstrate that the proposed phase-field model correctly captures the volume expansion induced by the density mismatch between ice and water, and satisfies the mass conservation constraint in the three-phase Stefan problem.

6.4 Freezing droplet

In this section we study the freezing of a water droplet and present numerical results obtained with the thermodynamically consistent AC/CH–NS–energy model. We first describe the physical and computational setup of the freezing droplet problem, including the computational domain, initial conditions, and boundary conditions. We then introduce the reference

physical scales and the corresponding dimensionless parameters used in the simulations. Formulating the problem in nondimensional form provides a unified framework for comparing different cases and clarifies the relative roles of surface tension, latent heat, viscosity, and heat transport.

We consider a liquid water droplet initially at a uniform temperature T_0 placed on a cold substrate and surrounded by air. The droplet occupies a two-dimensional axisymmetric domain, with gravity neglected. The computational domain is chosen sufficiently large so that the outer boundaries do not influence the droplet dynamics during the time interval of interest. Initially, the droplet has a circular shape with radius R_f, and the phase-field variables are initialized so that the water–air and water–ice interfaces are smoothly represented by diffuse transition layers. The initial temperature field is prescribed uniformly inside the droplet and air regions, while the substrate temperature is fixed below the melting temperature T_M.

No-slip velocity conditions are imposed on the solid substrate, while stress-free or symmetry conditions are applied on the remaining boundaries, consistent with the axisymmetric geometry. Thermal boundary conditions are specified by fixing the temperature at the substrate and applying either symmetry or zero-flux conditions on the remaining boundaries. Under these conditions, the droplet cools from below, and freezing proceeds through the coupled evolution of the water–ice and solid–air interfaces, driven by heat diffusion, latent heat release, and interfacial forces. This configuration serves as a representative and physically relevant test case for assessing the capability of the phase-field model to capture freezing dynamics of droplets.

To nondimensionalize the governing equations, we introduce a set of reference physical parameters based on typical material properties of water. These parameters define the characteristic scales for length, temperature, time, and material response appearing in the freezing droplet simulations, and they are used consistently to scale all terms in the AC/CH–NS–energy system.

The base reference quantities are listed in Table 6.6. The reference length R_f is chosen as the initial droplet radius, which sets the geometric scale of the problem. The liquid–air surface tension σ_f provides the capillary scale, while the reference density ρ_f is taken as that of liquid water. The specific heat c_f and thermal conductivity k_f determine the thermal response, and η_f is the reference viscosity. The temperature scale is chosen as $T_f = 1\,\mathrm{K}$, which allows temperature variations to be expressed conveniently in nondimensional form. The latent heat L_f sets the characteristic energy scale associated with phase change.

Parameter	Symbol	Value (SI units)
Reference length	R_f	$2.50 \times 10^{-4}\,\mathrm{m}$
Surface tension	σ_f	$7.20 \times 10^{-2}\,\mathrm{N/m}$
Density	ρ_f	$1.00 \times 10^{3}\,\mathrm{kg/m^3}$
Temperature scale	T_f	$1.00\,\mathrm{K}$
Specific heat	c_f	$4.18 \times 10^{3}\,\mathrm{J/(kg\,K)}$
Thermal conductivity	k_f	$5.56 \times 10^{-1}\,\mathrm{W/(m\,K)}$
Viscosity	η_f	$1.78 \times 10^{-3}\,\mathrm{Pa\,s}$
Reference velocity	V_f	$5.31 \times 10^{-2}\,\mathrm{m/s}$
Latent heat	L_f	$3.34 \times 10^{5}\,\mathrm{J/kg}$

Table 6.6: Base reference physical parameters used in the nondimensional formulation.

From these base quantities, we define the derived reference scales summarized in Table 6.7. The thermal diffusivity is $\alpha_f = k_f/(\rho_f c_f)$, and the reference velocity is defined as $V_f = \alpha_f/R_f$, corresponding to heat diffusion across the droplet radius. This choice naturally leads to the time scale $t_f = R_f/V_f$, while the reference pressure is given by $p_f = \rho_f V_f^2$. These scales are used to nondimensionalize the momentum and energy equations and to fix the scaling of mobilities, mixing energy coefficients, and relaxation rates in the phase-field formulation.

Derived quantity	Symbol	Value (SI units)
Reference time	t_f	$4.71 \times 10^{-1}\,\mathrm{s}$
Reference pressure	p_f	$2.83 \times 10^{-4}\,\mathrm{Pa}$
Thermal diffusivity	α_f	$1.23 \times 10^{-7}\,\mathrm{m^2/s}$
Mixing energy	λ_f	$1.80 \times 10^{-8}\,\mathrm{m^2/s^2}$
AC mobility	$M_{\psi,f}$	$7.38 \times 10^{-2}\,\mathrm{kg\,s/m^3}$
CH mobility	$M_{\phi,f}$	$4.61 \times 10^{-4}\,\mathrm{kg\,s/m^5}$
Relaxation rate	$\Gamma_{\phi,f}$	$2.95 \times 10^{4}\,\mathrm{s/m^2}$

Table 6.7: Derived reference quantities computed from the base parameters.

With these reference scales fixed, all physical fields in the AC/CH–NS–energy equations are expressed in dimensionless form. The freezing droplet dynamics are then governed by a small number of dimensionless groups, including the Thompson–Gibbs parameter G characterizing curvature effects, the Stefan number Ste measuring the ratio of sensible to latent heat, the Reynolds and Weber numbers quantifying inertial effects relative to viscosity and surface tension, and the Peclet number Pe describing the balance between thermal advection and diffusion. Additional phase-field parameters Π_η and Π_T control the coupling between temperature, viscosity, and interfacial motion.

All simulations presented in the remainder of this section use the parameter values summarized in Table 6.6 and Table 6.7, unless stated otherwise. With the computational setup and nondimensional framework established, we now proceed to examine the numerical results for a reference freezing droplet case.

6.4.1 Dimensionless groups and parameter values

With the reference scales introduced above, the governing AC/CH–NS–energy system can be written in fully nondimensional form. The behavior of the freezing droplet is then characterized by a small number of dimensionless groups, each measuring the relative importance of competing physical mechanisms. This nondimensional formulation provides a concise way to interpret the numerical results and to compare different simulation cases within a unified framework.

The curvature effect associated with interfacial free energy is quantified by the Thompson–Gibbs parameter

$$G = \frac{\rho_f L_f R_f}{\sigma_f}, \tag{6.6}$$

which compares the latent heat scale to the surface tension scale. The relative importance of sensible heat compared with latent heat is measured by the Stefan number

$$Ste = \frac{C_f T_f}{L_f}. \tag{6.7}$$

Fluid inertia relative to surface tension and viscosity is characterized by the Weber and Reynolds numbers,

$$We = \frac{\rho_f V_f^2 R_f}{\sigma_f}, \tag{6.8}$$

$$Re = \frac{\rho_f V_f R_f}{\eta_f}, \tag{6.9}$$

respectively. Thermal transport is governed by the Peclet number,

$$\frac{1}{Pe} = \frac{\alpha_f}{R_f V_f} = \frac{k_f}{\rho_f c_f R_f V_f}, \tag{6.10}$$

which compares thermal diffusion to advection.

In addition, two dimensionless parameters arise naturally from the phase-field formulation.

The first,

$$\frac{1}{\Pi_\eta} = \frac{\eta_f V_f}{\rho_f c_f T_f R_f}, \tag{6.11}$$

controls the coupling between viscosity and temperature variations. The second,

$$\Pi_T = G \cdot Ste = \frac{\rho_f C_f T_f R_f}{\sigma_f}, \tag{6.12}$$

measures the combined effect of surface tension and thermal energy in the AC/CH equations.

Once the reference physical parameters are fixed, the numerical values of these dimensionless groups are uniquely determined. Table 6.8 summarizes the values used throughout the freezing droplet simulations presented in this chapter. These parameters indicate that surface tension plays a significant role ($G \approx 10^3$), latent heat dominates over sensible heat ($Ste \approx 12.5$), and viscosity exhibits a strong temperature dependence ($\Pi_\eta \approx 10^6$). The Peclet number is close to unity, implying that thermal diffusion and advection are of comparable magnitude, while the Weber and Reynolds numbers show that inertial effects are present but moderated by viscosity and surface tension.

Dimensionless group	Symbol	Value
Thompson–Gibbs parameter	G	1159.72
Product group in AC/CH equations	Π_T	14527.8
Dimensionless viscosity parameter	Π_η	1.0901×10^6
Stefan number	Ste	12.5269
Weber number	We	1
Reynolds number	Re	75.0358
Peclet number	Pe	1.01006

Table 6.8: Dimensionless groups used in the freezing droplet simulations.

Together, these dimensionless groups provide a compact description of the physical regime

studied in the freezing droplet problem. They guide the interpretation of the numerical results in the following sections, including the formation of the pointed tip, the motion of the water–ice interface, and the sensitivity of the droplet shape to surface tension. Unless otherwise stated, all simulations reported below use the parameter values listed in Table 6.8.

6.4.2 Numerical results for a base freezing droplet case

We now present a representative freezing droplet simulation to illustrate how the proposed thermodynamically consistent AC/CH–NS–energy model captures the coupled evolution of phase interfaces, temperature field, and droplet morphology. This base case serves both as a physical validation and as a reference configuration for subsequent parametric studies.

We consider a liquid water droplet initially at a uniform temperature $T_0 = 293\,\mathrm{K}$ placed on a cold substrate, surrounded by air. The melting temperature is $T_M = 273\,\mathrm{K}$. As the system evolves, heat is extracted through the substrate, triggering solidification at the water–ice interface and inducing simultaneous motion of the water–ice and solid–air interfaces. The evolution is governed by the balance between heat diffusion, latent heat release, interfacial curvature effects, and material property contrasts.

Figure 6.9 shows the time evolution of the phase interfaces for the reference case with solid–liquid interfacial tension $\sigma_{sl} = 0.8$. The red curve denotes the solid–air interface, while the blue curve represents the water–ice interface. At early times, solidification initiates near the substrate and the water–ice interface moves inward. As freezing progresses, the solid–air interface advances outward, and the coupled motion of the two interfaces leads to the formation of a pointed tip near the top of the droplet. This characteristic morphology is a direct consequence of the interaction between curvature, surface tension, and volume expansion during phase change, and is consistently reproduced by the present model.

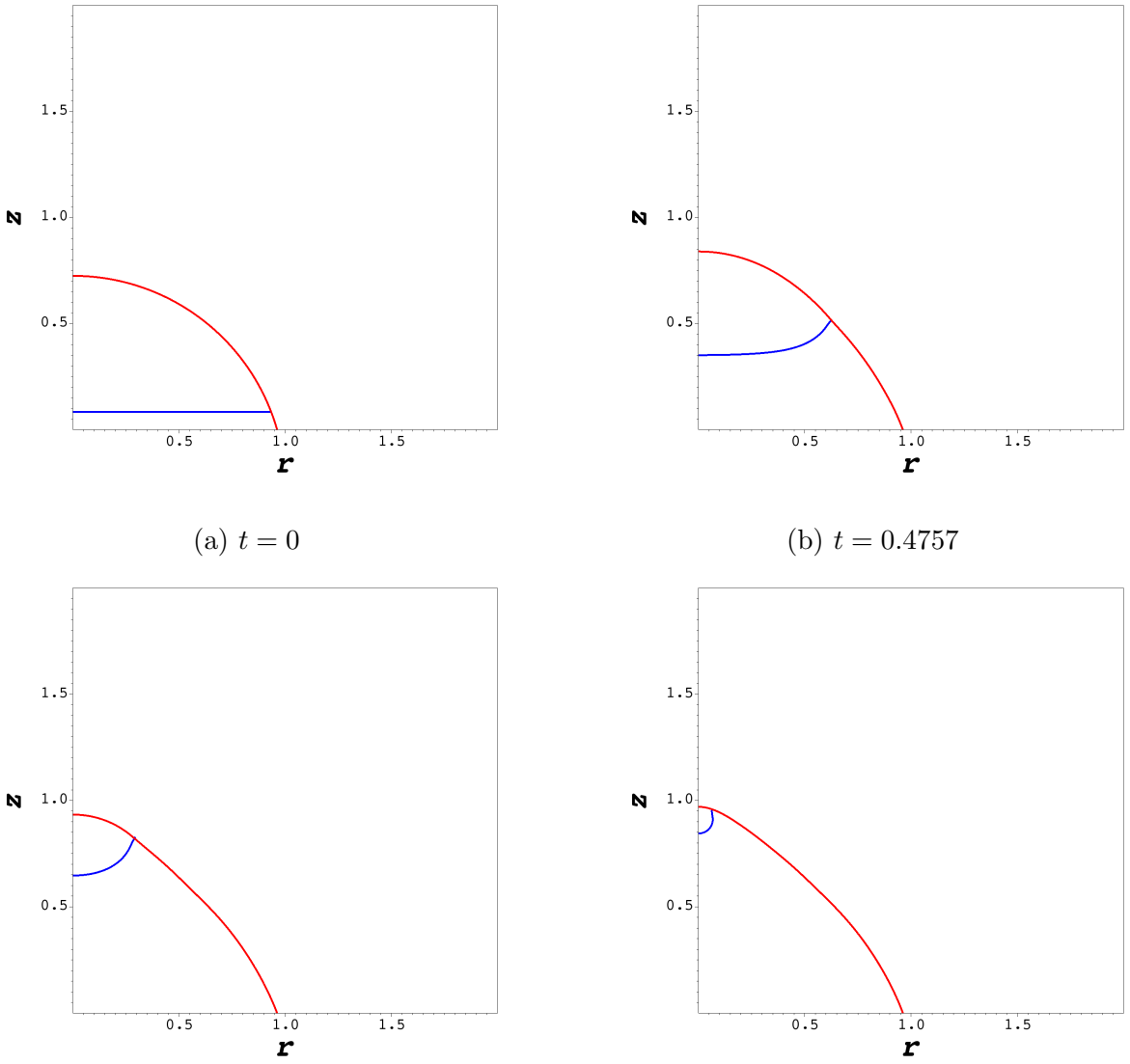

(a) $t = 0$ (b) $t = 0.4757$

(c) $t = 0.8507$ (d) $t = 0.9932$

Figure 6.9: Time evolution of a freezing droplet for $\sigma_{sl} = 0.8$. Red: solid–air interface; blue: water–ice interface. The snapshots illustrate the coupled inward motion of the water–ice front and outward growth of the solid phase, leading to the formation of a pointed tip.

To elucidate the thermal mechanisms underlying the interface motion, we examine the temperature field inside the droplet during solidification. The relevant nondimensional parameters for this case are Ste = 12.53 and Pe = 1.01, indicating that sensible heat and latent heat are both important and that thermal advection and diffusion are of comparable magnitude.

The density ratio is $\rho_s/\rho_l = 0.9162$, and the thermal conductivity ratio $k_s/k_l = 3.99$, which promotes efficient heat conduction through the solid phase. In addition, the viscosity contrast $\eta_s/\eta_l \approx 300$ effectively suppresses motion inside the solid region, while allowing limited flow in the liquid phase.

Figure 6.10 shows the temperature field at four representative times, $t = 0.1t_f$, $0.3t_f$, $0.6t_f$, and $0.9t_f$, where t_f denotes the total freezing time. At early stages, a strong thermal boundary layer develops near the cold substrate. As freezing proceeds, the thermal gradient propagates upward and the isotherms bend in response to the evolving interface geometry. By $t = 0.9t_f$, most of the droplet interior has cooled close to T_M, and the solid phase has advanced toward the top of the droplet. The temperature evolution is fully consistent with the interface motion observed in Fig. 6.9 and confirms the correct treatment of latent heat through the energy law (3.29).

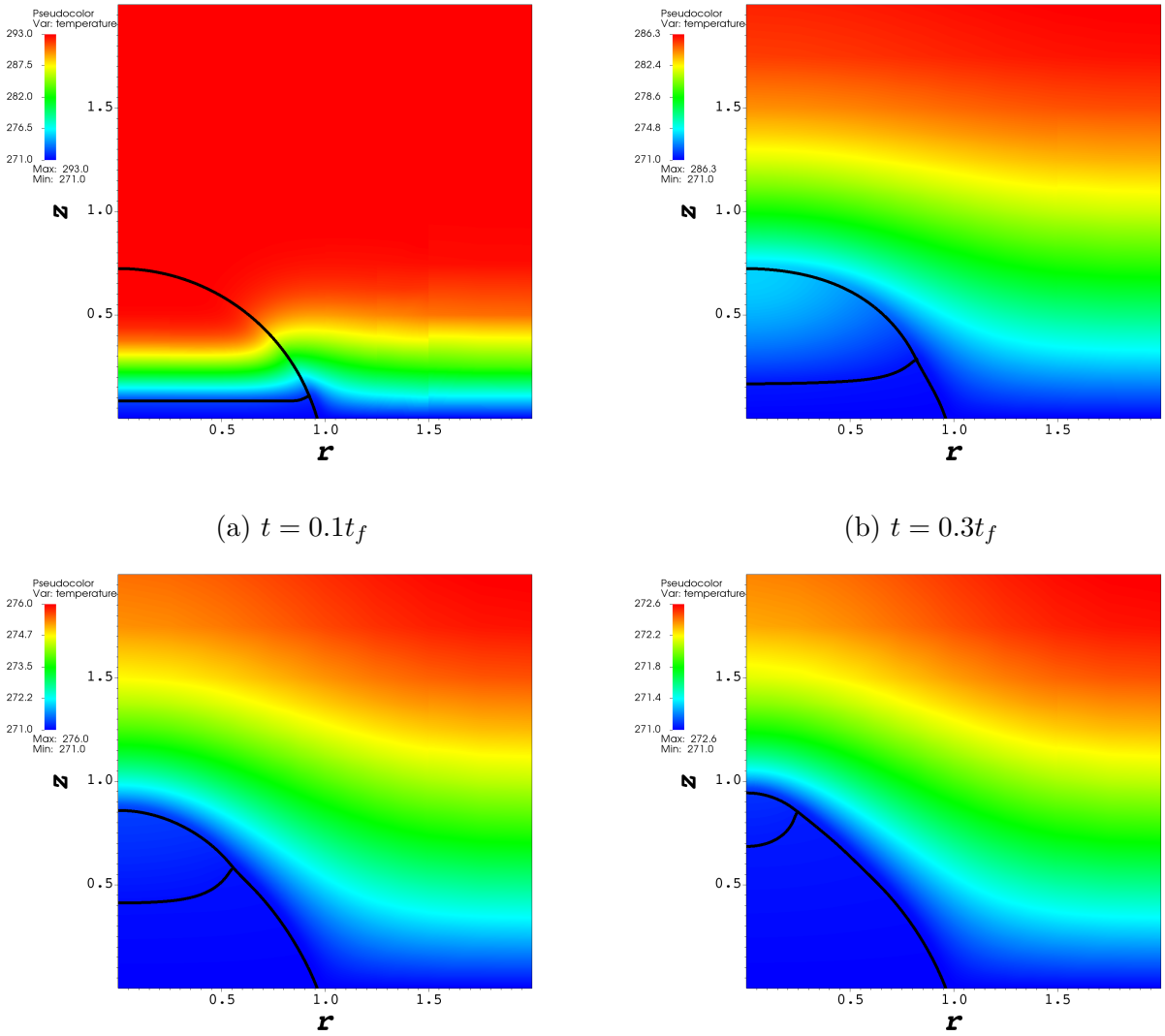

(a) $t = 0.1t_f$

(b) $t = 0.3t_f$

(c) $t = 0.6t_f$

(d) $t = 0.9t_f$

Figure 6.10: Temperature field inside the droplet at different times during solidification. The colour map shows the instantaneous temperature distribution, illustrating the upward propagation of the thermal gradient and its coupling with interface evolution.

An important validation of the model is obtained by comparing the simulated droplet shapes with experimental measurements. Figure 6.11 shows the initial and final droplet profiles for the reference parameter set. The numerical results reproduce the experimentally observed final shape with high accuracy, demonstrating that the model captures the coupled effects of curvature, latent heat, and volume expansion during freezing.

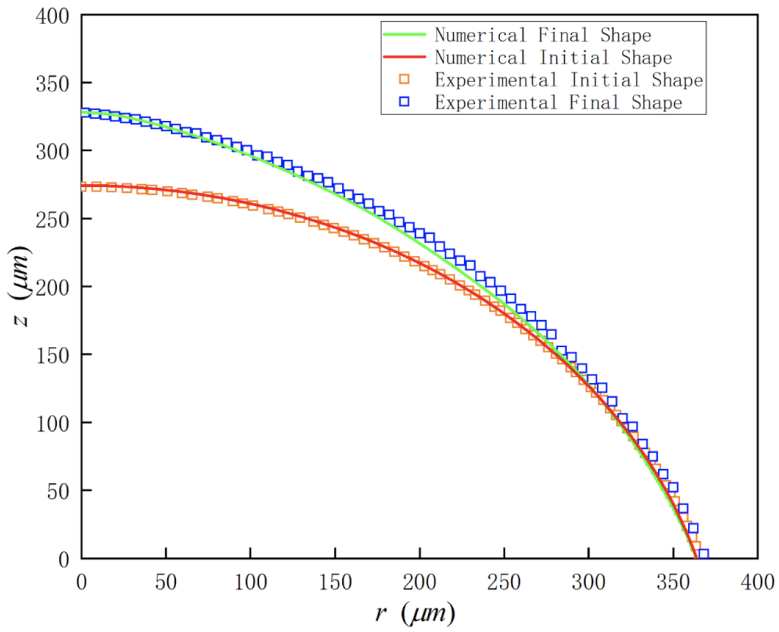

Figure 6.11: Comparison of the initial and final droplet shapes from numerical simulations and experimental data. The solid–liquid interfacial tension is $\sigma_{sl} = 0.7$, and all other material parameters are fixed as described in the text.

Finally, we investigate the influence of the solid–liquid interfacial tension σ_{sl} on the final droplet morphology. Figure 6.12 compares simulated interface profiles for different values of σ_{sl} with experimental data. Increasing σ_{sl} leads to a sharper and more pronounced tip, while smaller values of σ_{sl} result in a rounder cap. This trend reflects the role of surface tension in penalizing interface curvature and is consistent with physical intuition as well as experimental observations. The good agreement across a range of interfacial tension values further demonstrates the robustness of the proposed phase-field formulation.

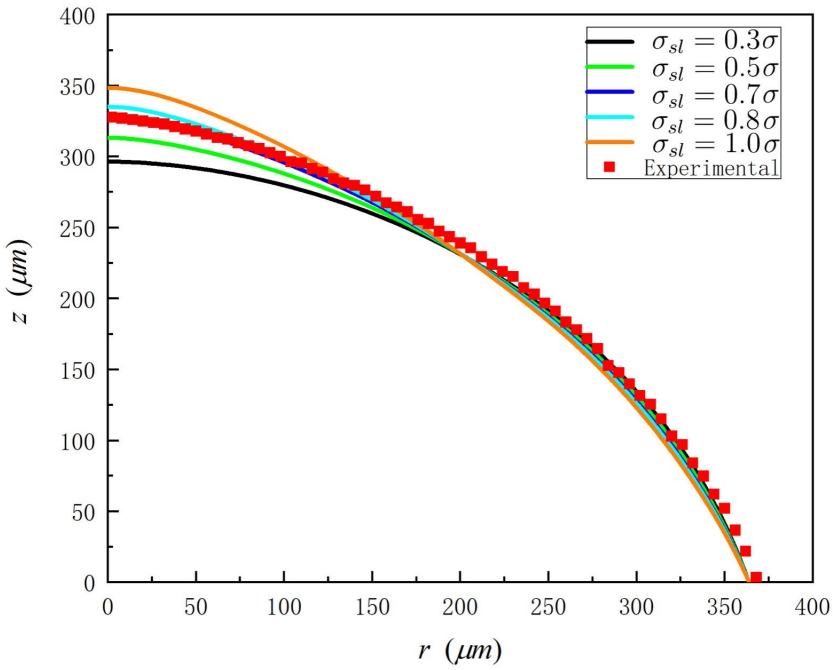

Figure 6.12: Final droplet shapes for different normalized solid–liquid interfacial tension values σ_{sl}, compared with experimental measurements.

Chapter 7

Summary

This dissertation presents a thermodynamically consistent phase-field formulation for the non-isothermal solidification of a three-phase water–ice–air system. The model is constructed from the entropy inequality, ensuring non-negative entropy production throughout the evolution and enforcing full compliance with the second law of thermodynamics. Within this framework, the water–ice transition, the deformable liquid–gas interface, density variation, and latent-heat effects are incorporated in a unified manner through the phase-field variables ϕ and ψ, whose governing equations are given by the Cahn–Hilliard equation (3.49), the Allen–Cahn equation (3.51), the quasi-incompressible momentum balance (3.54), the continuity relation (3.55), and the internal energy law (3.29). The chemical potentials associated with both phases are derived consistently from the free energy using (3.50) and (3.52), allowing all interfacial forces to arise naturally from the underlying thermodynamic structure.

To solve this coupled nonlinear system, we develop a finite-element discretization based on the weak formulations in Chapter 5. A semi-implicit θ-scheme is employed for time integration, and all nonlinear terms are linearized using first-order Taylor expansion in the increments of ϕ, ψ, and $\mathbf{v}$. This treatment is applied uniformly to the density $\rho(\phi, \psi)$, the advective contributions, and the chemical potentials in (3.50) and (3.52). The resulting

discrete equations preserve the mass conservation inherent in the Cahn–Hilliard equation and maintain the stability properties of the continuous model. The final weak forms of the discrete system are given by (5.3), (5.5), (5.1), (5.2), and (5.7).

A series of benchmark tests are performed to validate both the physical fidelity of the model and the robustness of the numerical method.

- **Gibbs–Thomson effect:** By considering a two-phase solid–liquid system, we demonstrate that the model reproduces the curvature-induced shift in the melting temperature, matching the theoretical relation derived in (6.3).
- **Clausius–Clapeyron relation:** With zero curvature, the simulations recover the pressure-dependent equilibrium temperature described by (6.1), showing excellent quantitative agreement across a wide range of pressure differences.
- **Volume expansion in the Stefan problem:** The model captures the density-driven motion of the liquid and solid interfaces, maintaining the ratio $\Delta l_w/\Delta l_i = -\rho_s/\rho_l$ dictated by mass conservation.
- **Freezing droplet:** Numerical predictions of the droplet profile and tip formation show close agreement with experimental observations and accurately reflect the influence of the solid–liquid surface tension.

These benchmark results demonstrate that the numerical scheme—built upon finite-element weak formulations, semi-implicit θ-time discretization, and Newton linearization—provides a stable and accurate tool for simulating non-isothermal, three-phase solidification. The ability of the model to recover classical thermodynamic relations, capture realistic interfacial dynamics, and reproduce experimentally observed droplet shapes confirms that it offers a reliable and unified framework for studying complex multiphase phase-change phenomena.

Bibliography

[1] Helmut Abels, Harald Garcke, and Günther Grün. THERMODYNAMICALLY CONSISTENT, FRAME INDIFFERENT DIFFUSE INTERFACE MODELS FOR INCOMPRESSIBLE TWO-PHASE FLOWS WITH DIFFERENT DENSITIES. *Mathematical Models and Methods in Applied Sciences*, 22(03), 11 2011. doi: 10.1142/s0218202511500138. URL https://doi.org/10.1142/s0218202511500138.

[2] Saad Akhtar, Minghan Xu, Mohammaderfan Mohit, and Agus P. Sasmito. A comprehensive review of modeling water solidification for droplet freezing applications. *Renewable and Sustainable Energy Reviews*, 188:113768, 2023. ISSN 1364-0321. doi: https://doi.org/10.1016/j.rser.2023.113768. URL https://www.sciencedirect.com/science/article/pii/S1364032123006251.

[3] D. M. Anderson, G. B. McFadden, and A. A. Wheeler. Diffuse-interface methods in fluid mechanics. *Annual Review of Fluid Mechanics*, 30(Volume 30, 1998):139–165, 1998. ISSN 1545-4479. doi: https://doi.org/10.1146/annurev.fluid.30.1.139. URL https://www.annualreviews.org/content/journals/10.1146/annurev.fluid.30.1.139.

[4] D. M. Anderson, G. B. McFadden, and A. A. Wheeler. A phase-field model of solidification with convection. *Physica D: Nonlinear Phenomena*, 135(1-2):175–194, 2000. doi: 10.1016/S0167-2789(99)00140-6.

[5] Daniel Arndt, Wolfgang Bangerth, Denis Davydov, Timo Heister, Luca Heltai, Martin

Kronbichler, Matthias Maier, Bruno Turcksin, and David Wells. *The deal.II Library, Version 9.0*, 2018. https://www.dealii.org.

[6] Peter Atkins and Julio de Paula. *Atkins' Physical Chemistry*. Oxford University Press, 8th edition, 2006.

[7] F. Boyer, C. Lapuerta, S. Minjeaud, B. Piar, and M. Quintard. Cahn–Hilliard/Navier–Stokes model for the simulation of Three-Phase flows. *Transport in Porous Media*, 82(3):463–483, 5 2009. doi: 10.1007/s11242-009-9408-z. URL https://doi.org/10.1007/s11242-009-9408-z.

[8] Franck Boyer. A theoretical and numerical model for the study of incompressible mixture flows. *Computers Fluids*, 31(1):41–68, 1 2002. doi: 10.1016/s0045-7930(00)00031-1. URL https://doi.org/10.1016/s0045-7930(00)00031-1.

[9] G. Caginalp. Stefan and Hele-Shaw type models as asymptotic limits of the phase-field equations. *Physical review. A, General physics*, 39(11):5887–5896, 6 1989. doi: 10.1103/physreva.39.5887. URL https://doi.org/10.1103/physreva.39.5887.

[10] Herbert B. Callen and Robert B. Griffiths. Thermodynamics and an introduction to thermostatistics. *American Journal of Physics*, 55(9):860–861, 9 1987. doi: 10.1119/1.14986. URL https://doi.org/10.1119/1.14986.

[11] Gaurav Chaudhary and Ri Li. Freezing of water droplets on solid surfaces: An experimental and numerical study. *Experimental Thermal and Fluid Science*, 57:86–93, 4 2014. doi: 10.1016/j.expthermflusci.2014.04.007. URL https://doi.org/10.1016/j.expthermflusci.2014.04.007.

[12] Ravi Chella and Jorge Viñals. Mixing of a two-phase fluid by cavity flow. *Physical review. E, Statistical physics, plasmas, fluids, and related interdisciplinary topics*, 53 (4):3832–3840, 4 1996. doi: 10.1103/physreve.53.3832. URL https://doi.org/10.1103/physreve.53.3832.

[13] Long-Qing Chen. Phase-Field models for microstructure evolution. *Annual Review of Materials Research*, 32(1):113–140, 7 2002. doi: 10.1146/annurev.matsci.32.112001.132041. URL https://doi.org/10.1146/annurev.matsci.32.112001.132041.

[14] J G Dash, Haiying Fu, and J S Wettlaufer. The premelting of ice and its environmental consequences. *Reports on Progress in Physics*, 58(1):115–167, 1 1995. doi: 10.1088/0034-4885/58/1/003. URL https://doi.org/10.1088/0034-4885/58/1/003.

[15] Hang Ding, Peter D.M. Spelt, and Chang Shu. Diffuse interface model for incompressible two-phase flows with large density ratios. *Journal of Computational Physics*, 226(2):2078–2095, 7 2007. doi: 10.1016/j.jcp.2007.06.028. URL https://doi.org/10.1016/j.jcp.2007.06.028.

[16] S. Dong. An efficient algorithm for incompressible N-phase flows. *Journal of Computational Physics*, 276:691–728, 8 2014. doi: 10.1016/j.jcp.2014.08.002. URL https://doi.org/10.1016/j.jcp.2014.08.002.

[17] S. Dong. Physical formulation and numerical algorithm for simulating N immiscible incompressible fluids involving general order parameters. *Journal of Computational Physics*, 283:98–128, 12 2014. doi: 10.1016/j.jcp.2014.11.039. URL https://doi.org/10.1016/j.jcp.2014.11.039.

[18] Heike Emmerich. Advances of and by phase-field modelling in condensed-matter physics. *Advances In Physics*, 57(1):1–87, 1 2008. doi: 10.1080/00018730701822522. URL https://doi.org/10.1080/00018730701822522.

[19] D. J. Eyre. Unconditionally gradient stable time marching the cahn–hilliard equation. In *Computational and Mathematical Models of Microstructural Evolution*, volume 529 of *Materials Research Society Symposium Proceedings*, pages 39–46, 1998.

[20] A. Fuller, K. Kant, and R. Pitchumani. Analysis of freezing of a sessile water droplet on surfaces over a range of wettability. *Journal of Colloid and Interface Science*, 653:

960–970, 9 2023. doi: 10.1016/j.jcis.2023.09.119. URL https://doi.org/10.1016/j.jcis.2023.09.119.

[21] E. A. Guggenheim and Harold W. Woolley. *Thermodynamics: an advanced treatment for chemists and physicists*, volume 10. Pergamon Press, 11 1957. doi: 10.1063/1.3060168. URL https://doi.org/10.1063/1.3060168.

[22] F. Guillen-Gonzalez and G. Tierra. On linear schemes for a cahn–hilliard diffuse interface model. *Journal of Computational Physics*, 234:140–171, 2013. doi: 10.1016/j.jcp.2012.09.020.

[23] Z. Guo and P. Lin. A thermodynamically consistent phase-field model for two-phase flows with thermocapillary effects. *Journal of Fluid Mechanics*, 766:226–271, 2 2015. doi: 10.1017/jfm.2014.696. URL https://doi.org/10.1017/jfm.2014.696.

[24] Z. Guo, P. Lin, and J.S. Lowengrub. A numerical method for the quasi-incompressible Cahn–Hilliard–Navier–Stokes equations for variable density flows with a discrete energy law. *Journal of Computational Physics*, 276:486–507, 8 2014. doi: 10.1016/j.jcp.2014.07.038. URL https://doi.org/10.1016/j.jcp.2014.07.038.

[25] Morton E. Gurtin, Debra Polignone, and Jorge Viñals. TWO-PHASE BINARY FLUIDS AND IMMISCIBLE FLUIDS DESCRIBED BY AN ORDER PARAMETER. *Mathematical Models and Methods in Applied Sciences*, 06(06):815–831, 9 1996. doi: 10.1142/s0218202596000341. URL https://doi.org/10.1142/s0218202596000341.

[26] Yoshimichi Hagiwara, Shoji Ishikawa, Ryota Kimura, and Kazumasa Toyohara. Ice growth and interface oscillation of water droplets impinged on a cooling surface. *Journal of Crystal Growth*, 468:46–53, 2017. ISSN 0022-0248. doi: https://doi.org/10.1016/j.jcrysgro.2016.12.095. URL https://www.sciencedirect.com/science/article/pii/S0022024816309642. The 18th International Conference on Crystal Growth and Epitaxy (ICCGE-18).

[27] P. C. Hohenberg and B. I. Halperin. Theory of dynamic critical phenomena. *Reviews of Modern Physics*, 49(3):435–479, 7 1977. doi: 10.1103/revmodphys.49.435. URL https://doi.org/10.1103/revmodphys.49.435.

[28] S. R. Hosseini, M. Moghimi, and N. M. Nouri. On the role of surface morphology in impacting-freezing dynamics of supercooled droplets. *Scientific Reports*, 14(1): 12585, 6 2024. doi: 10.1038/s41598-024-61826-5. URL https://doi.org/10.1038/s41598-024-61826-5.

[29] Jiangxu Huang, Lei Wang, Zhenhua Chai, and Baochang Shi. Phase-field-based lattice boltzmann method for containerless freezing. *Phys. Rev. E*, 110:035301, Sep 2024. doi: 10.1103/PhysRevE.110.035301. URL https://link.aps.org/doi/10.1103/PhysRevE.110.035301.

[30] Ziyang Huang, Guang Lin, and Arezoo M. Ardekani. Consistent, essentially conservative and balanced-force Phase-Field method to model incompressible two-phase flows. *Journal of Computational Physics*, 406:109192, 12 2019. doi: 10.1016/j.jcp.2019.109192. URL https://doi.org/10.1016/j.jcp.2019.109192.

[31] David Jacqmin. Calculation of Two-Phase Navier–Stokes flows using Phase-Field modeling. *Journal of Computational Physics*, 155(1):96–127, 10 1999. doi: 10.1006/jcph.1999.6332. URL https://doi.org/10.1006/jcph.1999.6332.

[32] Stefan Jung, Manish K. Tiwari, N. Vuong Doan, and Dimos Poulikakos. Mechanism of supercooled droplet freezing on surfaces. *Nature Communications*, 3(1), 1 2012. doi: 10.1038/ncomms1630. URL https://doi.org/10.1038/ncomms1630.

[33] Linn Karlsson, Henrik Lycksam, Anna-Lena Ljung, Per Gren, and T. Staffan Lundström. Experimental study of the internal flow in freezing water droplets on a cold surface. *Experiments in Fluids*, 60(12), 11 2019. doi: 10.1007/s00348-019-2823-1. URL https://doi.org/10.1007/s00348-019-2823-1.

[34] Alain Karma and Wouter-Jan Rappel. Phase-field method for computationally efficient modeling of solidification with arbitrary interface kinetics. *Physical review. E, Statistical physics, plasmas, fluids, and related interdisciplinary topics*, 53(4):R3017–R3020, 4 1996. doi: 10.1103/physreve.53.r3017. URL https://doi.org/10.1103/physreve.53.r3017.

[35] Junseok Kim. Phase-Field models for Multi-Component fluid flows. *Communications in Computational Physics*, 12(3):613–661, 5 2012. doi: 10.4208/cicp.301110.040811a. URL https://doi.org/10.4208/cicp.301110.040811a.

[36] Junseok Kim and John Lowengrub. Phase field modeling and simulation of three-phase flows. *Interfaces and Free Boundaries Mathematical Analysis Computation and Applications*, 7(4):435–466, 12 2005. doi: 10.4171/ifb/132. URL https://doi.org/10.4171/ifb/132.

[37] Weiliang Kong, Liping Wang, Peixiang Bian, and Hong Liu. Effect of surface wettability on impact-freezing of supercooled large water droplet. *Experimental Thermal and Fluid Science*, 130:110508, 8 2021. doi: 10.1016/j.expthermflusci.2021.110508. URL https://doi.org/10.1016/j.expthermflusci.2021.110508.

[38] Xiaoli Li and Jie Shen. Efficient linear and unconditionally energy stable schemes for the modified phase field crystal equation. *Science China Mathematics*, 65(10):2201–2218, 9 2021. doi: 10.1007/s11425-020-1867-8. URL https://doi.org/10.1007/s11425-020-1867-8.

[39] J. Lowengrub and L. Truskinovsky. Quasi–incompressible Cahn–Hilliard fluids and topological transitions. *Proceedings of the Royal Society A Mathematical Physical and Engineering Sciences*, 454(1978):2617–2654, 10 1998. doi: 10.1098/rspa.1998.0273. URL https://doi.org/10.1098/rspa.1998.0273.

[40] A. G. Marín, O. R. Enríquez, P. Brunet, P. Colinet, and J. H. Snoeijer. Universality

of tip Singularity formation in freezing water drops. *Physical Review Letters*, 113(5): 054301, 7 2014. doi: 10.1103/physrevlett.113.054301. URL https://doi.org/10.1103/physrevlett.113.054301.

[41] R.S. Qin and H.K. Bhadeshia. Phase field method. *Materials Science and Technology*, 26(7):803 – 811, 2010. doi: 10.1179/174328409X453190. URL https://www.scopus.com/inward/record.uri?eid=2-s2.0-77955318688&doi=10.1179%2f174328409X453190&partnerID=40&md5=4ff1ba3d344885455bccd10bd98192dc. Cited by: 167.

[42] Robert Rosenberg. Why is Ice Slippery? *Physics Today*, 58(12):50–54, 12 2005. doi: 10.1063/1.2169444. URL https://doi.org/10.1063/1.2169444.

[43] W.W. Schultz, M.G. Worster, and D.M. Anderson. Solidifying sessile water droplets. *Springer eBooks*, pages 209–226, 01 2001. doi: 10.1007/978-94-015-9807-1_24.

[44] Yuheng Shang, Matic Može, Yunus Tansu Aksoy, Sylvie Castagne, David Seveno, Iztok Golobič, and Maria Rosaria Vetrano. Effect of surface wettability on dynamic behaviors and freezing mechanisms of water droplets impacting cold surfaces. *Physics of Fluids*, 36(9), 9 2024. doi: 10.1063/5.0222155. URL https://doi.org/10.1063/5.0222155.

[45] J. Shen and X. Yang. Numerical approximations of allen–cahn and cahn–hilliard equations. *Discrete and Continuous Dynamical Systems Series A*, 28(4):1669–1691, 2010. doi: 10.3934/dcds.2010.28.1669.

[46] Jie Shen and Xiaofeng Yang. A Phase-Field Model and Its Numerical Approximation for Two-Phase Incompressible Flows with Different Densities and Viscosities. *SIAM Journal on Scientific Computing*, 32(3):1159–1179, 1 2010. doi: 10.1137/09075860x. URL https://doi.org/10.1137/09075860x.

[47] Jie Shen, Jie Xu, and Jiang Yang. The scalar auxiliary variable (SAV) approach for

gradient flows. *Journal of Computational Physics*, 353:407–416, 10 2017. doi: 10.1016/j.jcp.2017.10.021. URL https://doi.org/10.1016/j.jcp.2017.10.021.

[48] H. Shetabivash, A. Dolatabadi, and M. Paraschivoiu. A multiple level-set approach for modelling containerless freezing process. *Journal of Computational Physics*, 415: 109527, 2020. ISSN 0021-9991. doi: https://doi.org/10.1016/j.jcp.2020.109527. URL https://www.sciencedirect.com/science/article/pii/S0021999120303016.

[49] Jacco H. Snoeijer and Philippe Brunet. Pointy ice-drops: How water freezes into a singular shape. *American Journal of Physics*, 80(9):764–771, 8 2012. doi: 10.1119/1.4726201. URL https://doi.org/10.1119/1.4726201.

[50] Faryar Tavakoli, Stephen H. Davis, and H. Pirouz Kavehpour. Freezing of supercooled water drops on cold solid substrates: initiation and mechanism. *Journal of Coatings Technology and Research*, 12(5):869–875, 6 2015. doi: 10.1007/s11998-015-9693-0. URL https://doi.org/10.1007/s11998-015-9693-0.

[51] Moussa Tembely and Ali Dolatabadi. A comprehensive model for predicting droplet freezing features on a cold substrate. *Journal of Fluid Mechanics*, 859:566–585, 2019. doi: 10.1017/jfm.2018.839.

[52] Gyula I Tóth and Wenyue Ma. Phase-field modelling of the effect of density change on solidification revisited: model development and analytical solutions for single component materials. *Journal of Physics Condensed Matter*, 32(20):205402, 1 2020. doi: 10.1088/1361-648x/ab670e. URL https://doi.org/10.1088/1361-648x/ab670e.

[53] S.-l. Wang, R.F. Sekerka, A.A. Wheeler, B.T. Murray, S.R. Coriell, R.J. Braun, and G.B. McFadden. Thermodynamically-consistent phase-field models for solidification. *Physica D Nonlinear Phenomena*, 69(1-2):189–200, 11 1993. doi: 10.1016/0167-2789(93)90189-8. URL https://doi.org/10.1016/0167-2789(93)90189-8.

[54] Zhihua Wang, Lijing Zhou, Wenqiang Zhang, Xiaorong Wang, Shuguang Li, and Xuerui Mao. An energy-stable phase-field model for droplet icing simulations. *Journal of Computational Physics*, page 113792, 1 2025. doi: 10.1016/j.jcp.2025.113792. URL https://doi.org/10.1016/j.jcp.2025.113792.

[55] J. S. Wettlaufer. Impurity effects in the premelting of ice. *Physical Review Letters*, 82 (12):2516–2519, 3 1999. doi: 10.1103/physrevlett.82.2516. URL https://doi.org/10.1103/physrevlett.82.2516.

[56] Masafumi Yamazaki, Aleksandar Jemcov, and Hirotaka Sakaue. A review on the current status of icing physics and mitigation in aviation. *Aerospace*, 8(7), 2021. ISSN 2226-4310. doi: 10.3390/aerospace8070188. URL https://www.mdpi.com/2226-4310/8/7/188.

[57] X. Yang. Linear, first and second-order, unconditionally energy stable numerical schemes for the phase field model of homopolymer blends. *Journal of Computational Physics*, 327:294–316, 2016. doi: 10.1016/j.jcp.2016.09.029.

[58] Xiaofeng Yang and Lili Ju. Linear and unconditionally energy stable schemes for the binary fluid–surfactant phase field model. *Computer Methods in Applied Mechanics and Engineering*, 318:1005–1029, 2 2017. doi: 10.1016/j.cma.2017.02.011. URL https://doi.org/10.1016/j.cma.2017.02.011.

[59] Xiaofeng Yang, Jia Zhao, and Qi Wang. Numerical approximations for the molecular beam epitaxial growth model based on the invariant energy quadratization method. *Journal of Computational Physics*, 333:104–127, 12 2016. doi: 10.1016/j.jcp.2016.12.025. URL https://doi.org/10.1016/j.jcp.2016.12.025.

[60] Xiaofeng Yang, Jia Zhao, Qi Wang, and Jie Shen. Numerical approximations for a three-component cahn–hilliard phase-field model based on the invariant energy quadratization method. *Mathematical Models and Methods in Applied Sciences*, 27(11):1993–

2030, 7 2017. doi: 10.1142/s0218202517500373. URL https://doi.org/10.1142/s0218202517500373.

[61] Haijun Yu and Xiaofeng Yang. Numerical approximations for a phase-field moving contact line model with variable densities and viscosities. *Journal of Computational Physics*, 334:665–686, 1 2017. doi: 10.1016/j.jcp.2017.01.026. URL https://doi.org/10.1016/j.jcp.2017.01.026.

[62] Pengtao Yue. Thermodynamically consistent phase-field modelling of contact angle hysteresis. *Journal of Fluid Mechanics*, 899, 7 2020. doi: 10.1017/jfm.2020.465. URL https://doi.org/10.1017/jfm.2020.465.

[63] Mark Waldo Zemansky and Richard H Dittman. *Heat and thermodynamics : an intermediate textbook*. McGraw-Hill, 1 1981. URL http://ci.nii.ac.jp/ncid/BA3391839X.

[64] Hao Zeng, Sijia Lyu, Dominique Legendre, and Chao Sun. Influence of gravity on the freezing dynamics of drops on a solid surface. *Phys. Rev. Fluids*, 7:103605, Oct 2022. doi: 10.1103/PhysRevFluids.7.103605. URL https://link.aps.org/doi/10.1103/PhysRevFluids.7.103605.

[65] Chaoyang Zhang, Hui Zhang, Wenzhen Fang, Yugang Zhao, and Chun Yang. Axisymmetric lattice Boltzmann model for simulating the freezing process of a sessile water droplet with volume change. *Physical review. E*, 101(2), 2 2020. doi: 10.1103/physreve.101.023314. URL https://doi.org/10.1103/physreve.101.023314.

[66] Wenqiang Zhang, Armin Shahmardi, Kwing so Choi, Outi Tammisola, Luca Brandt, and Xuerui Mao. A phase-field method for three-phase flows with icing. *Journal of Computational Physics*, 458:111104, 2022. ISSN 0021-9991. doi: https://doi.org/10.1016/j.jcp.2022.111104. URL https://www.sciencedirect.com/science/article/pii/S0021999122001668.

[67] Jia Zhao, Xiaofeng Yang, Yuezheng Gong, and Qi Wang. A novel linear second order unconditionally energy stable scheme for a hydrodynamic Q-tensor model of liquid crystals. *Computer Methods in Applied Mechanics and Engineering*, 318:803–825, 2 2017. doi: 10.1016/j.cma.2017.01.031. URL https://doi.org/10.1016/j.cma.2017.01.031.

Appendices

Appendix A

First Appendix

A.1 θ-scheme Chemical Potential for ϕ

We want to derive the semi-discrete form for the equation (5.4):

$$\underbrace{(\mu_\phi, \tilde{\mu_\phi})}_{\textbf{Term}1} = \underbrace{\left(\left[r(\psi)r'(\phi)L - \frac{\partial c}{\partial \phi}T_M\right]\left(1 - \frac{T}{T_M}\right), \tilde{\mu_\phi}\right)}_{\textbf{Term}2} - \underbrace{\left(\frac{\partial c}{\partial \phi}T\ln\frac{T}{T_M}, \tilde{\mu_\phi}\right)}_{\textbf{Term}3}$$
$$+ \underbrace{(\lambda_\phi\omega'(\phi), \tilde{\mu_\phi}) + \left(r'(\phi)\lambda_\psi\left(\omega(\psi) + \frac{1}{2}|\nabla\psi|^2\right), \tilde{\mu_\phi}\right)}_{\textbf{Term}4} - \underbrace{\left(\frac{p - p_0}{\rho^2}\frac{\partial \rho}{\partial \phi}, \tilde{\mu_\phi}\right)}_{\textbf{Term}5}$$
$$- \underbrace{\left(\frac{1}{\rho}\nabla\cdot(\rho\lambda_\phi\nabla\phi), \tilde{\mu_\phi}\right)}_{\textbf{Term}6}$$

(**Term** 1)

$$(\mu_\phi, \tilde{\mu_\phi})$$

$$\begin{aligned} \text{RHS} &= -\mu_\phi^{*,\theta} \\ \text{MAT} &= \delta\mu_\phi \end{aligned} \tag{A.1}$$

(**Term** 2)

$$\left(\left[r(\psi)r'(\phi)L - \frac{\partial c}{\partial \phi}T_M\right]\left(1 - \frac{T}{T_M}\right), \tilde{\mu_\phi}\right)$$

$$\text{RHS} = \left(L \cdot r\left(\psi^{*,\theta}\right) r'\left(\phi^{*,\theta}\right) - T_M \cdot \frac{\partial C^{*,\theta}}{\partial \phi}\right)\left(1 - \frac{T^*,\theta}{T_M}\right) \tag{A.2}$$

$$\begin{aligned}\text{MAT} = &\left(L \cdot r\left(\psi^{*,\theta}\right) r'\left(\phi^{*,\theta}\right) - T_M \frac{\partial C^{*,\theta}}{\partial \phi}\right)\frac{\theta \delta T}{T_M} \\ &- \left(L \cdot \left(r\left(\psi^{*,\theta}\right) r''\left(\phi^{*,\theta}\right)\theta\delta\phi + r'\left(\phi^{*,\theta}\right) r'\left(\psi^{*,\theta}\right)\theta\delta\psi\right) - T_M \cdot C_\phi^{*,\theta}(\delta\phi, \delta\psi)\right) \cdot \left(1 - \frac{T^{*,\theta}}{T_M}\right)\end{aligned} \tag{A.3}$$

$$\text{where } \left.\frac{\partial C}{\partial \phi}\right|_\theta = \frac{\partial C^{*,\theta}}{\partial \phi} + C_\phi^{*,\theta}(\delta\phi, \delta\psi) \tag{A.4}$$

$$\frac{\partial C^{*,\theta}}{\partial \phi} = C_l r'\left(\phi^{*,\theta}\right) r\left(\psi^{*,\theta}\right) + C_s r'\left(\phi^{*,\theta}\right) - C_s r'\left(\phi^{*,\theta}\right) r\left(\psi^{*,\theta}\right) - C_g r'\left(\phi^{*,\theta}\right) \tag{A.5}$$

$$\begin{aligned}C_\phi^{*,\theta}(\delta\phi, \delta\psi) = &\left[C_l r\left(\psi^{*,\theta}\right) r''\left(\phi^{*,\theta}\right) + C_s r''\left(\phi^{*,\theta}\right) - C_s r\left(\psi^{*,\theta}\right) r''\left(\phi^{*,\theta}\right) - C_g r''\left(\phi^{*,\theta}\right)\right] \cdot \theta\delta\phi \\ &+ \left[C_l r'\left(\phi^{*,\theta}\right) r'\left(\psi^{*,\theta}\right) - C_s r'\left(\phi^{*,\theta}\right) r'\left(\psi^{*,\theta}\right)\right] \cdot \theta\delta\psi\end{aligned} \tag{A.6}$$

(**Term** 3)

$$-\left(\frac{\partial c}{\partial \phi} T \ln \frac{T}{T_M}, \tilde{\mu_\phi}\right)$$

$$\text{RHS} = -\frac{\partial C^{*,\theta}}{\partial \phi} \cdot T^{*,\theta} \ln \frac{T^{*,\theta}}{T_M} \tag{A.7}$$

$$\text{MAT} = C_\phi^{*,\theta}\left(\delta\phi, \delta\psi\right) \cdot T^{*,\theta} \ln \frac{T^{*,\theta}}{T_M} + \frac{\partial C^{*,\theta}}{\partial \phi} \cdot \theta\delta T\left(\ln \frac{T^{*,\theta}}{T_M} + 1\right) \tag{A.8}$$

(**Term** 4)

$$(\lambda_\phi \omega'(\phi), \tilde{\mu_\phi}) + \left(r'(\phi)\lambda_\psi\left(\omega(\psi) + \frac{1}{2}|\nabla\psi|^2\right), \tilde{\mu_\phi}\right)$$

$$\text{RHS} = \lambda_\phi \omega' \left(\phi^{*,\theta}\right) + \lambda_\psi r' \left(\phi^{*,\theta}\right) \cdot \left[\omega \left(\psi^{*,\theta}\right) + \frac{1}{2} \left|\nabla \psi^{*,\theta}\right|^2\right] \tag{A.9}$$

$$\begin{aligned} \text{MAT} = & - \lambda_\phi \omega'' \left(\phi^{*,\theta}\right) \cdot \theta\delta\phi - \lambda_\psi r'' \left(\phi^{*,\theta}\right) \theta\delta\phi \cdot \left[\omega \left(\psi^{*,\theta}\right) + \frac{1}{2} \left|\nabla \psi^{*,\theta}\right|^2\right] \\ & - \lambda_\psi r' \left(\phi^{*,\theta}\right) \cdot \left[\omega' \left(\psi^{*,\theta}\right) \theta\delta\psi + \theta\delta\nabla\psi \cdot \nabla\psi^{*,\theta}\right] \end{aligned} \tag{A.10}$$

(**Term** 5)

$$- \left(\frac{p^*}{\rho^2} \frac{\partial \rho}{\partial \phi}, \tilde{\mu_\phi}\right)$$

$$\text{RHS} = \left(p^{*,\theta} - p_0\right) \cdot \left[\frac{1}{\rho_l} \left(r \left(\psi^{*,\theta}\right) r' \left(\phi^{*,\theta}\right)\right) + \frac{1}{\rho_s} \left(r' \left(\phi^{*,\theta}\right) - r \left(\psi^{*,\theta}\right) r' \left(\phi^{*,\theta}\right)\right) - \frac{1}{\rho_g} \cdot r' \left(\phi^{*,\theta}\right)\right] \tag{A.11}$$

$$\begin{aligned} \text{MAT} = & - \delta p \cdot \left[\frac{1}{\rho_l} r \left(\psi^{*,\theta}\right) r' \left(\phi^{*,\theta}\right) + \frac{1}{\rho_s} \left(r' \left(\phi^{*,\theta}\right) - r \left(\psi^{*,\theta}\right) r' \left(\phi^{*,\theta}\right)\right) - \frac{1}{\rho_g} r' \left(\phi^{*,\theta}\right)\right] \\ & - \left(p^{*,\theta} - p_0\right) \left[\frac{1}{\rho_l} \left(r \left(\psi^{*,\theta}\right) r'' \left(\phi^{*,\theta}\right) \cdot \theta\delta\phi + r' \left(\phi^{*,\theta}\right) r' \left(\psi^{*,\theta}\right) \cdot \theta\delta\psi\right)\right. \\ & \quad + \frac{1}{\rho_s} \left(r'' \left(\phi^{*,\theta}\right) \cdot \theta\delta\phi - r \left(\psi^{*,\theta}\right) r'' \left(\phi^{*,\theta}\right) \cdot \theta\delta\phi - r' \left(\phi^{*,\theta}\right) r' \left(\psi^{*,\theta}\right) \cdot \theta\delta\psi\right) \\ & \quad \left. - \frac{1}{\rho_g} r'' \left(\phi^{*,\theta}\right) \cdot \theta\delta\phi\right] \end{aligned} \tag{A.12}$$

(**Term** 6)

$$- \left(\frac{1}{\rho} \nabla \cdot \left(\rho \lambda_\phi \nabla\phi\right), \tilde{\mu_\phi}\right)$$

$$\begin{aligned} \left(\lambda_\phi \nabla\phi, \nabla\widetilde{\mu}_\phi\right) &= \left(\lambda_\phi \nabla \left(\phi^{*,\theta} + \theta\delta\phi\right), \nabla\widetilde{\mu}_\phi\right) \\ &= \left(\lambda_\phi \left(\nabla\phi^{*,\theta} + \theta\delta\nabla\phi\right), \nabla\widetilde{\mu}_\phi\right) \end{aligned} \tag{A.13}$$

$$\begin{aligned} \text{RHS} &= \lambda_\phi \nabla\phi^{*,\theta} \\ \text{MAT} &= -\lambda_\phi \theta\delta\nabla\phi \end{aligned} \tag{A.14}$$

$$\left(-\frac{1}{\rho} \nabla\rho\lambda_\phi \nabla\phi, \widetilde{\mu}_\phi\right) = \left(-\frac{1}{\rho^\theta} \nabla\rho^\theta \cdot \lambda_\phi \left(\nabla\phi^{*,\theta} + \theta\delta\nabla\phi\right), \widetilde{\mu}_\phi\right)$$

$$\text{RHS} = -\left(\frac{1}{\rho_l} r\left(\phi^{*,\theta}\right) r\left(\psi^{*,\theta}\right) + \frac{1}{\rho_s}\left(r\left(\phi^{*,\theta}\right) - r\left(\phi^{*,\theta}\right) r\left(\psi^{*,\theta}\right)\right) + \frac{1}{\rho_g}\left(1 - r\left(\phi^{*,\theta}\right)\right)\right) \cdot \nabla\rho^{*,\theta} \cdot \lambda_\phi \cdot \nabla\phi^{*,\theta} \tag{A.15}$$

$$\text{MAT} = \frac{1}{\rho^\theta}(\delta\phi, \delta\psi) \cdot \nabla\rho^{*,\theta} \cdot \lambda_\phi \cdot \nabla\phi^{*,\theta} + \frac{1}{\rho^{*,\theta}} \cdot \nabla\rho^\theta(\delta\phi, \delta\psi) \cdot \lambda_\phi \cdot \nabla\phi^{*,\theta} + \frac{1}{\rho^{*,\theta}} \cdot \nabla\rho^{*,\theta} \cdot \lambda_\phi \cdot \theta\delta\nabla\phi \tag{A.16}$$

$$\text{where } \frac{1}{p^\theta} = \frac{1}{\rho^{*,\theta}} + \frac{1}{\rho^\theta}(\delta\phi, \delta\psi)$$

$$\frac{1}{\rho^{*,\theta}} = \frac{1}{\rho_l} r\left(\phi^{*,\theta}\right) r\left(\psi^{*,\theta}\right) + \frac{1}{\rho_s}\left(r\left(\phi^{*,\theta}\right) - r\left(\phi^{*,\theta}\right) r\left(\psi^{*,\theta}\right) + \frac{1}{\rho_g}\left(1 - r\left(\phi^{*,\theta}\right)\right)\right)$$

$$\begin{aligned}\frac{1}{\rho^\theta}(\delta\phi, \delta\psi) =& \theta\delta\phi\left[\frac{1}{\rho_l} r\left(\psi^{*,\theta}\right) r'\left(\phi^{*,\theta}\right) + \frac{1}{\rho_s}\left(r'\left(\phi^{*,\theta}\right) - r\left(\psi^{*,\theta}\right) r'\left(\phi^{*,\theta}\right)\right) - \frac{1}{\rho_s} r'\left(\phi^{*,\theta}\right)\right] \\ &+ \theta\delta\psi\left[\frac{1}{\rho_l} r\left(\phi^{*,\theta}\right) r'\left(\psi^{*,\theta}\right) - \frac{1}{\rho_s} r\left(\phi^{*,\theta}\right) r'\left(\psi^{*,\theta}\right)\right]\end{aligned}$$

A.2 θ-scheme Chemical Potential for ψ

We want to derive the semi-discrete form for the equation (5.6):

$$\begin{aligned}\underbrace{(\mu_\psi, \tilde{\mu_\psi})}_{\textbf{Term7}} =& \underbrace{\left(\left[r'(\psi)r(\phi)L - \frac{\partial c}{\partial\psi} T_M\right]\left(1 - \frac{T}{T_M}\right), \tilde{\mu_\psi}\right)}_{\textbf{Term8}} - \underbrace{\left(\frac{\partial c}{\partial\psi} T \ln\frac{T}{T_M}, \tilde{\mu_\psi}\right)}_{\textbf{Term9}} \\ &+ \underbrace{(r(\phi)\lambda_\psi\omega'(\psi), \tilde{\mu_\psi})}_{\textbf{Term10}} - \underbrace{\left(\frac{p - p_0}{\rho^2}\frac{\partial\rho}{\partial\psi}, \tilde{\mu_\psi}\right)}_{\textbf{Term11}} \\ &- \underbrace{\left(\frac{1}{\rho}\nabla\cdot(\rho r(\phi)\lambda_\psi\nabla\psi), \tilde{\mu_\psi}\right)}_{\textbf{Term12}}\end{aligned}$$

(**Term** 7)

$$(\mu_\psi, \tilde{\mu_\psi})$$

$$\begin{aligned} \text{RHS} &= -\mu_\psi^{*,\theta} \\ \text{MAT} &= \delta\mu_\psi \end{aligned} \tag{A.17}$$

(**Term** 8)

$$\left(\left[r'(\psi) r(\phi) L - \frac{\partial c}{\partial \psi} T_M \right] \left(1 - \frac{T}{T_M} \right), \tilde{\mu_\psi} \right)$$

$$\text{RHS} = \left(L \cdot r' \left(\psi^{*,\theta} \right) \cdot r \left(\phi^{*,\theta} \right) - T_M \frac{\partial C^{*,\theta}}{\partial \psi} \right) \left(1 - \frac{T^{*,\theta}}{T_M} \right) \tag{A.18}$$

$$\begin{aligned} \text{MAT} = &\left(L \cdot r' \left(\psi^{*,\theta} \right) r \left(\phi^{*,\theta} \right) - T_M \frac{\partial C^{*,\theta}}{\partial \psi} \right) \frac{\theta \delta T}{T_M} \\ &- \left(L \left(r' \left(\psi^{*,\theta} \right) r' \left(\phi^{*,\theta} \right) \cdot \theta \delta\phi + r(\phi^{*,\theta}) \cdot r'' \left(\psi^{*,\theta} \right) \cdot \theta \delta\psi \right) - T_M \cdot C_\psi^{*,\theta}(\delta\phi, \delta\psi) \right) \cdot \left(1 - \frac{T^{*,\theta}}{T_M} \right) \end{aligned} \tag{A.19}$$

$$\text{where } \left. \frac{\partial C}{\partial \psi} \right|_\theta = \frac{\partial C^{*,\theta}}{\partial \psi} + C_\psi^{*,\theta}(\delta\phi, \delta\psi)$$

$$\frac{\partial C^{*,\theta}}{\partial \psi} = (C_l - C_s) \, r' \left(\psi^{*,\theta} \right) r \left(\phi^{*,\theta} \right)$$

$$C_\psi^{*,\theta} \left(\delta\phi, \delta\psi \right) = (C_l - C_s) \, r' \left(\psi^{*,\theta} \right) r' \left(\phi^{*,\theta} \right) \cdot \theta \delta\phi + (C_l - C_s) \, r \left(\phi^{*,\theta} \right) r'' \left(\psi^{*,\theta} \right) \cdot \theta \delta\psi$$

(**Term** 9)

$$- \left(\frac{\partial c}{\partial \psi} T \ln \frac{T}{T_M}, \tilde{\mu_\psi} \right)$$

$$\text{RHS} = -\left(C_l - C_s\right) r'\left(\psi^{*,\theta}\right) r\left(\phi^{*,\theta}\right) \cdot T^{*,\theta} \ln \frac{T^{*,\theta}}{T_M} \tag{A.20}$$

$$\text{MAT} = \frac{\partial C^{*,\theta}}{\partial \psi} \cdot \theta \delta T \left(\ln \frac{T^{*,\theta}}{T_M} + \frac{1}{T_M}\right) + C_\psi^{*,\theta}(\delta\phi, \delta\psi) \cdot T^{*,\theta} \ln \frac{T^{*,\theta}}{T_M} \tag{A.21}$$

(**Term** 10)

$$(r(\phi)\lambda_\psi \omega'(\psi), \tilde{\mu_\psi})$$

$$\text{RHS} = \lambda_\psi \cdot r\left(\phi^{*,\theta}\right) \omega'\left(\psi^{*,\theta}\right) \tag{A.22}$$

$$\text{MAT} = -\lambda_\psi r\left(\phi^{*,\theta}\right) \omega''\left(\psi^{*,\theta}\right) \cdot \theta\delta\psi - \lambda_\psi \omega'\left(\psi^{*,\theta}\right) r'\left(\phi^{*,\theta}\right) \cdot \theta\delta\phi \tag{A.23}$$

(**Term** 11)

$$-\left(\frac{p - p_0}{\rho^2} \frac{\partial \rho}{\partial \psi}, \tilde{\mu_\psi}\right)$$

$$\text{RHS} = \left(p^{*,\theta} + p_0\right) \left(\frac{1}{\rho_l} - \frac{1}{\rho_s}\right) r'\left(\psi^{*,\theta}\right) r\left(\phi^{*,\theta}\right) \tag{A.24}$$

$$\begin{aligned} \text{MAT} = &-\left(p^{*,\theta} + p_0\right) \left(\frac{1}{\rho_l} - \frac{1}{\rho_s}\right) \left[r'\left(\psi^{*,\theta}\right) r'\left(\phi^{*,\theta}\right) \cdot \theta\delta\phi + r\left(\phi^{*,\theta}\right) r''\left(\psi^{*,\theta}\right) \cdot \theta\delta\psi\right] \\ &- \delta p \left(\frac{1}{\rho_l} - \frac{1}{\rho_s}\right) r'\left(\psi^{*,\theta}\right) r\left(\phi^{*,\theta}\right) \end{aligned} \tag{A.25}$$

(**Term** 12)

$$-\left(\frac{1}{\rho} \nabla \cdot \left(\rho r(\phi) \lambda_\psi \nabla \psi\right), \tilde{\mu_\psi}\right)$$

$$\left(r(\phi)\lambda_\psi \nabla\psi, \nabla\widetilde{\mu}_\psi\right) = \left(\lambda_\psi \left(r\left(\phi^{*,\theta}\right) + r'\left(\phi^{*,\theta}\right) \cdot \theta\delta\phi\right) \cdot \left(\nabla\psi^{*,\theta} + \theta\delta\nabla\psi\right), \nabla\widetilde{\mu}_\phi\right)$$

$$\text{RHS} = \lambda_\psi r\left(\phi^{*,\theta}\right)\nabla\psi^{*,\theta} \tag{A.26}$$

$$\text{MAT} = -\lambda_\psi\left(r\left(\phi^{*,\theta}\right)\cdot\theta\delta\nabla\psi + \nabla\psi^{*,\theta}r'\left(\phi^{*,\theta}\right)\cdot\theta\delta\phi\right) \tag{A.27}$$

$$\left(-\frac{1}{\rho}\nabla p\cdot\left(\lambda_\psi r(\phi)\nabla\psi\right),\widetilde{\mu}_\psi\right)$$

$$\text{RHS} = -\frac{1}{\rho^{*,\theta}}\cdot\nabla\rho^{*,\theta}\cdot\lambda_\psi\cdot r\left(\phi^{*,\theta}\right)\cdot\nabla\psi^{*,\theta} \tag{A.28}$$

$$\begin{aligned}\text{MAT} =& \frac{1}{\rho^\theta}(\delta\phi,\delta\psi)\cdot\nabla\rho^{*,\theta}\cdot\lambda_\psi\cdot r\left(\phi^{*,\theta}\right)\cdot\nabla\psi^{*,\theta} + \frac{1}{\rho^{*,\theta}}\cdot\nabla\rho^\theta(\delta\phi,\delta\psi)\cdot\lambda_\psi\cdot r\left(\phi^{*,\theta}\right)\cdot\nabla\psi^{*,\theta}\\ &+\frac{1}{\rho^{*,\theta}}\cdot\nabla\rho^{*,\theta}\cdot\lambda_\psi\cdot r'\left(\phi^{*,\theta}\right)\cdot\theta\delta\phi\cdot\nabla\psi^{*,\theta}\\ &+\frac{1}{\rho^{*,\theta}}\cdot\nabla\rho^{*,\theta}\cdot\lambda_\psi\cdot r\left(\phi^{*,\theta}\right)\cdot\theta\delta\nabla\psi\end{aligned} \tag{A.29}$$

$$\text{where } \frac{1}{p^\theta} = \frac{1}{\rho^{*,\theta}} + \frac{1}{\rho^\theta}(\delta\phi,\delta\psi)$$

$$\frac{1}{\rho^{*,\theta}} = \frac{1}{\rho_l}r\left(\phi^{*,\theta}\right)r\left(\psi^{*,\theta}\right) + \frac{1}{\rho_s}\left(r\left(\phi^{*,\theta}\right) - r\left(\phi^{*,\theta}\right)r\left(\psi^{*,\theta}\right) + \frac{1}{\rho_g}\left(1 - r\left(\phi^{*,\theta}\right)\right)\right)$$

$$\begin{aligned}\frac{1}{\rho^\theta}(\delta\phi,\delta\psi) =& \theta\delta\phi\left[\frac{1}{\rho_l}r\left(\psi^{*,\theta}\right)r'\left(\phi^{*,\theta}\right) + \frac{1}{\rho_s}\left(r'\left(\phi^{*,\theta}\right) - r\left(\psi^{*,\theta}\right)r'\left(\phi^{*,\theta}\right)\right) - \frac{1}{\rho_s}r'\left(\phi^{*,\theta}\right)\right]\\ &+\theta\delta\psi\left[\frac{1}{\rho_l}r\left(\phi^{*,\theta}\right)r'\left(\psi^{*,\theta}\right) - \frac{1}{\rho_s}r\left(\phi^{*,\theta}\right)r'\left(\psi^{*,\theta}\right)\right]\end{aligned}$$

A.3 θ-scheme for Momentum Equation

We want to derive the semi-discrete form for the equation (5.1):

$$\begin{aligned}\underbrace{\left(\rho\left(\frac{\partial \mathbf{v}}{\partial t}+\mathbf{v}\cdot\nabla\mathbf{v}\right),\tilde{\mathbf{v}}\right)}_{\textbf{Term}13} =& \underbrace{-\left(-(p-p_0\mathbf{I})+\eta\left(\nabla\mathbf{v}+(\nabla\mathbf{v})^T-\frac{2}{3}(\nabla\cdot\mathbf{v})\mathbf{I}\right),\nabla\tilde{\mathbf{v}}\right)_\Omega}_{\textbf{Term}14}\\ &+\underbrace{\left(\rho\frac{\partial\hat{f}}{\partial\nabla\phi}\otimes\nabla\phi+\rho\frac{\partial\hat{f}}{\partial\nabla\psi}\otimes\nabla\psi,\nabla\tilde{\mathbf{v}}\right)_\Omega}_{\textbf{Term}15}\end{aligned} \tag{A.30}$$

(**Term** 13)

$$\left(\rho\frac{dv}{dt},\tilde{v}\right)$$

$$\text{RHS}=-\rho^{*,\theta}\left(\frac{V^*-V^n}{\Delta t}+V^{*,\theta}\cdot\nabla V^{*,\theta}\right) \tag{A.31}$$

$$\begin{aligned}\text{MAT}=&\left(\frac{\partial\rho^{*,\theta}}{\partial\phi}\theta\delta\phi+\frac{\partial\rho^{*,\theta}}{\partial\psi}\theta\delta\psi\right)\left(\frac{V^*-V^n}{\Delta t}+V^{*,\theta}\cdot\nabla V^{*,\theta}\right)\\ &+\rho^{*,\theta}\left(\frac{\delta V}{\Delta t}+V^{*,\theta}\cdot\theta\delta\nabla V+\theta\delta V\cdot\nabla V^{*,\theta}\right)\end{aligned} \tag{A.32}$$

(**Term** 14)

$$\left(\nabla\cdot\left[-\left(p-p_0\right)I+\mu(\nabla v+\nabla v^T-\frac{2}{3}\nabla\cdot I)\right],\tilde{v}\right)$$

$$\text{RHS}=\left(p^{*,\theta}-p_0\right)I-\mu^{*,\theta}\left(\nabla V^{*,\theta}+\left(\nabla V^{*,\theta}\right)^\top-\frac{2}{3}\nabla V^{*,\theta}I\right) \tag{A.33}$$

$$\begin{aligned}\text{MAT}=&-\theta\delta pI+\mu^{*,\theta}\left(\theta\delta\nabla V+\theta\delta(\nabla V)^\top-\frac{2}{3}\theta\nabla\cdot\delta VI\right)\\ &+\left(\frac{\partial\mu^{*,\theta}}{\partial\phi}\cdot\theta\delta\phi+\frac{\partial\mu^{*,\theta}}{\partial\psi}\cdot\theta\delta\psi\right)\cdot\left(\nabla V^{*,\theta}+\left(\nabla V^{*,\theta}\right)^\top-\frac{2}{3}\nabla V^{*,\theta}I\right)\end{aligned} \tag{A.34}$$

(**Term** 15)

$$\left(\nabla\cdot\left[-\rho\frac{\partial\hat{f}}{\partial\nabla\phi}\otimes\nabla\phi-\rho\frac{\partial\hat{f}}{\partial\nabla\psi}\otimes\nabla\psi\right],\tilde{v}\right)$$

$$\text{RHS}=\rho^{*,\theta}\left(\lambda_\phi\nabla\phi^{*,\theta}\otimes\nabla\phi^{*,\theta}+\lambda_\psi r\left(\phi^{*,\theta}\right)\nabla\psi^{*,\theta}\otimes\nabla\psi^{*,\theta}\right) \tag{A.35}$$

$$\begin{aligned}\text{MAT} = -\Bigg(&\left(\frac{\partial \rho^{*,\theta}}{\partial \phi}\theta\delta\phi + \frac{\partial \rho^{*,\theta}}{\partial \psi}\theta\delta\psi\right)\cdot\left(\lambda_\phi \nabla\phi^{*,\theta}\otimes\nabla\phi^{*,\theta} + \lambda_\psi r\left(\phi^{*,\theta}\right)\nabla\psi^{*,\theta}\otimes\nabla\psi^{*,\theta}\right)\\ &+\rho^{*,\theta}\Bigg[\lambda_\phi\left(\nabla\phi^{*,\theta}\otimes\theta\delta\nabla\phi + \theta\delta\nabla\phi\otimes\nabla\phi^{*,\theta}\right)\\ &+\lambda_\psi\Bigg(r\left(\phi^{*,\theta}\right)\nabla\psi^{*,\theta}\otimes\nabla\psi^{*,\theta} + r\left(\phi^{*,\theta}\right)\theta\delta\nabla\psi\otimes\nabla\psi^{*,\theta} + r'\left(\phi^{*,\theta}\right)\theta\delta\phi\cdot\nabla\psi^{*,\theta}\otimes\nabla\psi^{*,\theta}\Bigg)\Bigg]\end{aligned} \tag{A.36}$$

A.4 θ-scheme for Continuity Equation

We want to derive the semi-discrete form for equation (5.2):

$$\underbrace{(\nabla\cdot v,\tilde{p})}_{\textbf{Term}16} = \underbrace{-\left(\frac{1}{\rho}\left(\frac{\partial\rho}{D\phi}\frac{d\phi}{dt}+\frac{\partial\rho}{D\psi}\frac{d\psi}{dt}\right),\tilde{p}\right)}_{\textbf{Term}17} \tag{A.37}$$

(**Term** 16)

$$\begin{aligned}(\nabla\cdot v,\tilde{p})&\\ \text{RHS} &= -\nabla V^{*,\theta}\\ \text{MAT} &= \nabla\cdot\theta\delta V\end{aligned} \tag{A.38}$$

(**Term** 17)

$$-\left(\frac{1}{\rho}\left(\frac{\partial\rho}{\partial\phi}\frac{d\phi}{dt}+\frac{\partial\rho}{\partial\psi}\frac{d\psi}{dt}\right),\tilde{p}\right)$$

$$\begin{aligned}\text{RHS} = &\frac{1}{\rho_l}r\left(\psi^{*,\theta}\right)r'\left(\phi^{*,\theta}\right)\cdot\nabla M_\phi\mu_\phi^{*,\theta} + \frac{1}{\rho_s}\left(r'\left(\phi^{*,\theta}\right) - r\left(\psi^{*,\theta}\right)r'\left(\phi^{*,\theta}\right)\right)\cdot\nabla M_\phi\mu_\phi^{*,\theta}\Bigg)\\ &-\frac{1}{\rho_g}r'\left(\phi^{*,\theta}\right)\cdot\nabla M_\phi\mu_\phi^{*,\theta} + \left(\frac{1}{\rho_l}-\frac{1}{\rho_s}\right)r'\left(\psi^{*,\theta}\right)r\left(\phi^{*,\theta}\right)\cdot M_\psi\mu_\psi^{*,\theta}\end{aligned} \tag{A.39}$$

$$
\begin{aligned}
\mathrm{MAT} = & -\theta\delta\phi\left[\frac{1}{\rho_l} r\left(\psi^{*,\theta}\right) r''\left(\phi^{*,\theta}\right)\cdot\nabla M_\phi \mu_\phi^{*,\theta} + \frac{1}{\rho_s}\cdot\nabla M_\phi \mu_\phi^{*,\theta}\left(r''\left(\phi^{*,\theta}\right) - r\left(\psi^{*,\theta}\right) r''\left(\phi^{*,\theta}\right)\right)\right. \\
& \qquad \left. -\frac{1}{\rho_g}\cdot\nabla M_\phi \mu_\phi^{*,\theta} r''\left(\phi^{*,\theta}\right) + \left(\frac{1}{\rho_l}-\frac{1}{\rho_s}\right) M_\psi \mu_\psi^{*,\theta} r'\left(\psi^{*,\theta}\right) r'\left(\phi^{*,\theta}\right)\right] \\
& -\theta\delta\psi\left[\frac{1}{\rho_l} r'\left(\phi^{*,\theta}\right)\cdot r'\left(\psi^{*,\theta}\right)\cdot\nabla M_\phi \mu_\phi^{*,\theta} - \frac{1}{\rho_s}\cdot\nabla M_\phi \mu_\phi^{*,\theta} r'\left(\phi^{*,\theta}\right) r'\left(\psi^{*,\theta}\right)\right. \\
& \qquad \left. + \left(\frac{1}{\rho_l}-\frac{1}{\rho_s}\right) M_\psi \mu_\psi^{*,\theta} r'\left(\phi^{*,\theta}\right) r''\left(\psi^{*,\theta}\right)\right] \\
& -\nabla M_\phi \theta\delta\mu_\phi\left[\frac{1}{\rho_l} r\left(\psi^{*,\theta}\right) r'\left(\phi^{*,\theta}\right) + \frac{1}{\rho_g}\left(r'\left(\phi^{*,\theta}\right) - r\left(\psi^{*,\theta}\right) r'\left(\phi^{*,\theta}\right)\right) - \frac{1}{\rho_g} r'\left(\phi^{*,\theta}\right)\right] \\
& -M_\psi\delta\mu_\psi\left[\left(\frac{1}{\rho_l}-\frac{1}{\rho_s}\right) r'\left(\psi^{*,\theta}\right) r\left(\phi^{*,\theta}\right)\right]
\end{aligned}
\tag{A.40}
$$

Alternative form as following:

$$
-\left(\frac{1}{\rho}\left(\frac{\partial\rho}{\partial\phi}\frac{d\phi}{dt} + \frac{\partial\rho}{\partial\psi}\frac{d\psi}{dt}\right), \tilde{p}\right)
$$

$$
\begin{aligned}
\mathrm{RHS} = & \frac{1}{\rho_l} r\left(\psi^{*,\theta}\right) r'\left(\phi^{*,\theta}\right)\cdot H^{*,\theta} + \frac{1}{\rho_s}\left(r'\left(\phi^{*,\theta}\right) - r\left(\psi^{*,\theta}\right) r'\left(\phi^{*,\theta}\right)\right)\cdot H^{*,\theta}\Big) \\
& -\frac{1}{\rho_g} r'\left(\phi^{*,\theta}\right)\cdot H^{*,\theta} + \left(\frac{1}{\rho_l}-\frac{1}{\rho_s}\right) r'\left(\psi^{*,\theta}\right) r\left(\phi^{*,\theta}\right)\cdot M_\psi \mu_\psi^{*,\theta}
\end{aligned}
\tag{A.41}
$$

$$
\begin{aligned}
\mathrm{MAT} = & -\theta\delta\phi\left[\frac{1}{\rho_l} r\left(\psi^{*,\theta}\right) r''\left(\phi^{*,\theta}\right)\cdot H^{*,\theta} + \frac{1}{\rho_s}\cdot H^{*,\theta}\left(r''\left(\phi^{*,\theta}\right) - r\left(\psi^{*,\theta}\right) r''\left(\phi^{*,\theta}\right)\right)\right. \\
& \qquad \left. -\frac{1}{\rho_g}\cdot H^{*,\theta} r''\left(\phi^{*,\theta}\right) + \left(\frac{1}{\rho_l}-\frac{1}{\rho_s}\right) M_\psi \mu_\psi^{*,\theta} r'\left(\psi^{*,\theta}\right) r'\left(\phi^{*,\theta}\right)\right] \\
& -\theta\delta\psi\left[\frac{1}{\rho_l} r'\left(\phi^{*,\theta}\right)\cdot r'\left(\psi^{*,\theta}\right)\cdot H^{*,\theta} - \frac{1}{\rho_s}\cdot H^{*,\theta} r'\left(\phi^{*,\theta}\right) r'\left(\psi^{*,\theta}\right)\right. \\
& \qquad \left. + \left(\frac{1}{\rho_l}-\frac{1}{\rho_s}\right) M_\psi \mu_\psi^{*,\theta} r'\left(\phi^{*,\theta}\right) r''\left(\psi^{*,\theta}\right)\right] \\
& -\delta H\left[\frac{1}{\rho_l} r\left(\psi^{*,\theta}\right) r'\left(\phi^{*,\theta}\right) + \frac{1}{\rho_g}\left(r'\left(\phi^{*,\theta}\right) - r\left(\psi^{*,\theta}\right) r'\left(\phi^{*,\theta}\right)\right) - \frac{1}{\rho_g} r'\left(\phi^{*,\theta}\right)\right] \\
& -M_\psi\delta\mu_\psi\left[\left(\frac{1}{\rho_l}-\frac{1}{\rho_s}\right) r'\left(\psi^{*,\theta}\right) r\left(\phi^{*,\theta}\right)\right]
\end{aligned}
\tag{A.42}
$$

A.5 θ-scheme for Internal Energy Equation

We want to derive the semi-discrete form for equation (5.7):

$$\underbrace{\left(\rho c\frac{dT}{dt},\tilde{T}\right)}_{\textbf{Term}18}=\underbrace{\left(M_\phi\left|\nabla\mu_\phi\right|^2,\tilde{T}\right)+\left(M_\psi\left|\mu_\psi\right|^2,\tilde{T}\right)}_{\textbf{Term}19}+\underbrace{\left(\eta\left(\nabla v+\nabla v^\top-\frac{2}{3}\nabla\cdot v\ I\right):\nabla v,\tilde{T}\right)}_{\textbf{Term}20}$$
$$+\underbrace{\left(\nabla\cdot(k\nabla T),\tilde{T}\right)}_{\textbf{Term}21}-\underbrace{\left(\rho L\left(r(\psi)r'(\phi)\frac{d\phi}{dt}+r'(\psi)r(\phi)\frac{d\psi}{dt}\right)\frac{T}{T_M},\tilde{T}\right)}_{\textbf{Term}22}$$
$$-\underbrace{\left(\rho\left(\frac{\partial c}{\partial\phi}\frac{d\phi}{dt}+\frac{\partial c}{\partial\psi}\frac{d\psi}{dt}\right)T\ln\frac{T}{T_M},\tilde{T}\right)}_{\textbf{Term}23}$$

(**Term** 18) Let

$$\frac{dT}{dt}=\frac{\partial T}{\partial t}+V^\theta\cdot\nabla T^\theta$$

$$\begin{aligned}\frac{\partial T}{\partial t}&=\frac{T^*+\delta T-T^h}{\Delta t}\\ V^\theta&=V^{*,\theta}+\theta\delta V\\ \nabla T^\theta&=\nabla T^{*,\theta}+\theta\delta\nabla T\\ \phi^\theta&=\phi^{*,\theta}+\theta\delta\phi\\ \psi^\theta&=\psi^{*,\theta}+\theta\delta\psi\end{aligned}$$

First term:

$$\begin{aligned}\rho\left(\phi^*,\psi^*\right)&=\rho\left(\phi^{*,\theta}+\theta\delta\phi,\psi^{*,\theta}+\theta\delta\psi\right)\\ &\approx\rho\left(\phi^{*,\theta},\psi^{*,\theta}\right)+\left.\frac{\partial\rho}{\partial\phi}\right|_{\phi^{*,\theta}}\theta\delta\phi+\left.\frac{\partial\rho}{\partial\psi}\right|_{\psi^{*,\theta}}\theta\delta\psi.\\ &=\rho^{*,\theta}+\frac{\partial\rho^{*,\theta}}{\partial\phi}\cdot\theta\delta\phi+\frac{\partial\rho^{*,\theta}}{\partial\psi}\theta\delta\psi\end{aligned}$$

2^{nd} term:

$$\begin{aligned} C\left(\phi^*,\psi^*\right) &= C\left(\phi^{*,\theta}+\theta\delta\phi,\psi^{*,\theta}+\theta\delta\psi\right) \\ &= C^{*,\theta}+\frac{\partial C^{*,\theta}}{\partial\phi}\cdot\theta\delta\phi+\frac{\partial C^{*,\theta}}{\partial\psi}\theta\delta\psi \end{aligned}$$

3^{nd} term:

$$\begin{aligned} \frac{dT}{dt} =& \frac{I^*+\delta T-T^n}{\Delta t}+\left(V^{*,\theta}+\theta\delta V\right)\left(\nabla T^{*,\theta}+\theta\delta\nabla T\right) \\ =& \frac{T^*-T^n}{\Delta t}+\frac{\delta T}{\Delta t}+V^{*,\theta}\nabla T^{*,\theta}+V^{*,\theta}\cdot\theta\nabla\delta T+\theta\delta V\nabla T^{*,\theta} \end{aligned}$$

$$\begin{aligned} &\left(\rho\left(\phi^\theta,\psi^\theta\right)C\left(\phi^\theta,\psi^\theta\right)\left(\frac{\partial T}{\partial t}+V^\theta\cdot\nabla T^\theta\right),\widetilde{T}\right) \\ &= \left(\left(\rho^*,\theta+\frac{\partial\rho^{*,\theta}}{\partial\phi}\cdot\theta\delta\phi+\frac{\partial\rho^{*,\theta}}{\partial\psi}\theta\delta\psi\right)\cdot\left(C^{*,\theta}+\frac{\partial C^{*,\theta}}{\partial\phi}\cdot\theta\delta\phi+\frac{\partial C^{*,\theta}}{\partial\psi}\theta\delta\psi\right)\right. \\ &\quad\left.\cdot\left(\frac{T^*-T^n}{\Delta t}+\frac{\delta T}{\Delta t}+V^{*,\theta}\nabla T^{*,\theta}+V^{*,\theta}\cdot\theta\nabla\delta T+\theta\delta V\nabla T^{*,\theta}\right),\quad\widetilde{T}\right) \\ &= \left(\rho^{*,\theta}\cdot C^{*,\theta}\cdot\frac{T^*-T^n}{\Delta t}+\rho^{*,\theta}\cdot C^{*,\theta}\cdot\frac{\delta T}{\Delta t}+\rho^{*,\theta}\cdot C^{*,\theta}\cdot V^{*,\theta}\nabla T^{*,\theta}+\rho^{*,\theta}C^{*,\theta}\cdot\theta\left(V^{*,\theta}\nabla\delta T+\delta V\nabla T^{*,\theta}\right)\right. \\ &\quad+\rho^{*,\theta}\frac{\partial C^{*,\theta}}{\partial\phi}\cdot\theta\delta\phi\left(\frac{T^*-T^n}{\Delta_t}+V^{*,\theta}\nabla T^{*,\theta}\right)+\rho^{*,\theta}\frac{\partial C^{*,\theta}}{\partial\psi}\theta\delta_\psi\left(\frac{T^*-T_n}{\Delta t}+V^{*,\theta}\cdot\nabla T^{*,\theta}\right) \\ &\quad\left.+C^{*,\theta}\frac{\partial\rho^{*,\theta}}{\partial\phi}\theta\delta\phi\left(\frac{T^*-T^n}{\Delta t}+V^{*,\theta}\nabla T^{*,\theta}\right)+C^{*,\theta}\frac{\partial\rho^{*,\theta}}{\partial\psi}\theta\delta\psi\left(\frac{T^*-T_n}{\Delta t}+V^{*,\theta}\cdot\nabla T^{*,\theta}\right),\widetilde{T}\right) \end{aligned}$$

So that

$$\begin{aligned} &\left(\rho\left(\phi^\theta,\psi^\theta\right)C\left(\phi^\theta,\psi^\theta\right)\left(\frac{\partial T}{\partial t}+V^\theta\cdot\nabla T^\theta\right),\widetilde{T}\right)= \\ &(\rho^{*,\theta}c^{*,\theta}\left(\frac{T^*-T_n}{\Delta t}+V^{*,\theta}\cdot\nabla T^{*,\theta}\right)+\rho^{*,\theta}c^{*,\theta}\left[\frac{\delta T}{\Delta t}+\theta\left(V^{*,\theta}\cdot\nabla\delta T+\delta V\cdot\nabla T^{*,\theta}\right)\right] \\ &+\left[\left(\rho^{*,\theta}\frac{\partial c^{*,\theta}}{\partial\phi}+c^{*,\theta}\frac{\partial\rho^{*,\theta}}{\partial\phi}\right)\theta\delta\phi\right. \\ &\left.+\left(\rho^{*,\theta}\frac{\partial c^{*,\theta}}{\partial\psi}+c^{*,\theta}\frac{\partial\rho^{*,\theta}}{\partial\psi}\right)\theta\delta\psi\right]\left(\frac{T^*-T_n}{\Delta t}+V^{*,\theta}\cdot\Delta T^{*,\theta}\right),\widetilde{T}) \end{aligned}$$

$$\text{RHS} = -\rho^{*,\theta} c^{*,\theta} \left(\frac{T^* - T_n}{\Delta t} + V^{*,\theta} \cdot \nabla T^{*,\theta} \right) \tag{A.43}$$

$$\begin{aligned} \text{MAT} = & \rho^{*,\theta} c^{*,\theta} \left[\frac{\delta T}{\Delta t} + \theta \left(V^{*,\theta} \cdot \nabla \delta T + \delta V \cdot \nabla T^{*,\theta} \right) \right] \\ & + \left[\left(\rho^{*,\theta} \frac{\partial c^{*,\theta}}{\partial \phi} + c^{*,\theta} \frac{\partial \rho^{*,\theta}}{\partial \phi} \right) \theta \delta \phi \right. \\ & \left. + \left(\rho^{*,\theta} \frac{\partial c^{*,\theta}}{\partial \psi} + c^{*,\theta} \frac{\partial \rho^{*,\theta}}{\partial \psi} \right) \theta \delta \psi \right] \left(\frac{T^* - T_n}{\Delta t} + V^{*,\theta} \cdot \Delta T^{*,\theta} \right) \end{aligned} \tag{A.44}$$

(**Term** 19) Let

$$\mu_\phi^\theta = \mu_\phi^{*,\theta} + \delta \mu_\phi$$

$$\begin{aligned} |\nabla \mu_\phi^\theta|^2 = & |\nabla \left(\mu_\phi^{*,\theta} + \delta \mu_\phi \right)|^2 \\ = & |\nabla \mu_\phi^{*,\theta}|^2 + 2 \nabla \mu_\phi^{*,\theta} \cdot \nabla \delta \mu_\phi \end{aligned}$$

$$\left(M_\phi \left| \nabla \mu_\phi \right|^2, \tilde{T} \right) + \left(M_\psi \left| \mu_\psi \right|^2, \tilde{T} \right)$$

$$\text{RHS} = M_\phi \left| \nabla \mu_\phi^{*,\theta} \right|^2 + M_\psi \left| \mu_\psi^{*,\theta} \right|^2 \tag{A.45}$$

$$\text{MAT} \ = - \left(2 M_\phi \nabla \mu_\phi^{*,\theta} \cdot \nabla \delta \mu_\phi + 2 M_\psi \theta \mu_\psi^{*,\theta} \delta \mu_\psi \right) \tag{A.46}$$

(**Term** 20)

$$\left(\eta \left(\nabla v + \nabla v^\top - \frac{2}{3} \nabla \cdot v \ I \right) : \nabla v, \tilde{T} \right)$$

$$\text{RHS} = \eta^{*,\theta} \left[\nabla V^{*,\theta} + \left(\nabla V^{*,\theta} \right)^\top - \frac{2}{3} \nabla V^{*,\theta} I \right] : \nabla V^{*,\theta} \tag{A.47}$$

$$\begin{aligned}\text{MAT} =&\theta\eta^{*,\theta}\left[\left(\nabla V^{*,\theta}+\left(\nabla V^{*,\theta}\right)^{\top}-\frac{1}{3}\nabla V^{*,\theta}I\right):\delta\nabla V+\left(\nabla\delta V+(\nabla\delta V)^{\top}-\frac{2}{3}\nabla\cdot\delta V I\right):\nabla V^{*,\theta}\right]\\&+\left(\frac{\partial\eta^{*,\theta}}{\partial\phi}\cdot\delta\phi+\frac{\partial\eta^{*,\theta}}{\partial\psi}\cdot\delta\psi\right)\cdot\left[\nabla V^{*,\theta}+\left(\nabla V^{*,\theta}\right)^{\top}-\frac{2}{3}\nabla V^{*,\theta}I\right]:\nabla V^{*,\theta}\end{aligned} \tag{A.48}$$

(**Term** 21)

$$\left(\nabla\cdot(k\nabla T),\tilde{T}\right)=-(k\nabla T,\nabla\tilde{T})_{\Omega}+(n\cdot(k\nabla T),\tilde{T})_{\partial\Omega}$$

$$\text{RHS}=-k\nabla T^{*,\theta} \tag{A.49}$$

$$\text{MAT}=k\theta\nabla\delta T \tag{A.50}$$

(**Term** 22)

$$-\left(\rho L\left(r(\psi)r'(\phi)\frac{d\phi}{dt}+r'(\psi)r(\phi)\frac{d\psi}{dt}\right)\frac{T}{T_M},\tilde{T}\right)$$

$$\begin{aligned}\text{RHS}=&-\rho^{*,\theta}r\left(\psi^{*,\theta}\right)r'\left(\phi^{*,\theta}\right)\cdot\frac{T^{*,\theta}}{T_M}\cdot L\cdot\frac{\phi^{*}-\phi^{n}}{\Delta t}\\&-\rho^{*,\theta}r'\left(\psi^{*,\theta}\right)r\left(\phi^{*,\theta}\right)\cdot\frac{T^{*,\theta}}{T_M}\cdot L\cdot\frac{\psi^{*}-\psi^{n}}{\Delta t}\end{aligned} \tag{A.51}$$

$$\begin{aligned}\mathrm{MAT} =&\Bigg[\rho^{*,\theta} r\left(\psi^{*,\theta}\right) r'\left(\phi^{*,\theta}\right)\cdot\frac{\delta T}{T_M}+\Bigg[\rho^{*,\theta} r\left(\psi^{*,\theta}\right)\cdot r''\left(\phi^{*,\theta}\right)\cdot\theta\delta\phi\\&+\rho^{*,\theta} r'\left(\phi^{*,\theta}\right)\cdot r'\left(\psi^{*,\theta}\right)\cdot\theta\delta\psi+r\left(\psi^{*,\theta}\right) r'\left(\phi^{*,\theta}\right)\cdot\frac{\partial\rho^{*,\theta}}{\partial\phi}\cdot\theta\delta\phi\\&+r\left(\psi^{*,\theta}\right) r'\left(\phi^{*,\theta}\right)\cdot\frac{\partial\rho^{*,\theta}}{\partial\psi}\cdot\theta\delta\psi\Bigg]\cdot\frac{T^{*,\theta}}{T_M}\Bigg]\cdot L\cdot\frac{\phi^*-\phi^n}{\Delta t}\\&+\Bigg[\rho^{*,\theta} r'\left(\psi^{*,\theta}\right) r\left(\phi^{*,\theta}\right)\cdot\frac{\delta T}{T_M}+\Bigg[\rho^{*,\theta} r'\left(\psi^{*,\theta}\right) r'\left(\phi^{*,\theta}\right)\theta\delta\phi\\&+\rho^{*,\theta} r\left(\phi^{*,\theta}\right) r''\left(\psi^{*,\theta}\right)\cdot\theta\delta\psi+r'\left(\psi^{*,\theta}\right) r\left(\phi^{*,\theta}\right)\cdot\frac{\partial\rho^{*,\theta}}{\partial\phi}\cdot\theta\delta\phi\\&+r'\left(\psi^{*,\theta}\right) r\left(\phi^{*,\theta}\right)\cdot\frac{\partial\rho^{*,\theta}}{\partial\psi}\cdot\theta\delta\psi\Bigg]\cdot\frac{T^{*,\theta}}{T_M}\Bigg]\cdot L\cdot\frac{\psi^*-\psi^n}{\Delta t}\end{aligned}\tag{A.52}$$

(**Term** 23)

$$-\left(\rho\left(\frac{\partial c}{\partial\phi}\frac{d\phi}{dt}+\frac{\partial c}{\partial\psi}\frac{d\psi}{dt}\right)T\ln\frac{T}{T_M},\tilde{T}\right)$$

$$\mathrm{RHS}=-\rho^{*,\theta}\cdot\nabla M_\phi\mu_\phi^{*,\theta}\cdot T^{*,\theta}\ln\frac{T^{*,\theta}}{T_M}\cdot C_2^1-\rho^{*,\theta}\cdot M_\psi\mu_\psi^{*,\theta}T^{*,\theta}\ln\frac{T^{*,\theta}}{T_M}\cdot C_3^1\tag{A.53}$$

$$\begin{aligned}\mathrm{MAT} =&\theta\delta\phi\left[\frac{\partial\rho^{*,\theta}}{\partial\phi}\cdot C_2^1\cdot\nabla M_\phi\mu_\phi^{*,\theta}\cdot T^{*,\theta}\ln\frac{T^{*,\theta}}{T_M}+\rho^{*,\theta}\cdot C_2^3\cdot\nabla M_\phi\mu_\phi^{*,\theta}\cdot T^{*,\theta}\ln\frac{T^{*,\theta}}{T_M}\right.\\&\left.+\frac{\partial\rho^{*,\theta}}{\partial\phi}\cdot C_3^1\cdot M_\psi\mu_\psi^{*,\theta}\cdot T^{*,\theta}\ln\frac{T^{*,\theta}}{T_M}+\rho^{*,\theta}C_3^3M_\psi\mu_\psi^{*,\theta}\cdot T^{*,\theta}\ln\frac{T^{*,\theta}}{T_M}\right]\\&+\theta\delta\psi\left[\frac{\partial\rho^{*,\theta}}{\partial\psi}\cdot C_2^1\cdot\nabla M_\phi\mu_\phi^{*,\theta}\cdot T^{*,\theta}\ln\frac{T^{*,\theta}}{T_M}+\rho^{*,\theta}C_2^2\nabla M_\phi\mu_\phi^{*,\theta}\cdot T^{*,\theta}\ln\frac{T^{*,\theta}}{T_M}\right.\\&\left.+\frac{\partial\rho^{*,\theta}}{\partial\psi}\cdot C_3^1\cdot M_\psi\mu_\psi^{*,\theta}\cdot T^{*,\theta}\ln\frac{T^{*,\theta}}{T_M}+\rho^{*,\theta}\cdot C_3^2\ M_\psi\mu_\psi^{*,\theta}\cdot T^{*,\theta}\ln\frac{T^{*,\theta}}{T_M}\right]\\&+\rho^{*,\theta}\cdot C_2^1\nabla M_\phi\theta\delta\mu_\phi\cdot T^{*,\theta}\cdot\ln\frac{T^{*,\theta}}{T_M}+\rho^{*,\theta}C_3^1\cdot M_\psi\theta\delta\mu_\psi\cdot T^{*,\theta}\ln\frac{T^{*,\theta}}{T_M}\\&+\theta\delta T\ln\frac{T^{*,\theta}}{T_M}\left[\rho^{*,\theta}\cdot C_2^1\cdot\nabla M_\phi\mu_\phi^{*,\theta}+\rho^{*,\theta}\cdot C_3^1M_\psi\mu_\psi^{*,\theta}\right]\\&+\theta\delta T\left[\rho^{*,\theta}C_2^1\nabla M_\phi\mu_\phi^{*,\theta}+\rho^{*,\theta}C_3^1M_\psi\mu_\psi^{*,\theta}\right]\end{aligned}\tag{A.54}$$

$$\text{where } C_2^1 = \frac{\partial c}{\partial \phi} = C_l r'\left(\phi^{*,\theta}\right) r\left(\psi^{*,\theta}\right) + C_s r'\left(\phi^{*,\theta}\right) - C_s r'\left(\phi^{*,\theta}\right) r\left(\psi^{*,\theta}\right) - C_g r'\left(\phi^{*,\theta}\right)$$

$$C_2^2 = \frac{\partial}{\partial \psi}\left(\frac{\partial c}{\partial \phi}\right) = C_l r'\left(\phi^{*,\theta}\right) r'\left(\psi^{*,\theta}\right) - C_s r'\left(\phi^{*,\theta}\right) r'\left(\psi^{*,\theta}\right)$$

$$C_2^3 = \frac{\partial}{\partial \phi}\left(\frac{\partial c}{\partial \phi}\right) = C_l r\left(\psi^{*,\theta}\right) r''\left(\phi^{*,\theta}\right) + C_s r''\left(\phi^{*,\theta}\right) - C_s r\left(\psi^{*,\theta}\right) r''\left(\phi^{*,\theta}\right) - C_g r''\left(\phi^{*,\theta}\right)$$

$$C_3^1 = \frac{\partial c}{\partial \psi} = \left(C_l - C_s\right) \cdot r'\left(\psi^{*,\theta}\right) r\left(\phi^{*,\theta}\right)$$

$$C_3^2 = \frac{\partial}{\partial \psi}\left(\frac{\partial c}{\partial \psi}\right) = \left(C_l - C_s\right) r\left(\phi^{*,\theta}\right) r''\left(\psi^{*,\theta}\right)$$

$$C_3^3 = \frac{\partial}{\partial \phi}\left(\frac{\partial c}{\partial \psi}\right) = \left(C_l - C_s\right) r'\left(\psi^{*,\theta}\right) r'\left(\phi^{*,\theta}\right)$$

Alternative form as following:

We have:

$$\left(\rho \frac{d\phi}{dt}\right)^{n+\theta} = H$$

$$H^\theta = H^{*,\theta} + \delta H$$

$$H = \nabla \cdot \left(M_\phi \nabla \mu_\phi\right)$$

$$c(\phi, \psi) = C_l r(\phi) r(\psi) + C_s r(\phi)(1 - r(\psi)) + C_g(1 - r(\phi))$$

$$\frac{\partial c}{\partial \phi} = \left[C_l r(\psi) + C_s(1 - r(\psi)) - c_g\right] r'(\phi)$$

$$\frac{\partial c}{\partial \psi} = \left(C_l - C_s\right) r'(\psi) r(\phi)$$

$$-\left(\rho\left(\frac{\partial c}{\partial \phi}\frac{d\phi}{dt} + \frac{\partial c}{\partial \psi}\frac{d\psi}{dt}\right) T \ln\frac{T}{T_M}, \tilde{T}\right)$$

$$\text{RHS} = \left[-C_2^1 H^{*,\theta} + C_3^1 M_\psi \mu_\psi^{*,\theta}\right] \cdot T^{*,\theta} \ln\frac{T^{*,\theta}}{T_M} \tag{A.55}$$

$$\begin{aligned}\mathrm{MAT} =&[(C_2^2\theta\delta\psi + C_2^3\theta\delta\phi)H^{*,\theta} - (C_3^2\theta\delta\psi + C_3^3\theta\delta\phi)M_\psi\mu_\psi^{*,\theta}] \cdot T^{*,\theta}\ln\frac{T^{*,\theta}}{T_M} \\ &+ (C_2^1\delta H - C_3^1 M_\psi\delta\mu_\psi \cdot T^{*,\theta}\ln\frac{T^{*,\theta}}{T_M} \\ &+ (C_2^1 H^{*,\theta} - C_3^1 M_\psi\mu_\psi^{*,\theta}) \cdot (\theta\delta T\ln\frac{T^{*,\theta}}{T_M} + \theta\delta T)\end{aligned} \tag{A.56}$$

Appendix B

Second Appendix

B.1 Derivation of the Full Chemical Potential Expressions

We derive the explicit forms of μ_ϕ and μ_ψ by performing functional differentiation of the total free energy $\mathcal{F}$ in Eq. (4.1), using the free energy density defined in Eq. (4.2):

$$f(\phi,\psi;\nabla\phi,\nabla\psi) = \lambda_\phi\Big(W(\phi)+\frac{1}{2}|\nabla\phi|^2\Big) + r(\phi)\Big[\lambda_\psi\Big(W(\psi)+\frac{1}{2}|\nabla\psi|^2\Big) + r(\psi)\,L\Big(1-\frac{T}{T_m}\Big)\Big].$$

To justify the variational expressions of the chemical potentials, we briefly recall how the functional derivatives of $\mathcal{F}$ are obtained. Let η_ϕ and η_ψ be smooth test functions. We consider the first variation of $\mathcal{F}$ in the direction (η_ϕ,η_ψ):

$$\delta\mathcal{F} = \frac{d}{d\varepsilon}\mathcal{F}\big[\phi+\varepsilon\eta_\phi,\ \psi+\varepsilon\eta_\psi\big]\Big|_{\varepsilon=0}.$$

Using Eq. (4.1), we write

$$\mathcal{F}\big[\phi+\varepsilon\eta_\phi,\,\psi+\varepsilon\eta_\psi\big]=\int_\Omega f\Big(\phi+\varepsilon\eta_\phi,\,\psi+\varepsilon\eta_\psi;\nabla\phi+\varepsilon\nabla\eta_\phi,\,\nabla\psi+\varepsilon\nabla\eta_\psi\Big)\,d\Omega.$$

Differentiating with respect to ε and evaluating at $\varepsilon=0$, we obtain

$$\delta\mathcal{F}=\int_\Omega \frac{d}{d\varepsilon}f\Big(\phi+\varepsilon\eta_\phi,\,\psi+\varepsilon\eta_\psi;\nabla\phi+\varepsilon\nabla\eta_\phi,\,\nabla\psi+\varepsilon\nabla\eta_\psi\Big)\bigg|_{\varepsilon=0}\,d\Omega.$$

By the chain rule,

$$\frac{d}{d\varepsilon}f\bigg|_{\varepsilon=0}=\frac{\partial f}{\partial\phi}\,\eta_\phi+\frac{\partial f}{\partial\nabla\phi}\cdot\nabla\eta_\phi+\frac{\partial f}{\partial\psi}\,\eta_\psi+\frac{\partial f}{\partial\nabla\psi}\cdot\nabla\eta_\psi.$$

Substituting this into the previous identity gives

$$\delta\mathcal{F}=\int_\Omega\left(\frac{\partial f}{\partial\phi}\,\eta_\phi+\frac{\partial f}{\partial\nabla\phi}\cdot\nabla\eta_\phi+\frac{\partial f}{\partial\psi}\,\eta_\psi+\frac{\partial f}{\partial\nabla\psi}\cdot\nabla\eta_\psi\right)\,d\Omega.$$

We next apply integration by parts to the gradient terms. For the ϕ-dependent contribution, we have

$$\int_\Omega\frac{\partial f}{\partial\nabla\phi}\cdot\nabla\eta_\phi\,d\Omega=-\int_\Omega\nabla\cdot\left(\frac{\partial f}{\partial\nabla\phi}\right)\eta_\phi\,d\Omega+\int_{\partial\Omega}\left(\frac{\partial f}{\partial\nabla\phi}\cdot n\right)\eta_\phi\,dS,$$

where n denotes the outward unit normal on $\partial\Omega$ If the test functions η_ϕ and η_ψ vanish on $\partial\Omega$, or if the natural boundary conditions are imposed so that the boundary integrals vanish, the boundary contributions drop out. As a result, the first variation of $\mathcal{F}$ can be written as

$$\delta\mathcal{F}=\int_\Omega\left[\left(\frac{\partial f}{\partial\phi}-\nabla\cdot\frac{\partial f}{\partial\nabla\phi}\right)\eta_\phi+\left(\frac{\partial f}{\partial\psi}-\nabla\cdot\frac{\partial f}{\partial\nabla\psi}\right)\eta_\psi\right]\,d\Omega.$$

By definition of the L^2 functional derivatives, the chemical potentials are identified as

$$\mu_\phi = \frac{\delta \mathcal{F}}{\delta \phi} = \frac{\partial f}{\partial \phi} - \nabla \cdot \frac{\partial f}{\partial \nabla \phi}, \tag{B.1}$$

and

$$\mu_\psi = \frac{\delta \mathcal{F}}{\delta \psi} = \frac{\partial f}{\partial \psi} - \nabla \cdot \frac{\partial f}{\partial \nabla \psi}. \tag{B.2}$$

B.1.1 Calculation of μ_ϕ.

First, compute $\frac{\partial f}{\partial \phi}$:

$$\frac{\partial f}{\partial \phi} = \lambda_\phi W'(\phi) + r'(\phi)\Big[\lambda_\psi\Big(W(\psi) + \frac{1}{2}|\nabla \psi|^2\Big) + r(\psi)\, L\Big(1 - \frac{T}{T_m}\Big)\Big].$$

Next, compute $\frac{\partial f}{\partial \nabla \phi}$:

$$\frac{\partial f}{\partial \nabla \phi} = \lambda_\phi \nabla \phi.$$

Therefore,

$$-\nabla \cdot \frac{\partial f}{\partial \nabla \phi} = -\lambda_\phi \Delta \phi.$$

Combining these two results gives:

$$\mu_\phi = -\lambda_\phi \Delta \phi + \lambda_\phi W'(\phi) + r'(\phi)\Big[\lambda_\psi\Big(W(\psi) + \frac{1}{2}|\nabla \psi|^2\Big) + r(\psi)\, L\Big(1 - \frac{T}{T_m}\Big)\Big]. \tag{B.3}$$

B.1.2 Calculation of μ_ψ.

First, compute $\frac{\partial f}{\partial \psi}$:

$$\frac{\partial f}{\partial \psi} = r(\phi)\Big[\lambda_\psi W'(\psi) + r'(\psi)\, L\Big(1 - \frac{T}{T_m}\Big)\Big].$$

Next, compute $\frac{\partial f}{\partial \nabla \psi}$:

$$\frac{\partial f}{\partial \nabla \psi} = r(\phi)\lambda_\psi \nabla \psi.$$

Therefore,

$$-\nabla \cdot \frac{\partial f}{\partial \nabla \psi} = -\nabla \cdot \Big(r(\phi)\lambda_\psi \nabla \psi\Big).$$

If $r(\phi)$ is assumed spatially uniform (or treated as constant during differentiation with respect to ψ), this simplifies to:

$$-\nabla \cdot \Big(r(\phi)\lambda_\psi \nabla \psi\Big) = -\lambda_\psi r(\phi)\Delta \psi.$$

Hence,

$$\mu_\psi = -\lambda_\psi \Delta \psi + r(\phi)\Big[\lambda_\psi W'(\psi) + r'(\psi)\, L\Big(1 - \frac{T}{T_m}\Big)\Big]. \tag{B.4}$$

These are the full expanded forms of the chemical potentials μ_ϕ and μ_ψ, showing contributions from the gradient (interfacial) energy, the bulk double-well potential, and the phase coupling with latent heat.

B.2 Derivation of the Extrapolation Formula for $F^{n+1/2}$

To derive an explicit approximation of $F^{n+1/2}$ using only past time levels, we employ a second-order Taylor expansion around the time level n. We seek a linear extrapolation formula of the form:

$$F^{n+1/2} \approx aF^n + bF^{n-1}, \tag{B.5}$$

where a and b are constants to be determined.

To determine the coefficients a and b in the extrapolation formula

$$F^{n+1/2} \approx aF^n + bF^{n-1},$$

we compare this form with the Taylor series expansion of $F^{n+1/2}$ around time step n. Specifically, we expand F^{n-1} and $F^{n+1/2}$ as:

$$F^{n-1} = F^n - \Delta t \left.\frac{dF}{dt}\right|_n + \frac{1}{2}\Delta t^2 \left.\frac{d^2F}{dt^2}\right|_n + O(\Delta t^3),$$

$$F^{n+1/2} = F^n + \frac{1}{2}\Delta t \left.\frac{dF}{dt}\right|_n + \frac{1}{8}\Delta t^2 \left.\frac{d^2F}{dt^2}\right|_n + O(\Delta t^3).$$

Substituting the Taylor expansion of F^{n-1} into the extrapolated form yields:

$$F^{n+1/2} = aF^n + b\left(F^n - \Delta t \left.\frac{dF}{dt}\right|_n + \frac{1}{2}\Delta t^2 \left.\frac{d^2F}{dt^2}\right|_n\right) + O(\Delta t^3),$$

which simplifies to:

$$F^{n+1/2} = (a+b)F^n - b\Delta t \left.\frac{dF}{dt}\right|_n + \frac{1}{2}b\Delta t^2 \left.\frac{d^2F}{dt^2}\right|_n + O(\Delta t^3).$$

We then match the coefficients of this expression with those of the Taylor expansion of

$F^{n+1/2}$. Comparing the zeroth-order terms yields:

$$a + b = 1.$$

Matching the first-order terms gives:

$$-b = \frac{1}{2} \quad \Rightarrow \quad b = -\frac{1}{2}.$$

Substituting this into the zeroth-order equation, we find:

$$a = 1 - b = 1 + \frac{1}{2} = \frac{3}{2}.$$

Therefore, the final extrapolation formula is:

$$F^{n+1/2} \approx \frac{3}{2}F^n - \frac{1}{2}F^{n-1}.$$

This formula provides a second-order accurate approximation of $F^{n+1/2}$ using only values at F^n and F^{n-1}, and is used throughout our numerical scheme for explicit evaluation of nonlinear terms.

B.3 Detailed Proof of Energy Dissipation for IEQ Scheme

In this appendix, we provide the full derivation of the energy dissipation law for the proposed Crank-Nicolson IEQ numerical scheme, establishing its unconditional stability.

B.3.1 Evolution Equations

Recall the semi-discrete evolution equations derived in Chapter 4.3:

The Crank-Nicolson scheme discretizes the evolution equations for ϕ, ψ, and q as follows:

$$\frac{\phi^{n+1}-\phi^n}{\Delta t} = \Delta \mu_\phi^{n+1/2}, \tag{B.6}$$

$$\frac{\psi^{n+1}-\psi^n}{\Delta t} = -\mu_\psi^{n+1/2}, \tag{B.7}$$

$$\frac{q^{n+1}-q^n}{\Delta t} = \frac{1}{2\sqrt{F^{n+\frac{1}{2}}+C_0}}\left(\frac{\partial F^{n+1/2}}{\partial \phi}\frac{\phi^{n+1}-\phi^n}{\Delta t} + \frac{\partial F^{n+1/2}}{\partial \psi}\frac{\psi^{n+1}-\psi^n}{\Delta t}\right), \tag{B.8}$$

where:

$$\mu_\phi^{n+1/2} = -\lambda_\phi \Delta\left(\frac{\phi^{n+1}+\phi^n}{2}\right) + \frac{q^{n+1/2}}{\sqrt{F^{n+1/2}+C_0}}\frac{\partial F^{n+1/2}}{\partial \phi}, \tag{B.9}$$

$$\mu_\psi^{n+1/2} = -\lambda_\psi \Delta\left(\frac{\psi^{n+1}+\psi^n}{2}\right) + \frac{q^{n+1/2}}{\sqrt{F^{n+1/2}+C_0}}\frac{\partial F^{n+1/2}}{\partial \psi}. \tag{B.10}$$

To analyze the stability, we multiply each equation with carefully chosen test functions:

- For ϕ, the test function is $\mu_\phi^{n+1/2}$.
- For ψ, the test function is $\mu_\psi^{n+1/2}$.
- For q, the test function is $q^{n+1}+q^n$.

The chemical potentials μ_ϕ and μ_ψ directly govern the evolution of the order parameters ϕ and ψ, respectively. Testing with these potentials ensures that the derived stability analysis aligns with the physical energy dissipation law. The auxiliary variable q is linked to the free energy functional through q^2, making $2q^{n+1/2}$ a natural choice to preserve the quadratic coupling in the stability analysis. These test functions simplify the derivation of the energy dissipation law by directly linking the evolution equations to the gradient norm terms, as shown in the sections below.

B.3.1.1 Testing the ϕ Equation

To analyze the stability of the numerical scheme, we begin by testing the ϕ evolution equation with the test function $\mu_\phi^{n+1/2}$.

Step 1: Multiply the equation (B.6) by $\mu_\phi^{n+1/2}$ and integrate over Ω:

$$\int_\Omega \frac{\phi^{n+1} - \phi^n}{\Delta t} \mu_\phi^{n+1/2} \, d\Omega = \int_\Omega \Delta \mu_\phi^{n+1/2} \mu_\phi^{n+1/2} \, d\Omega.$$

Step 2: Expand the left-hand side. The left-hand side represents the time derivative of ϕ, weighted by the chemical potential. Expanding this term gives:

$$\int_\Omega \frac{\phi^{n+1} - \phi^n}{\Delta t} \mu_\phi^{n+1/2} \, d\Omega = \frac{1}{\Delta t} \int_\Omega \mu_\phi^{n+1/2} (\phi^{n+1} - \phi^n) \, d\Omega.$$

Step 3: Simplify the right-hand side using the Laplacian. For the right-hand side, we use integration by parts and assume Neumann boundary conditions ($\nabla \mu_\phi^{n+1/2} \cdot \mathbf{n} = 0$ on $\partial\Omega$):

$$\int_\Omega \Delta \mu_\phi^{n+1/2} \mu_\phi^{n+1/2} \, d\Omega = -\int_\Omega |\nabla \mu_\phi^{n+1/2}|^2 \, d\Omega.$$

Here, $|\nabla \mu_\phi^{n+1/2}|^2 = (\nabla \mu_\phi^{n+1/2}) \cdot (\nabla \mu_\phi^{n+1/2})$, and the negative sign reflects the dissipation of energy.

Step 4: Combine the results. Equating the left-hand side and the simplified right-hand side, we have:

$$\frac{1}{\Delta t} \int_\Omega \mu_\phi^{n+1/2} (\phi^{n+1} - \phi^n) \, d\Omega = -\int_\Omega |\nabla \mu_\phi^{n+1/2}|^2 \, d\Omega.$$

Step 5: Interpret the result. The result shows that the dissipation of the gradient norm $\|\nabla \mu_\phi^{n+1/2}\|^2$ is directly linked to the time evolution of ϕ, weighted by the chemical potential $\mu_\phi^{n+1/2}$. This energy dissipation is crucial for the stability of the scheme, as it ensures that the total energy decreases over time.

The testing process leads to the following dissipation equation for ϕ:

$$\frac{1}{\Delta t}\int_\Omega \mu_\phi^{n+1/2}(\phi^{n+1}-\phi^n)\,d\Omega = -\|\nabla\mu_\phi^{n+1/2}\|^2, \tag{B.11}$$

where $\|\nabla\mu_\phi^{n+1/2}\|^2 = \int_\Omega |\nabla\mu_\phi^{n+1/2}|^2\,d\Omega$ is the gradient norm of the chemical potential.

B.3.1.2 Testing the ψ Equation

Similarly, test the ψ evolution equation (B.7) with $\mu_\psi^{n+1/2}$:

$$\left\langle \frac{\psi^{n+1}-\psi^n}{\Delta t}, \mu_\psi^{n+1/2} \right\rangle = \left\langle -\mu_\psi^{n+1/2}, \mu_\psi^{n+1/2} \right\rangle. \tag{B.12}$$

Simplify the Left-Hand Side (LHS):

$$\left\langle \frac{\psi^{n+1}-\psi^n}{\Delta t}, \mu_\psi^{n+1/2} \right\rangle = \frac{1}{\Delta t}\int_\Omega \mu_\psi^{n+1/2}(\psi^{n+1}-\psi^n)\,d\Omega.$$

Simplify the Right-Hand Side (RHS):

$$\left\langle -\mu_\psi^{n+1/2}, \mu_\psi^{n+1/2} \right\rangle = -\int_\Omega (\mu_\psi^{n+1/2})^2\,d\Omega.$$

Equating the simplified LHS and RHS, we have:

$$\frac{1}{\Delta t}\int_\Omega \mu_\psi^{n+1/2}(\psi^{n+1}-\psi^n)\,d\Omega = -\int_\Omega (\mu_\psi^{n+1/2})^2\,d\Omega.$$

The dissipation equation for ψ becomes:

$$\frac{1}{\Delta t}\int_\Omega \mu_\psi^{n+1/2}(\psi^{n+1}-\psi^n)\,d\Omega = -\|\mu_\psi^{n+1/2}\|^2, \tag{B.13}$$

where:

$$\|\mu_\psi^{n+1/2}\|^2 = \int_\Omega (\mu_\psi^{n+1/2})^2 \, d\Omega.$$

This result shows that the evolution of ψ dissipates the norm of $\mu_\psi^{n+1/2}$, ensuring energy dissipation and contributing to the unconditional stability of the scheme.

B.3.1.3 Testing the q Equation

We aim to demonstrate the unconditional stability of the scheme for the auxiliary variable q.

Multiply equation (B.8) by $q^{n+1} + q^n$ and integrate over Ω:

$$\begin{aligned}\int_\Omega \frac{q^{n+1} - q^n}{\Delta t} \cdot (q^{n+1} + q^n) \, d\Omega = \int_\Omega \frac{1}{2\sqrt{F^{n+\frac{1}{2}} + C}} \Bigg(& \frac{\partial F^{n+1/2}}{\partial \phi} \frac{\phi^{n+1} - \phi^n}{\Delta t} \\ & + \frac{\partial F^{n+1/2}}{\partial \psi} \frac{\psi^{n+1} - \psi^n}{\Delta t} \Bigg) \cdot (q^{n+1} + q^n) \, d\Omega.\end{aligned} \tag{B.14}$$

Equating the LHS and RHS, the evolution of q satisfies:

$$\begin{aligned}\frac{1}{\Delta t} \int_\Omega \left((q^{n+1})^2 - (q^n)^2 \right) \, d\Omega = & \int_\Omega \frac{(q^{n+1} + q^n)}{2\sqrt{F^{n+\frac{1}{2}} + C}} \frac{\partial F^{n+1/2}}{\partial \phi} \frac{\phi^{n+1} - \phi^n}{\Delta t} \, d\Omega \\ & + \int_\Omega \frac{(q^{n+1} + q^n)}{2\sqrt{F^{n+\frac{1}{2}} + C}} \frac{\partial F^{n+1/2}}{\partial \psi} \frac{\psi^{n+1} - \psi^n}{\Delta t} \, d\Omega.\end{aligned} \tag{B.15}$$

B.3.1.4 Testing the chemical potentials

The chemical potentials $\mu_\phi^{n+1/2}$ and $\mu_\psi^{n+1/2}$ are key components in the energy evolution of the system. When multiplied by the respective time derivatives $\frac{\phi^{n+1}-\phi^n}{\Delta t}$ and $\frac{\psi^{n+1}-\psi^n}{\Delta t}$, they quantify the dissipation contributions of each variable to the total energy.

Multiplying $\mu_\phi^{n+1/2}$ by $\frac{\phi^{n+1}-\phi^n}{\Delta t}$ and integrating over the domain Ω, we obtain

$$\int_\Omega \mu_\phi^{n+1/2} \cdot \frac{\phi^{n+1}-\phi^n}{\Delta t}\, d\Omega = \int_\Omega -\lambda_\phi \Delta \left(\frac{\phi^{n+1}+\phi^n}{2}\right) \cdot \frac{\phi^{n+1}-\phi^n}{\Delta t}\, d\Omega + \int_\Omega \frac{q^{n+1/2}}{\sqrt{F^{n+1/2}+C}} \frac{\partial F^{n+1/2}}{\partial \phi} \cdot \frac{\phi^{n+1}-\phi^n}{\Delta t}\, d\Omega. \tag{B.16}$$

Using integration by parts, the first term simplifies to:

$$\int_\Omega \Delta \left(\frac{\phi^{n+1}+\phi^n}{2}\right) \cdot \frac{\phi^{n+1}-\phi^n}{\Delta t}\, d\Omega = -\frac{1}{2\Delta t} \int_\Omega \left(|\nabla \phi^{n+1}|^2 - |\nabla \phi^n|^2\right)\, d\Omega. \tag{B.17}$$

Substituting (B.17) into (B.16), we obtain

$$\int_\Omega \mu_\phi^{n+1/2} \cdot \frac{\phi^{n+1}-\phi^n}{\Delta t}\, d\Omega = -\frac{\lambda_\phi}{2\Delta t} \int_\Omega \left(|\nabla \phi^{n+1}|^2 - |\nabla \phi^n|^2\right)\, d\Omega + \int_\Omega \frac{q^{n+1/2}}{\sqrt{F^{n+1/2}+C}} \frac{\partial F^{n+1/2}}{\partial \phi} \cdot \frac{\phi^{n+1}-\phi^n}{\Delta t}\, d\Omega. \tag{B.18}$$

This shows that the change in $|\nabla \phi|^2$ contributes to energy dissipation, while the free energy coupling term reflects the interaction with the potential energy.

Similarly, for ψ, we have:

$$\int_\Omega \mu_\psi^{n+1/2} \cdot \frac{\psi^{n+1}-\psi^n}{\Delta t}\, d\Omega = \int_\Omega -\lambda_\psi \Delta \left(\frac{\psi^{n+1}+\psi^n}{2}\right) \cdot \frac{\psi^{n+1}-\psi^n}{\Delta t}\, d\Omega + \int_\Omega \frac{q^{n+1/2}}{\sqrt{F^{n+1/2}+C}} \frac{\partial F^{n+1/2}}{\partial \psi} \cdot \frac{\psi^{n+1}-\psi^n}{\Delta t}\, d\Omega. \tag{B.19}$$

The Laplacian term simplifies to:

$$\int_\Omega \Delta \left(\frac{\psi^{n+1}+\psi^n}{2}\right) \cdot \frac{\psi^{n+1}-\psi^n}{\Delta t}\, d\Omega = -\frac{1}{2\Delta t} \int_\Omega \left(|\nabla \psi^{n+1}|^2 - |\nabla \psi^n|^2\right)\, d\Omega. \tag{B.20}$$

Substituting into (B.19), we obtain

$$\int_\Omega \mu_\psi^{n+1/2} \cdot \frac{\psi^{n+1} - \psi^n}{\Delta t}\, d\Omega = -\frac{\lambda_\psi}{2\Delta t} \int_\Omega \left(|\nabla \psi^{n+1}|^2 - |\nabla \psi^n|^2 \right)\, d\Omega + \int_\Omega \frac{q^{n+1/2}}{\sqrt{F^{n+1/2} + C}} \frac{\partial F^{n+1/2}}{\partial \psi} \cdot \frac{\psi^{n+1} - \psi^n}{\Delta t}\, d\Omega. \tag{B.21}$$

These expressions will be used to derive the discrete energy dissipation law.

B.3.1.5 Combining the Dissipation Laws

Combining equations (B.11), (B.13), (B.15), (B.16), and (B.19) we obtain the total energy dissipation law:

$$\begin{aligned} \frac{1}{\Delta t} \int_\Omega |q^{n+1}|^2 - |q^n|^2\, d\Omega = &- \int_\Omega |\nabla \mu_\phi^{n+1/2}|^2\, d\Omega - \int_\Omega |\mu_\psi^{n+1/2}|^2\, d\Omega, \\ &+ \int_\Omega \lambda_\phi \Delta \left(\frac{\phi^{n+1} + \phi^n}{2} \right) \frac{\phi^{n+1} - \phi^n}{\Delta t}\, d\Omega \\ &+ \int_\Omega \lambda_\psi \Delta \left(\frac{\psi^{n+1} + \psi^n}{2} \right) \frac{\psi^{n+1} - \psi^n}{\Delta t}\, d\Omega. \end{aligned}$$

Substituting Eq. (B.17) and Eq. (B.20) into the dissipation terms, we have:

$$\begin{aligned} \frac{1}{\Delta t} \int_\Omega \left[(q^{n+1})^2 - (q^n)^2 \right]\, d\Omega = &- \int_\Omega |\nabla \mu_\phi^{n+1/2}|^2\, d\Omega - \int_\Omega |\mu_\psi^{n+1/2}|^2\, d\Omega \\ &- \frac{1}{2\Delta t} \int_\Omega \lambda_\phi \left(|\nabla \phi^{n+1}|^2 - |\nabla \phi^n|^2 \right)\, d\Omega \\ &- \frac{1}{2\Delta t} \int_\Omega \lambda_\psi \left(|\nabla \psi^{n+1}|^2 - |\nabla \psi^n|^2 \right)\, d\Omega. \end{aligned}$$

The total dissipation law becomes:

$$\begin{aligned}\frac{1}{\Delta t}\int_\Omega \left[|q^{n+1}|^2-|q^n|^2\right]\,d\Omega \quad &+\frac{1}{2\Delta t}\int_\Omega \lambda_\phi\left(|\nabla\phi^{n+1}|^2-|\nabla\phi^n|^2\right)\,d\Omega\\ &+\frac{1}{2\Delta t}\int_\Omega \lambda_\psi\left(|\nabla\psi^{n+1}|^2-|\nabla\psi^n|^2\right)\,d\Omega\\ &=-\int_\Omega |\nabla\mu_\phi^{n+1/2}|^2\,d\Omega-\int_\Omega |\mu_\psi^{n+1/2}|^2\,d\Omega\le 0. \end{aligned}\tag{B.22}$$

Finally, combining equations, we obtain the total discrete energy dissipation law:

$$\mathcal{E}^{n+1}-\mathcal{E}^n=-\Delta t\int_\Omega |\nabla\mu_\phi^{n+1/2}|^2\,d\Omega-\Delta t\int_\Omega (\mu_\psi^{n+1/2})^2\,d\Omega\le 0,\tag{B.23}$$

where

$$\mathcal{E}^n=\int_\Omega\left(\frac{\lambda_\phi}{2}|\nabla\phi^n|^2+\frac{\lambda_\psi}{2}|\nabla\psi^n|^2+(q^n)^2-C\right)\,d\Omega.$$

We can rewrite the dissipation law as:

$$\mathcal{E}^{n+1}-\mathcal{E}^n\le 0.\tag{B.24}$$

This final expression encapsulates the total energy dissipation, ensuring that the numerical scheme is unconditionally stable. Each term represents the dissipative contributions from ϕ, ψ, and q, showing that the total discrete energy functional decreases monotonically over time.